INTERACTIONS OF WAVES AND PARTICLES IN PLASMAS WITH REFERENCE TO AN EXPERIMENTAL STUDY OF CURRENT-DRIVEN TURBULENCE

by

W.H.M. CLARK

Wolfson College

This thesis is submitted in partial fulfilment for the requirements for the Degree of Doctor of Philosophy in the University of Oxford

Dept. of Eng. Science,
Parks Road, Oxford

Hilary Term
1976

TO MY PARENTS

CONTENTS

Page

CHAPTER I

INTRODUCTION 1

1.1 PLASMA TURBULENCE 1

1.2 RESPONSE OF PLASMA TO A STEADY ELECTRIC FIELD 7

CHAPTER II

CURRENT-DRIVEN ELECTROSTATIC INSTABILITIES 12

2.1 INTRODUCTION 12

2.2 COLD, ONE-DIMENSIONAL PLASMA 13

2.3 COLD PLASMA IN CYLINDRICAL GEOMETRY WITH AN AXIAL MAGNETIC MAGNETIC FIELD 14

2.4 WARM PLASMA 17

2.4.1 One-Dimensional Plasma 17

2.4.2 The Experimental Plasma 20

2.5 FURTHER COMMENTS 22

2.5.1 Electron Acceleration in a Steady Field E_0 22

2.5.2 Nonlinear Development: A Comparison with the Beam-Plasma Two-stream Instability 24

CHAPTER III

THE EXPERIMENT 27

3.1 THE PLASMA 27

3.2 THE EXPERIMENT 31

3.3 ELECTRICAL MEASUREMENTS 34

3.4 A THEORY DESCRIBING THE ESTABLISHMENT OF AN ELECTRON DRIFT IN A COLLISIONLESS PLASMA COLUMN 38

3.4.1 The Transmission Line Equations for a Cold Electron Plasma Column 38

3.4.2 The Equivalent Circuit 41

3.4.3 Comparison with Experiment 45

CONTENTS
(continued)

Page

CHAPTER IV

A PLASMA DIAGNOSTIC: DISPERSION OF ELECTRON PLASMA WAVES 48

4.1 INTRODUCTION 48

4.2 TIME-RESOLVED MEASUREMENT OF THE DISPERSION 48

4.3 ELECTRONIC SAMPLING TECHNIQUE 50

4.4 RESULTS 57

4.5 ANALYSIS 58

4.6 DISCUSSION OF THE RESULTS FOR $t > 0.2\ \mu s$ 63

4.7 THE INITIAL TRANSIENT (for $I > I_c$) 69

4.8 CONCLUSION 75

CHAPTER V

THE FLUCTUATION SPECTRUM 76

5.1 INTRODUCTION 76

5.2 FLUCTUATION MEASUREMENTS 77

- 5.2.1 Frequency Spectrum 78
- 5.2.2 Wave-Vector Spectrum

5.3 PRACTICAL PROBLEMS ENCOUNTERED WITH ELECTROSTATIC PROBES 81

- 5.3.1 Frequency Response and Absolute Amplitude Calibration 81
- 5.3.2 Local Disturbance of the Plasma 82

5.4 LOW FREQUENCY FLUCTUATIONS, 3 - 20 MHz 83

5.5 THE HIGH FREQUENCY FLUCTUATIONS, > 50 MHz 88

5.6 CONCLUSION 90

CHAPTER VI

CONCLUSION 93

6.1 TURBULENT HEATING EXPERIMENTS 93

6.2 COMPUTER SIMULATIONS 96

6.3 THEORETICAL APPROACHES 99

6.4 SUMMARY OF RESULTS AND OUTSTANDING PROBLEMS 101

CONTENTS

(continued)

Page

APPENDICES

App. A.1 DISPERSION RELATION FOR THE ELECTRON-ION TWO-STREAM INSTABILITY FOR A COLD 1-D PLASMA 103

App. A.2 DISPERSION RELATION FOR A COLD PLASMA COMPLETELY FILLING A CYLINDRICAL WAVEGUIDE WITH AN AXIAL MAGNETIC FIELD SUCH THAT $\omega_{ce}^2 \gg \omega_{pe}^2 \gg \omega_{pi}^2 \gg \omega_{ci}^2$ 107

App.A.3 DISPERSION RELATION FOR ELECTRON PLASMA WAVES 112

App.A.4 VARIATIONS OF THE TECHNIQUE FOR TIME-RESOLVED MEASUREMENTS OF THE DISPERSION OF ELECTRON PLASMA WAVES 116

App.A.5 THE ENSEMBLE AVERAGE POWER SPECTRUM OF THE HIGH-FREQUENCY FLUCTUATIONS MEASURED WITH AN ELECTRONIC SPECTRUM ANALYSER 121

REFERENCES 125

LIST OF FREQUENTLY USED SYMBOLS

(Wherever a symbol occasionally has another meaning, it is made clear from the context.)

a	radius of plasma column
A	area of plasma column
A_p	p^{th} velocity moment of the axial electron distribution function, (see p.60)
$A(\tau)$	normalised ensemble average of the instantaneous auto-correlation, (see p.79)
b	radius of cylindrical waveguide
B_o, B_z	uniform axial magnetic field
c	velocity of light
c_s	ion acoustic speed
$C(\underline{\xi})$	normalised ensemble average of the instantaneous two-probe cross-correlation, (see p.81)
$D(\omega, k)$	Dispersion relation, (see p.12)
e	electronic charge
$\underline{\tilde{E}}$	fluctuating, self-consistent, electrostatic field
E_c	critical field for the electron-ion two-stream instability, (see p.23)
E_{Dr}	Dreicer field, (see p.8)
E_o	uniform applied electric field
$F(\underline{r}, \underline{v}, t)$	one-particle distribution function, (subscripts 'i' denotes ions, 'e' denotes electrons)
$H(t)$	Heaviside step function
I	plasma current
I_c	critical plasma current, (see p.34)
$\underline{k}$	wave-vector
k_z	component of $\underline{k}$ in the axial direction
ℓ	length of plasma column
m	electron mass, (also m_e)
M	ion mass, (also m_i)
n	particle number density
N_D	number of particles in a Debye cube
$p_{\mu\nu}$	ν^{th} root of the μ^{th}-order Bessel's function of the first kind
r	radial coordinate for cylindrical polar coordinate system
$\underline{r}$	position vector

R	resistance of plasma column
$S(t)$	fluctuation signal detected by an electrostatic probe
t	time coordinate, (measured from start of pulse)
T	temperature, (subscripts 'i' denotes ions, 'e' denotes electrons)
u	characteristic velocity for the plasma column, (see p.40)
$\underline{v}$	velocity vector
v_d	electron drift velocity
v_e	electron root mean square (or thermal) velocity
v_{eo}	electron thermal velocity at $t = 0$
v_z	axial component of velocity
V	voltage at cold plate, (see p.34)
V_o	open-circuit pulse generator voltage, (see p.32)
V_{pl}	voltage across plasma column excluding cold plate sheath, (see p.34)
V_s	voltage across cold plate sheath, (see p.34)
W	energy density of collective fluctuations
z	axial coordinate for cylindrical polar coordinate system
Z_o	characteristic impedance for the plasma column, (see p.40)
α	angle of propagation of $\underline{k}$ with respect to $\underline{B}$, (see p.17)
γ	temporal growth rate
$\underline{\underline{\epsilon}}$	plasma dielectric tensor
ϵ_o	permittivity of free space
φ	electrostatic potential
$\tilde{\varphi}$	amplitude of electrostatic oscillation
κ	Boltzmann's constant
λ_D	Debye length
μ_o	permeability of free space
μ	azimuthal mode number, (see p.14)
ν	radial mode number, (see p.15)
ν_c	binary collision frequency for collisions between ions and electrons
ν_{eff}	effective collision frequency for collisions between ions and electrons
σ	plasma electrical conductivity
τ_{ac}	wave coherence time
τ_c	binary collision time for collisions between ions and electrons
τ_{eff}	effective collision time for collisions between ions and electrons

τ_R	risetime of voltage pulse
τ_{tr}	particle trapping time
θ	azimuthal coordinate for cylindrical polar coordinate system
ω	2π X wave frequency
ω_c	2π X cyclotron frequency, 'i' ions; 'e' electrons
ω_p	2π X plasma frequency, 'i' ions; 'e' electrons
ω_r	real part of ω
ω^*	2π X characteristic frequency for the electron-ion two-stream instability.

ACKNOWLEDGEMENTS

The experimental work described in this thesis was carried out on the single-ended Q-Machine, THESEUS, while I was on attachment at the UKAEA Culham Laboratory from the Department of Engineering Science, Oxford University. The experiment was partly supported by the Science Research Council and partly by Culham Laboratory, both of which I wish to gratefully acknowledge for personal financial support in the form of an SRC post-graduate award for three years followed by a fifteen month graduate studentship from Culham.

Although the experimental rig was operated and maintained by myself, I should like to express my gratitude to the constructor of THESEUS, Mr W.J. McKay, for his helpfulness and for being able to draw upon his great wealth of experience and advice in combating the numerous hardware problems encountered during my work. Technical assistance was also rendered cheerfully by Miss Susan Gulliver and Mr J.B.B. Percival.

It is a great pleasure to acknowledge the stimulating and fruitful discussions held with my colleagues, Dr P.D. Edgley and Mr S. Mrowka. The latter I am particularly grateful to for writing the computer program and processing the data for the frequency power spectra reported in Chapter V. It is also a great pleasure to acknowledge the encouragement and support I have received from Dr R.N. Franklin and my supervisor, Dr S.M. Hamberger. The latter I owe a particular debt, not only for his constant stimulation throughout the course of my research, but also for teaching me how to prepare and present this work.

Finally my thanks must go to Ina Godwin, who again has earned her reputation for meticulous attention to detail, not only in the typing of this thesis, but also in the layout and labelling of figures.

ABSTRACT

This thesis is an experimental study of a plasma which is made strongly turbulent by conducting an electric current. The experiments are performed on the cylindrical potassium plasma column which exists between the hot and cold end-plates of a single-ended Q-machine. The plasma is continuously produced at the hotplate by contact ionization and confined radially by a strong axial magnetic field such that $\omega_{ce} \gg \omega_{pe}$. The electrons and ions are initially close to thermal equilibrium with the hotplate, with a common temperature $\simeq 0.2$ eV. The plasma density ($\sim 10^9$ cm^{-3}), is such that the time for collisions between electrons and ions is very long compared to the time taken for an electron to travel the length of the column.

Pulsed electron currents of duration $\sim 2\,\mu s$ are drawn through the plasma by applying positive voltage pulses $(\leqslant 100\,V)$ to the cold plate. Simple electrical measurements indicate that, above a critical current, the plasma has an anomalously low conductivity accompanied by the onset of a high level of potential fluctuations, which are detected in the plasma by electrostatic probes.

A diagnostic technique has been developed to study the temporal evolution of the distribution function of axial electron velocities. This involves time-resolved measurements of the dispersion of electron plasma waves during the current pulse. Analysis of this dispersion gives unambiguous measurements of the electron density n, drift velocity v_d, and root mean square (or thermal) velocity v_e, during the pulse. The results indicate that, after an initial transient, n and v_d are axially uniform, n remains equal to the initial value and the current drawn from the plasma gives a good measure of their product. The critical current

corresponds to $v_d = 1.3\ v_c$, which linear theory predicts, is the threshold for the electron-ion two-stream instability. Above this threshold, v_e quickly exceeds v_d and, in contrast to the predictions of linear theory and computer simulation, continues to rise for constant v_d to high values, (indicating electron temperatures $\leqslant 80$ eV), limited only by the energy containment time of the column. The values of conductivity deduced from the effective scattering rate and from the electrical measurements are in good agreement, and are consistent with an empirical scaling law found in a pulsed toroidal discharge by other workers.

Measurements on the potential fluctuations indicate a broad frequency spectrum: in the low frequencies the correlation lengths were too short to be measured; in the high frequencies the fluctuations were shown to consist of relatively coherent, long wavelength electron plasma waves.

CHAPTER I

INTRODUCTION

This work is an experimental investigation of a plasma which is made strongly turbulent by conducting an electric current. In this chapter we introduce the phenomenon of plasma turbulence by considering the relaxation times associated with transport processes in a fully ionized plasma. From this we see that the effective collision frequency for plasmas which are not in thermal equilibrium * might be greatly enhanced by collective fluctuations, when compared with plasmas in thermal equilibrium. In particular, we consider the response of a plasma to a steady electric field and the chapter concludes with an introduction to the experiment.

1.1 PLASMA TURBULENCE

Fully ionized plasma can be regarded as an assembly of electrons and ions, (which in this particular work are singly charged), whose average number densities n , when considered over sufficiently long time and length scales, are such as to produce no net charge. In this work we consider only elastic collisions so that the particles interact only through their coulomb fields. Those transport processes which are responsible for dissipating some available free energy into particle thermal energy, can be expressed in terms of appropriate microscopic relaxation times τ , or effective collision frequencies, $\nu = \tau^{-1}$, which are determined by the interaction of particles with fluctuating electrostatic fields $\underline{\tilde{E}}$, which are themselves due to the coulomb fields of all the particles, i.e. self-consistent fields $\neq$

---

* By thermal equilibrium we mean that both species of particles have Maxwellian velocity distributions, with a common temperature T .

$\neq$ In general we should consider self-consistent electromagnetic fields, but in this work we can neglect these because all electromagnetic fluctuations have phase velocities very much faster than particle velocities.

Plasma kinetic theory can be applied to the problem of calculating $\underline{\tilde{E}}$ provided the parameter N_D, is very large, where

$$\left.\begin{aligned} N_D &= n\,\lambda_D^3 \gg 1 \\ \text{and} \qquad \lambda_D &= \sqrt{\frac{\epsilon_o\, KT}{n\, e^2}}\,, \quad \text{the Debye length.} \end{aligned}\right\} \qquad \ldots (1.1)$$

For the purposes of this discussion we will only summarize the main results by referring to various texts, (e.g. CLEMMOW and DOUGHERTY (1969) chapter 12 and references therein, also KRALL and TRIVELPIECE (1973) chapter 11).

For scalelengths $> \lambda_D$ the dynamics of each specie of particles in phase space $(\underline{r}\,,\,\underline{v})$, is described in terms of <u>one-particle distribution functions</u>, $F_{i,e}(\underline{r}\,,\underline{v}\,,t)^*$. The evolution of $F_{i,e}$ and the self-consistent fields are determined by the set of Vlasov-Maxwell equations :

$$\left.\begin{aligned} \frac{\partial F_{i,e}}{\partial t} + \underline{v}\cdot\underline{\nabla}_r F_{i,e} \pm \frac{e}{m_{i,e}}\left[\underline{E} + \underline{v}\wedge\underline{B}\right]\cdot\underline{\nabla}_v F_{i,e} &= 0 \\ \epsilon_o \operatorname{div}\underline{E} &= \rho_{ext} + e\int (F_i - F_e)\, d^3v \\ \operatorname{div}\underline{B} &= 0 \\ \operatorname{curl}\underline{E} &= -\frac{\partial \underline{B}}{\partial t} \\ \operatorname{curl}\underline{H} &= \underline{J}_{ext} + e\int (\underline{v}F_i - \underline{v}F_e)\, d^3v + \epsilon_o \frac{\partial \underline{E}}{\partial t} \end{aligned}\right\} \quad (1.2)$$

The fields which describe the collective nature of particle interactions are known as <u>collective fields</u>. They are smooth continuous functions that do not take into account the discrete nature of particle interactions. Linearized perturbation solutions describe the propagation of a great variety of collective oscillations $\propto \exp i(\underline{k}\cdot\underline{r} - \omega t)$, with wavelengths $k\lambda_D \gtrsim 1$ and phase velocities ω/k, which can be much less than c, the velocity of light.

---

* Subscripts i for ions, e for electrons

For scalelengths $< \lambda_D$, $\underline{\tilde{E}}$ is dominated by the discrete nature of particle interactions. For most of the time there are weak binary correlations between particles and $\underline{\tilde{E}}$ can be related to $F(\underline{r},\underline{v})$ by a two-particle correlation function*.

When a plasma is in thermal equilibrium, the energy density W, of the collective fluctuations is very small compared with the particle thermal energy, (e.g. see Krall and Trivelpiece (op. cit.) p.567), i.e.

$$\frac{W}{n\,KT} \sim \frac{1}{N_D} \quad . \qquad \ldots (1.3)$$

For each particle the dominant contribution to $\underline{\tilde{E}}$ is due to the binary correlations between it and all other particles within a Debye length. If the plasma is slightly perturbed, it is possible to estimate a relaxation time for particles to return to thermal equilibrium. For electrons, in the absence of a static magnetic field,

$$\left.\begin{aligned} \frac{1}{\nu_c} = \tau_c &= \frac{10}{n}\left(\frac{4\pi\epsilon_o}{e^2}\right)^2 \frac{m^{\frac{1}{2}}(KT)^{\frac{3}{2}}}{4\pi\log\Lambda} \sim \frac{N_D}{\omega_{pe}\log N_D} \\ \text{where} \qquad \Lambda &= \frac{12\pi(\epsilon_0 KT)^{\frac{3}{2}}}{n^{\frac{1}{2}}\,e^3} \\ \text{and} \qquad \omega_{pe} &= \sqrt{\frac{ne^2}{\epsilon_o m}}, \qquad \text{electron plasma frequency} \end{aligned}\right\} \qquad \ldots (1.4)$$

(see Clemmow and Dougherty (op.cit.) p.434).

If the plasma is not in thermal equilibrium there is the possibility of amplifying some of the modes of oscillation so that W exceeds the equilibrium value (1.3). If sufficient free energy is available, the linear solutions of (1.2) may indicate that some of the collective oscillations are unstable and these will grow at the expense of the free energy. In general the nonlinear development of these growing waves leads to a spectrum of collective fluctuations which begin to significantly perturb the particle

---

* This is true for thermal equilibrium, but may not be true for states far from thermal equilibrium, (see Clemmow and Dougherty (op.cit.) p.407).

motions and contribute an effective collision frequency ν_{eff}, to $\underline{\tilde{E}}$ in addition to ν_c in equation (1.4). It is possible that $\nu_{eff} \gg \nu_c$, but we may say that if $\nu_{eff} \geqslant \nu_c$, then the plasma is turbulent. The turbulence is a mechanism by which the plasma can effectively dissipate available free energy via collective fluctuations. A general scheme is shown in Fig.1.1.

Since equation (1.2) conserves entropy, strictly speaking this is not a thermal dissipation but conversion of free energy into a pathological form represented by the very fine-grained structure of $F(\underline{r},\underline{v})$ in phase space. However if $F(\underline{r},\underline{v})$ is reaveraged over a coarser grain, although it may not be in thermal equilibrium, it can be effectively considered as heated in certain regions of phase space.

In principle the calculation of $\underline{\tilde{E}}$ for collective fluctuations in a turbulent plasma requires a full nonlinear solution of the Vlasov-Maxwell equations (1.2). In practice considerable theoretical progress has been made for weakly turbulent plasmas, (see e.g. TSYTOVICH (1972), DRUMMOND and ROSS (1973) and references therein). The theory assumes that the waves have random phases with respect to each other and small growth or damping rates, i.e. amplitude $\propto \exp(\gamma t) \exp i(\underline{k}.\underline{r} - \omega t)$ where $\gamma^2 \ll \omega^2$. The amplitudes saturate by weak nonlinear interactions between waves and particles at low energy levels, i.e.

$$\frac{1}{N_D} \ll \frac{W}{n\kappa T} \ll 1 .$$

The phenomenological description is that of separate entities, waves and particles, where the concepts of energy and momentum for both are clearly and separately defined and the conservation laws, which describe their interaction, are easy to interpret.

However this analysis breaks down if $\gamma \sim \omega$, when high level amplitude saturation might occur, or if the spectrum of growing waves is

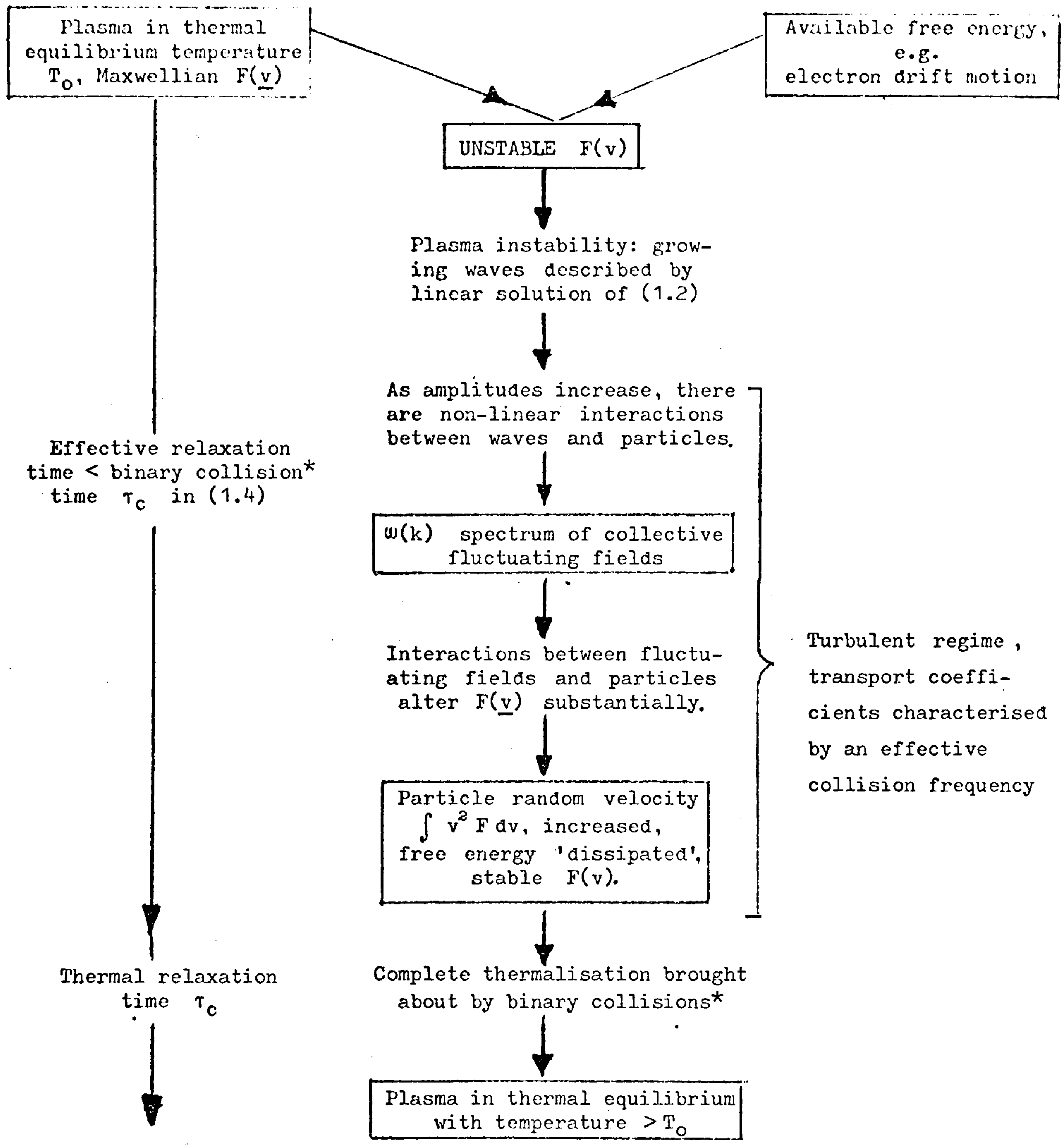

* By binary collision time we mean the time taken for a particle to be scattered through an angle of $\pi/2$ by the weak but continuous binary correlations between the particle and its neighbours within a Debye sphere.

Fig.1.1
A general scheme for plasma turbulence

sufficiently narrow such that the coherence time τ_{ac}, is long enough for particles to become temporarily 'trapped' by the wave, (see e.g. Chapter II).

By considering the two restrictions for weak turbulence theory, Drummond and Ross (op.cit.) derive a convenient classification of turbulent regimes. They define two parameters :

$$\Gamma_1 = \frac{W}{nKT} \qquad \dots (1.5)$$

and

$$\Gamma_2 = \frac{\tau_{ac}}{\tau_{tr}} , \qquad \dots (1.6)$$

where τ_{tr} is the time for particles to become trapped by a coherent wave. The classification scheme is shown in Fig.1.2.

The regime $\Gamma_1, \Gamma_2 \ll 1$ is classified as weak turbulence and the other regimes are arbitrarily referred to as strong turbulence of one form or other, although as Drummond and Ross admit, 'coherent turbulence' is perhaps a contradiction in terms. However the initial nonlinear saturation of collective fluctuations in certain situations may well consist of coherent oscillations.

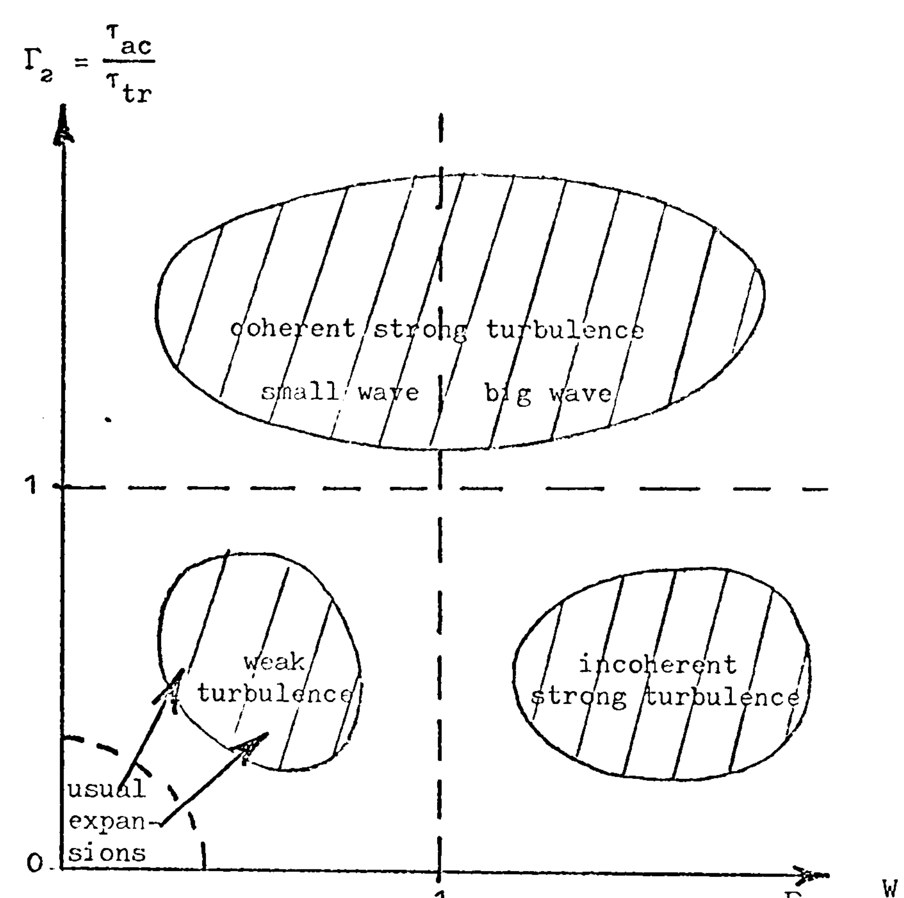

Fig.1.2
Classification of plasma turbulence after Drummond and Ross (op.cit.)

Theoretical models for the strongly turbulent regimes cannot be derived from weak turbulence theory and so we must rely on experiments or numerical simulations to suggest and test theoretical hypotheses. In the work reported here the aim has been to experimentally excite the electron-ion two-stream instability which has very fast growth rates, $\gamma \gtrsim \omega$, so that we might obtain an insight into one aspect of strong plasma turbulence.

1.2 RESPONSE OF PLASMA TO A STEADY ELECTRIC FIELD

Consider a uniform electric field $\underline{E}_o$, applied to a plasma in thermal equilibrium at time $t = 0$. Initially the electrons and ions are accelerated in opposite directions. The zero momentum frame of reference is approximately the ion rest frame because of the large ion-to-electron mass ratio M/m. Thus the current conducted by the plasma is almost entirely due to the electron drift motion. The equation for the electron drift velocity v_d, (parallel to $\underline{E}_o$), can be expressed as:

$$\frac{dv_d}{dt} = -\frac{eE_o}{m} - \nu_{eff}\, v_d \qquad \ldots (1.7)$$

where ν_{eff} is the effective collision frequency of the interaction by which the electrons lose momentum to the ions.

If $|\nu_{eff} v_d| \ll \left|\frac{eE_o}{m}\right|$ then the plasma response is <u>inductive</u>, i.e. the current density $J = -nev_d$, is given by:

$$\frac{dJ}{dt} \simeq \frac{ne^2}{m} E_o$$

which, for a voltage drop V, across a plasma of length ℓ, and area A, leads to

$$\left.\begin{aligned} V &= -L\frac{dI}{dt} \\ \text{where the inertial inductance, } L &= \frac{m\ell}{ne^2A}\, . \end{aligned}\right\} \qquad \ldots (1.8)$$

However if a steady state is reached such that $\frac{dv_d}{dt} = 0$, then the plasma is <u>resistive</u> with a conductivity

$$\sigma = \frac{ne^2}{m}\frac{1}{\nu_{eff}}\, . \qquad \ldots (1.9)$$

If a steady state is reached while the plasma is very close to thermal equilibrium, then ν_{eff} will be dominated by the binary collisions discussed in the previous section. An estimate for ν_{eff} would then be ν_c in equation (1.4), however we quote here a result of calculations reported in the literature, (see Clemmow and Dougherty, pp.376-377 and references therein),

$$\frac{\sigma}{4\pi\epsilon_0} = 7.43 \frac{N_D \, \omega_{pe}}{\log \Lambda} \quad . \qquad \ldots (1.10)$$

DREICER (1956) pointed out that for sufficiently large E_o, the binary collisions would not stabilise v_d because the Rutherford scattering cross-section for two particles with relative velocity v, diminishes as $1/v^4$. His calculations show that the electrons freely accelerate if,

$$E_o > E_{Dr} .$$

The critical field E_{Dr}, can be expressed in the form:

$$E_{Dr} = \frac{m v_e \nu_c}{e} \propto \frac{n}{KT} \qquad \ldots (1.11)$$

where v_e is the electron thermal velocity* and an estimate of ν_c is given by equation (1.4). Thus if the electrons are accelerated to $v_d \geqslant v_e$ before one binary collision time, the phenomenon of electron runaway occurs. If initially $E_o < E_{Dr}$, the electrons are heated by binary collisions until $E_o > E_{Dr}$ so that electron runaway eventually occurs for weak fields; an unfavourable consequence for controlled thermonuclear fusion since it appears impossible to heat plasmas to high temperatures by passing electric currents through them.

Such a treatment ignores the possibility of collective fluctuations limiting v_d when the plasma is no longer in thermal equilibrium. BUNEMAN (1958,1959) suggested that the electron-ion two-stream instability, which occurs with fast growth rates for $v_d \gg v_e$, would produce a turbulent spectrum of collective fluctuations involving both ions and electrons, thereby greatly increasing ν_{eff} from the value in equation (1.4). (In general various instabilities can occur when electrons drift relative to ions; these are discussed in Chapter II.)

---

* In general we shall define v_e as the root mean square electron velocity which for a one-dimensional Maxwellian distribution is $\sqrt{KT/m}$.

Experimentally it is found that when $E_o \gg E_{Dr}$, instabilities occur and appear to prevent runaway. The plasma becomes resistive with a conductivity much lower than (1.10) and, consistent with this, electron and ion heating have been observed accompanied by a non-thermal level of fluctuations and electromagnetic radiation; the phenomenon is known as turbulent heating.

Although there is further comment on these experiments in Chapter VI, we mention here the particular results of HAMBERGER and FRIEDMAN (1968). They found that for three different ion masses, hydrogen, argon and xenon, in a sufficiently strong electric field, σ could be represented by the empirical formula :

$$\frac{\sigma}{4\pi\epsilon_o} = (0.45 \pm 0.04)\left(\frac{M}{m}\right)^{0.3\pm0.1} \omega_{pe} . \qquad \ldots (1.12)$$

It is instructive to compare equation (1.12) with (1.10), viz :

$$\frac{\sigma_a}{\sigma_c} \sim \left(\frac{M}{m}\right)^{\frac{1}{3}} \frac{\log N_D}{N_D} \qquad \ldots (1.13)$$

where σ_a is the 'anomalous' conductivity measured in this experiment and σ_c is the 'classical' conductivity for a plasma in thermal equilibrium. For $N_D \gg 1$ not only can the estimates differ by orders of magnitude, but the parameter scalings are very different.

The measurements for scaling (1.12) were taken under conditions where the electron-ion two-stream instability was expected to be excited. Hamberger and Friedman (op.cit.) point out that the corresponding

$$\nu_{eff} \simeq \frac{1}{2\pi}\left(\frac{m}{M}\right)^{\frac{1}{3}} \omega_{pe} ,$$

is related to the characteristic frequency of the linear stages of this instability, (see Chapter II). Unfortunately this experiment suffered from difficulties of detailed interpretation. In general large pulsed experiments can only be made once every minute or so. It is difficult to achieve precise reproducibility from pulse to pulse so that a temporal resolution of the experimental data is very difficult. In particular it is difficult to measure unambiguously the evolution of n, v_d and v_e.

These problems suggested a simpler experiment to study the strong current-driven turbulence arising from the electron-ion two-stream instability.

A single-ended Q-machine continuously produces a uniform, cylindrical, (diameter ~ 3 cm), potassium plasma column between two end-plates (~ 1 m apart) within a uniform, axial magnetic field (~ 2 kG). Under suitable operating conditions, ($n < 10^{10}$ cm^{-3}, $T \sim 2{,}500$ K) the plasma is close to thermal equilibrium and it is possible to draw large pulsed electron currents ($v_d > v_e$), of duration $\leqslant 10\ \mu s$ with repetition rates $\leqslant 1$ kHz by applying pulsed potential differences of $\leqslant 100$ V between the two end plates with a pulse generator.

This arrangement has considerable advantages. The initial conditions for each pulse are well defined and reproducible. It should be possible to follow the detailed evolution of the plasma from the known initial conditions by using pulsed voltages rather than d.c. voltages, (this point concerns the magnitude of various timescales which will be considered in Chapter III). The fast repetition rate permits the use of electronic sampling techniques to measure ensemble averages over many pulses, a useful type of measurement for turbulent plasmas.

The experiment has a serious disadvantage compared with the toroidal or mirror magnetic confinement schemes used in other experiments, in that the energy confinement time is very short due to the column end losses. However, providing this is kept in mind, with such an experiment we should hope to study in more detail the initial processes that occur in a particular case of strong current-driven plasma turbulence.

In Chapter II the various current-driven instabilities that can be excited in the experiment are discussed in detail, mainly in the context of linear theory. In Chapter III the experiment is described with measurements of the macroscopic plasma parameters. Chapter IV describes a novel but important technique which provides unambiguous time-resolved measurements of n, v_d and v_e.

In Chapter V there are measurements concerning the observed turbulent fluctuations and Chapter VI concludes with an overall discussion of the results in comparison with other work and suggestions for future work.

CHAPTER II

CURRENT-DRIVEN ELECTROSTATIC INSTABILITIES

2.1 INTRODUCTION

In this chapter we review the linear theory concerning the various instabilities that occur when electrons drift through ions in a warm plasma column with an axial magnetic field. Initially we consider the dispersion relation $D(\omega, k) = 0$, for collective oscillations $\propto \exp i(\underline{k} \cdot \underline{r} - \omega t)$, that exist in a cold one-dimensional (1-D) plasma where the only instability that can occur is the electron-ion or current-driven two-stream instability. The complications introduced by magnetic field, cylindrical geometry and temperature are discussed in turn, leading to the conclusion that in the experiment, the fastest growing instability can be described to a good approximation by the simple 1-D theory with minor modifications. The chapter concludes with a comment on the nonlinear development of the current-driven two-stream instability and in particular why it is expected to excite strong turbulence.

The linear theory is based on two assumptions: (a) the plasma is 'collisionless', i.e. the collective fields are determined by equations (1.2), and (b) because the strong interaction between fluctuating fields $\underline{\tilde{E}}$, and the particles occurs for $\omega/k \ll c$, $\underline{\tilde{E}}$ can be considered in the electrostatic approximation, viz. $\underline{E} = -\underline{\nabla}\varphi$. When a steady magnetic field $\underline{B}_0$, is present a further consequence of (b) is that ω/k must be much smaller than the Alfven speed, $\sqrt{B_0^2/\mu_0 n M}$.

The general method of deriving $D(\omega, k)$ is to consider the plasma as a dielectric by including the self-consistent fields in the formulation of the plasma dielectric tensor $\underline{\underline{\epsilon}}(\omega, k)$, (see e.g. STIX, (1962) chapter I). Thus in the electrostatic approximation we solve Laplace's equation:

$$\underline{\nabla}(\underline{\underline{\epsilon}} \cdot \underline{\nabla}\varphi) = 0 \qquad \ldots (2.1)$$

with appropriate boundary conditions.

The general expression for $\underline{\underline{\epsilon}}$ is very complicated but we shall restrict the disccusion to approximations which are developed in the following sections.

2.2 COLD, ONE-DIMENSIONAL PLASMA

In 1-D, unbounded, cold plasma, equation (2.1) becomes, (Stix, op. cit.)

$$\epsilon_{33} = 0 .$$

Substituting for ϵ_{33} we have ,

$$D(\omega,k) = 1 - \frac{\omega_{pe}^2}{(\omega - kv_d)^2} - \frac{\omega_{pi}^2}{\omega^2} = 0 \quad . \qquad \ldots (2.2)$$

Solving equation (2.2) in terms of complex-ω for real-k always predicts growing oscillations (i.e. $\varphi \propto e^{\gamma t}$), if $v_d \neq 0$; this is the electron-ion two-stream instability. BUNEMAN (1958) computed the growth rates γ, using an approximation which can be shown to require

$$\left(\frac{m}{M}\right)^{\frac{1}{3}} \ll 1 ,$$

(there is a detailed discussion of these solutions in Appendix A.1). The maximum growth rate γ_{max}, is given by

$$\gamma_{max} = \frac{\sqrt{3}}{2^{4/3}} \left(\frac{m}{M}\right)^{\frac{1}{3}} \omega_{pe} \simeq 0.69 \ \omega^*$$

and occurs at, real frequency

$$\omega_r = \frac{1}{2^{4/3}} \left(\frac{m}{M}\right)^{\frac{1}{3}} \omega_{pe} \simeq 0.4 \ \omega^* \qquad \ldots (2.3)$$

and real

$$k = \frac{\omega_{pe}}{v_d}$$

where

$$\omega^* \equiv \left(\frac{m}{M}\right)^{\frac{1}{3}} \omega_{pe} .$$

The solution for γ is shown in Fig.2.1(a) and the complete solution for equation (2.2) is sketched in Fig.2.1(b).

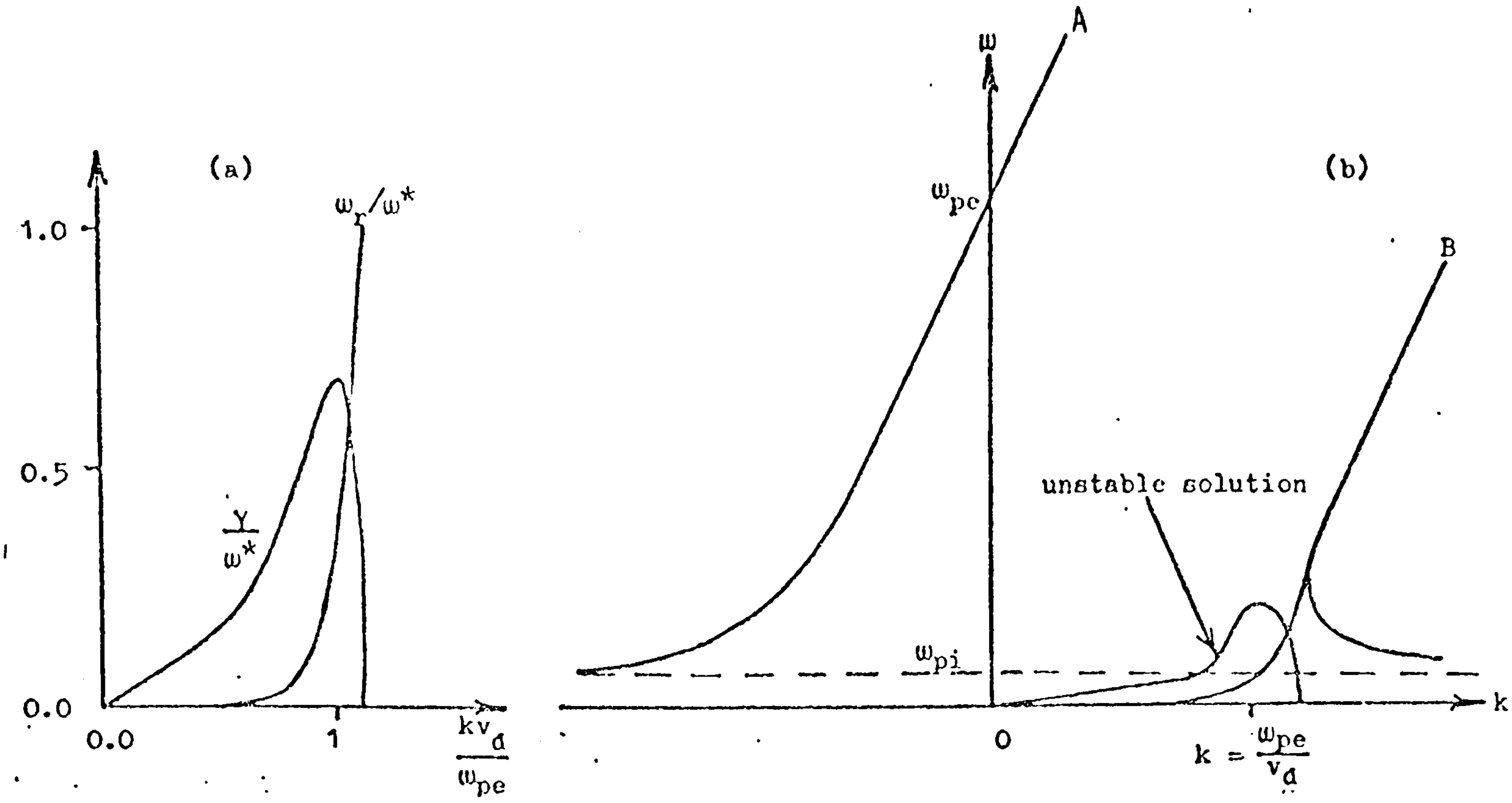

Fig.2.1
Dispersion relation for the electron-ion two-stream instability in the ion rest frame (solution to equation 2.2)
(a) Unstable part of solution (for hydrogen plasma)
(b) Complete solution (schematic)

Branches A and B in Fig.2.1(b) for $\omega \gg \omega_{pi}$ represent the fast and slow waves of the electron plasma oscillations which propagate undamped in a cold plasma. (The complete complex-ω solutions of equation (2.2) are complex conjugates, but the damped solution has been omitted from Fig.2.1). Notice that in the ion rest frame the amplitude of the fastest growing wave increases by $\exp(2\pi\sqrt{3}) \simeq 5 \times 10^{5}$, in one oscillation period $2\pi/\omega_r$.

2.3 COLD PLASMA IN CYLINDRICAL GEOMETRY WITH AN AXIAL MAGNETIC FIELD

A plasma contained within a hollow cylindrical conductor by a uniform axial magnetic field $(0,0\ B_z)$, will have a discrete set of eigenmode solutions propagating as $\exp(i k_z z)$ for a given ω. To obtain these we solve (2.1) in cylindrical polar coordinates (r, θ, z), considering first of all the idealised model of a uniform cold plasma completely filling a cylindrical waveguide of radius, a . The boundary conditions are :

$$\left.\begin{aligned} \varphi(r, \theta, z)\Big|_{r=a} &= 0 \\ \varphi(r, \theta, z) &= \varphi(r, \theta \pm 2\pi\mu, z) \end{aligned}\right\} \qquad \ldots (2.4)$$

where μ is an integer .

For a cold plasma in a magnetic field with drifting electrons and stationary ions $(v_d \parallel B_z)$, $\underline{\underline{\epsilon}}$ takes the form, (see e.g. KRALL and TRIVELPIECE (1973) p.179) ,

$$\underline{\underline{\epsilon}} = \begin{pmatrix} \epsilon_1 & +i\epsilon_2 & 0 \\ -i\epsilon_2 & \epsilon_1 & 0 \\ 0 & 0 & \epsilon_3 \end{pmatrix}$$

where

$$\epsilon_1 = 1 + \frac{\omega_{pe}^2}{\omega_{ce}^2 - (\omega - k_z v_d)^2} + \frac{\omega_{pi}^2}{\omega_{ci}^2 - \omega^2}$$

$$\epsilon_2 = \frac{\omega_{ce}}{\omega} \frac{\omega_{pe}^2}{\omega_{ce}^2 - (\omega - k_z v_d)^2} - \frac{\omega_{ci}}{\omega} \frac{\omega_{pi}^2}{\omega_{ci}^2 - \omega^2}$$

$$\epsilon_3 = 1 - \frac{\omega_{pe}^2}{(\omega - k_z v_d)^2} - \frac{\omega_{pi}^2}{\omega^2} \qquad \ldots (2.5)$$

where $\omega_{ce} = \frac{eB_z}{m}$ and $\omega_{ci} = \frac{eB_z}{M}$.

Substitution of equations (2.5) into (2.1) using the boundary conditions (2.4) leads to eigenfunctions * :

$$\varphi = \varphi_o \, J_\mu \left(p_{\mu\nu} \frac{r}{a}\right) e^{i\mu\theta} \, e^{i(k_z z - \omega t)} \qquad \ldots (2.6)$$

with a dispersion relation for each eigenmode of the form

$$-\frac{\epsilon_1}{\epsilon_3} = \left(\frac{k_z a}{p_{\mu\nu}}\right)^2 \equiv K^2 \qquad \ldots (2.7)$$

where $p_{\mu\nu}$ is the ν^{th} root of the μ^{th}-order Bessel's function of the first kind, (see KRALL and TRIVELPIECE (op.cit.) p.202).

The concise form of equation (2.7) can be written explicitly in terms of ω :

$$D(\omega, k_z) = 1 + \frac{1}{1+K^2} \left\{ \frac{\omega_{pe}^2}{(\omega_{ce}^2 - (\omega - k_z v_d)^2} + \frac{\omega_{pi}^2}{\omega_{ci}^2 - \omega^2} \right\} - \frac{K^2}{1+K^2} \left\{ \frac{\omega_{pe}^2}{(\omega - k_z v_d)^2} + \frac{\omega_{pi}^2}{\omega^2} \right\} = 0 \qquad \ldots (2.8)$$

---

* (2.1) can be manipulated to produce a separation of the (r, θ, z) coordinates because $\underline{\underline{\epsilon}}$ contains the appropriate zeros and does not implicitly contain an (r, θ) dependence.

For a given eigenmode, equation (2.8) has four solutions of ω for real-k_z and hence the possibility of further instabilities. In Appendix A.2 we discuss the complete solution in an approximation represented by

$$\omega_{ce}^2 \gg \omega_{pe}^2 \gg \omega_{pi}^2 \gg \omega_{ci}^2 , \qquad \ldots (2.9)$$

which corresponds to the experimental conditions. This effectively means that the electrons are constrained to one-dimensional motion parallel to $\underline{B}$ whereas the ions are allowed motion in all three dimensions. This leads to an estimate of γ_{max} for each instability, the results of which show that the electron-ion two-stream instability has by far the fastest growth with a maximum value modified from the 1-D solution (2.3), to

$$\left.\begin{aligned} \gamma_{max} &\simeq 0.69\ \omega^* \left[1 - \left(\frac{p_{\mu\nu} v_d}{\omega_{pe} a}\right)^2\right]^{1/6} \\ \omega_r &= \gamma_{max}/\sqrt{3} \\ \text{and} \quad k_z &\simeq \frac{\omega_{pe}}{v_d}\left[1 - \left(\frac{p_{\mu\nu} v_d}{a\,\omega_{pe}}\right)^2\right]^{\frac{1}{2}} \end{aligned}\right\} \qquad \ldots (2.10)$$

The approximation applies for drift velocities which satisfy:

$$\left(\frac{p_{\mu\nu} v_d}{a\,\omega_{pe}}\right)^2 \ll 1 \quad . \qquad \ldots (2.11)$$

If the experimental conditions satisfy condition (2.11) for low order mode numbers, the cylindrical geometry has a negligible effect on the dispersion of these fast growing eigenmodes.

Since these wavelengths are very short compared to the radius, to a first approximation the plasma is effectively unbounded. We can then re-write solution (2.10) in a simpler form for these short wavelengths, (i.e. ignoring mode-discreteness), by introducing the angle of propagation α, the wave vector makes with the magnetic field, i.e.

$$\left.\begin{aligned} \sqrt{3}\ \omega_r = \gamma_{max} &= 0.69\,(\cos\alpha)^{\frac{1}{3}}\ \omega^* \\ |\underline{k}| = \frac{k_z}{\cos\alpha} &= \frac{\omega_{pe}}{v_d} \end{aligned}\right\} \qquad \ldots (2.12)$$

A plot of $(\cos\alpha)^{\frac{1}{3}}$ in Fig.2.2 shows that waves propagating at angles $\leq \pi/4$ to the direction of $\underline{B}$ have γ_{max} within 10% of the 1-D solution (2.3).

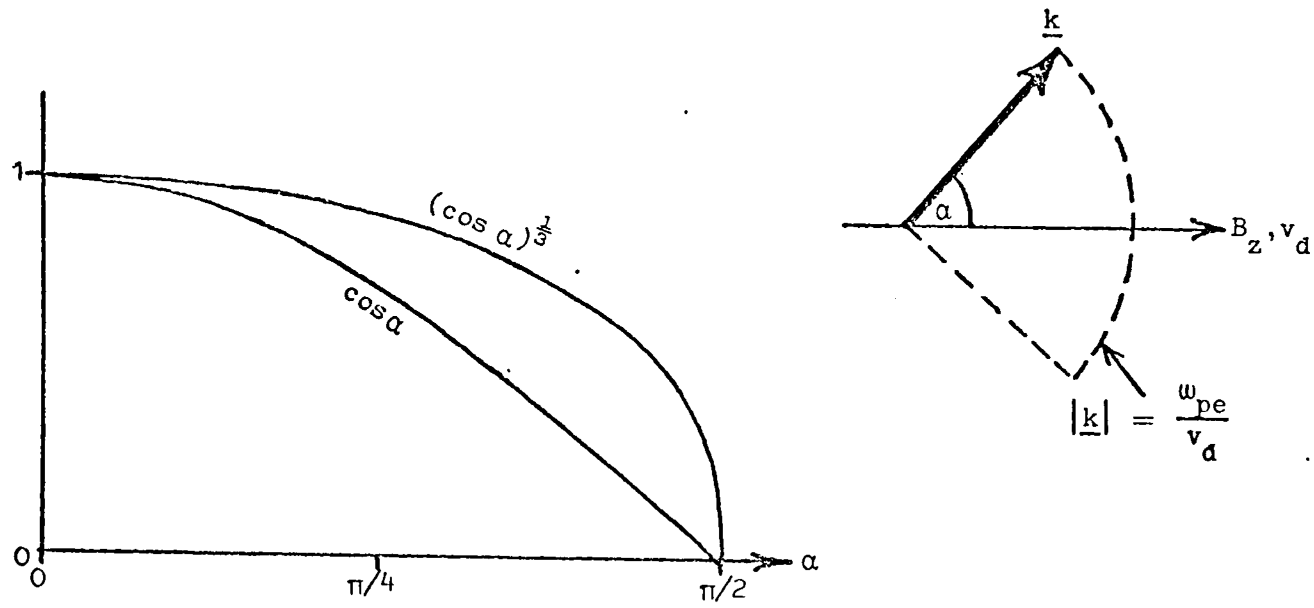

Fig.2.2
Angular dependence of propagation of the most unstable wavelengths for the two-stream instability in an unbounded cold plasma where : $\omega_{ce} \gg \omega_{pe} \gg \omega_{pi} \gg \omega_{ci}$

2.4 WARM PLASMA

We now consider the effects of finite temperature, starting as before with a 1-D treatment.

2.4.1 One-Dimensional Plasma

If we assume Maxwellian velocity distributions for each specie but with drifting electrons, then two further parameters become relevant; the electron thermal velocity v_e, and the electron-to-ion temperature ratio T_e/T_i. Finite temperature modifies the cold 1-D plasma in two ways; firstly there is a critical drift velocity below which the plasma is stable, and secondly there exists the slow-growing ion acoustic instability if $T_e \gg T_i$.

For a 1-D model, $D(\omega,k)$ can be derived from the linearised Vlasov-Maxwell equations (1.2) using the electrostatic approximation (2.1). This leads to :

$$D(\omega,k) = 1 - \frac{\omega_{pe}^2}{k^2}\int_{-\infty}^{+\infty} \frac{\frac{dF_e}{dv}\,dv}{(v-\omega/k)} - \frac{\omega_{pi}^2}{k^2}\int_{-\infty}^{+\infty} \frac{\frac{dF_i}{dv}\,dv}{(v-\omega/k)} = 0 \quad .. (2.13)$$

where $F_{i,e}(v)$ is normalised as follows,

$$\int_{-\infty}^{+\infty} F_{i,e}(v)\, dv = 1 \, . \qquad \ldots (2.14)$$

Care must be taken concerning the contours of integration in (2.13), (see e.g. Clemmow and Dougherty, chapter 8). For Maxwellian F(v), (2.13) can be normalised in terms of the electron and ion plasma frequencies and the Debye length λ_D, viz:

$$D(\omega,k) = 1 - \frac{1}{2(k\lambda_D)^2} Z'\left(\frac{\Omega_e - k\lambda_D V}{\sqrt{2}\, k\lambda_D}\right) - \frac{R^2}{2(k\lambda_D)^2} Z'\left(\frac{\Omega_i R}{\sqrt{2}\, k\lambda_D}\right) = 0 \qquad \ldots (2.15)$$

where

$$\Omega_e = \frac{\omega}{\omega_{pe}} \, , \quad \Omega_i = \frac{\omega}{\omega_{pi}}$$

$$V = \frac{v_d}{v_e} = \frac{v_d}{\sqrt{\frac{KT_e}{m}}} \, , \quad R = \sqrt{\frac{T_e}{T_i}}$$

$$Z'(\zeta) = \frac{2}{\sqrt{\pi}} \int_{-\infty}^{+\infty} \frac{z \exp(-z^2)}{(\zeta - z)}\, dz \, .$$

$Z'(\zeta)$ is the derivative of the Plasma Dispersion Function which has been tabulated by FRIED and CONTE (1961).

JACKSON (1960) considers $T_e = T_i$ and shows that for instability v_d must exceed some critical value, i.e.

$$v_d > v_{crit} = 1.308 \left(1 + \sqrt{\frac{m}{M}}\right) v_e \, . \qquad \ldots (2.16)$$

His solutions of ω_r and γ for three values of v_d/v_e are shown in Fig.2.3, demonstrating how quickly the solutions approach the cold plasma solution for large v_d.

Notice that, for even the modest value $v_d = 3.1\, v_e$, the maximum amplification during one period of oscillation is $\sim 3 \times 10^3$.

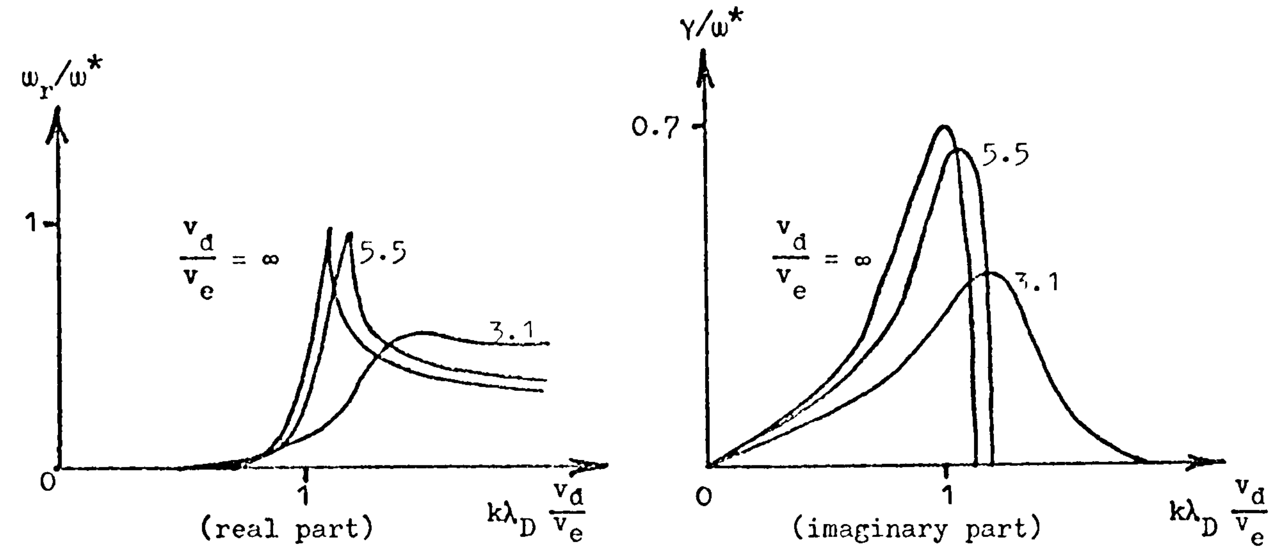

Fig.2.3
Unstable solutions of the electron-ion two-stream instability for a one-dimensional warm hydrogen plasma, $T_e = T_i$ after Jackson (op. cit.)

STRINGER (1964) presents solutions of equation (2.15) over a wide range of parameters. He finds that, for $T_e > T_i$, v_{crit} is reduced from the value in equation (2.16) and for $T_e \gg T_i$ becomes $\sim c_s = \sqrt{\frac{KT_e}{M}}$, the ion acoustic speed. In this situation, if v_d is between c_s and v_e, the instability has a different nature, i.e. unstable ion acoustic oscillations with slow growth rates $\gamma_{max} \ll \omega_r < \omega_{pi}$. However if $v_d > 1.3\, v_e$, fast growing oscillations occur, $\gamma_{max} \gtrsim \omega_r > \omega_{pi}$, which are characteristic of the electron-ion two-stream instability. Fig.2.4 shows how γ_{max} varies with T_e/T_i and v_d/v_e.

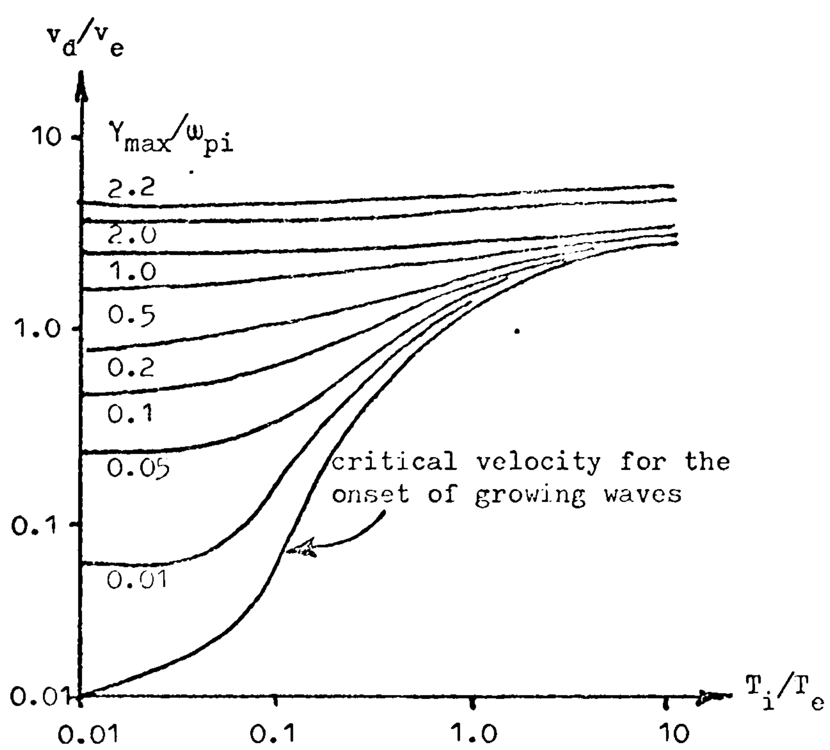

Fig.2.4
Growth rate of fastest growing wave in a current-carrying plasma (after Stringer, op. cit.)

In the experiment the initial conditions are $T_e \simeq T_i$ so that we do not expect to excite the slow-growing ion acoustic instability in the early stages.

2.4.2 The Experimental Plasma

The plasma column used in the experiment is shown schematically in Fig.2.5.

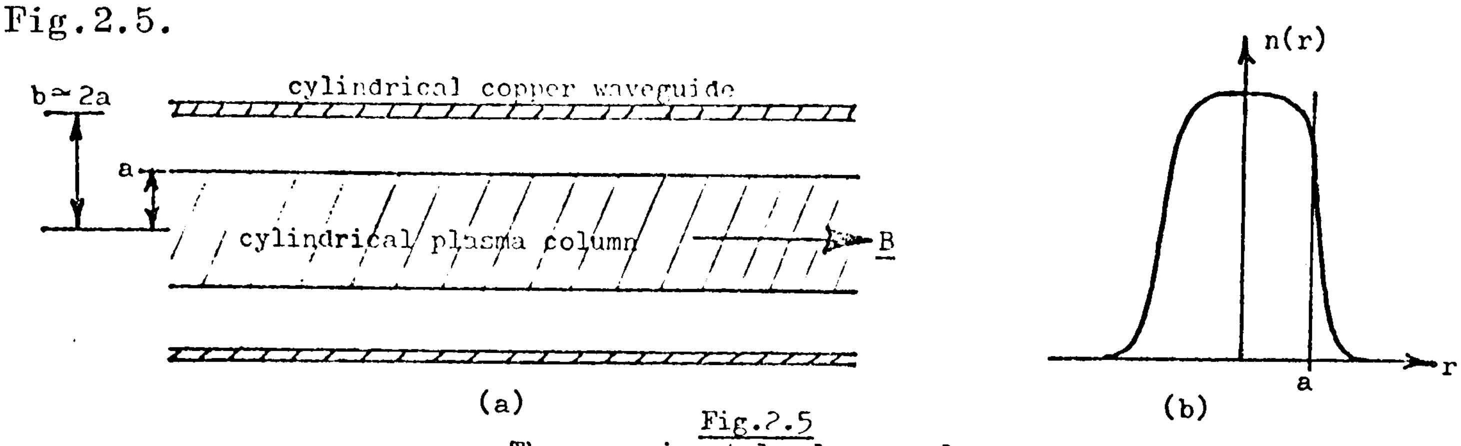

Fig.2.5
The experimental plasma column
(a) radial boundary conditions
(b) density profile

The radial density gradient at the column edge introduces the possibility of current-driven drift wave instabilities, (see e.g. HENDEL and YAMADA (1974)), but the boundary conditions do not substantially alter $D(\omega,k)$ from the completely filled plasma waveguide case discussed in section 2.3 and Appendix A.2. Finite temperature effects all the instabilities in various ways, but because of the ordering (2.9) they are slowly growing, $\gamma \ll \omega_r$, and have low frequency, $\omega_r \ll \omega_{pi}$, when compared with the electron-ion two-stream instability.

In the experiment the two characteristic scalelengths, a and λ_D are well separated, viz :

$$a \gg \lambda_D \qquad \ldots (2.17)$$

Thus with moderate drift velocities, it is possible to satisfy conditions (2.16) and (2.11) simultaneously, viz :

$$\frac{a}{p_{\mu\nu}} \gg \frac{v_d}{\omega_{pe}} > 1.3\ \lambda_D \ . \qquad \ldots (2.18)$$

In this situation the electron-ion two-stream instability is approximately described by the simple cold plasma theory in section 2.2 with two modifications; a critical drift velocity given by (2.16) if $T_e = T_i$, and wave propagation at an angle to the cylindrical axis as given by equation (2.12).

Finally, because of their importance in Chapter IV, we comment on the dispersion of the stable electron plasma waves in the plasma column, i.e. branches A and B in the cold 1-D plasma, Fig.2.1(b). The modification to $D(\omega,k)$ by the electron temperature and the cylindrical geometry is discussed in detail in Appendix A.3, however, for the sake of completeness we show in Fig.2.6 the dispersion of the (0,0) mode of electrostatic oscillations that occur in a warm plasma column with $T_e = T_i$ and electrons drifting, $v_d > 1.3\ v_e$, with respect to stationary ions.

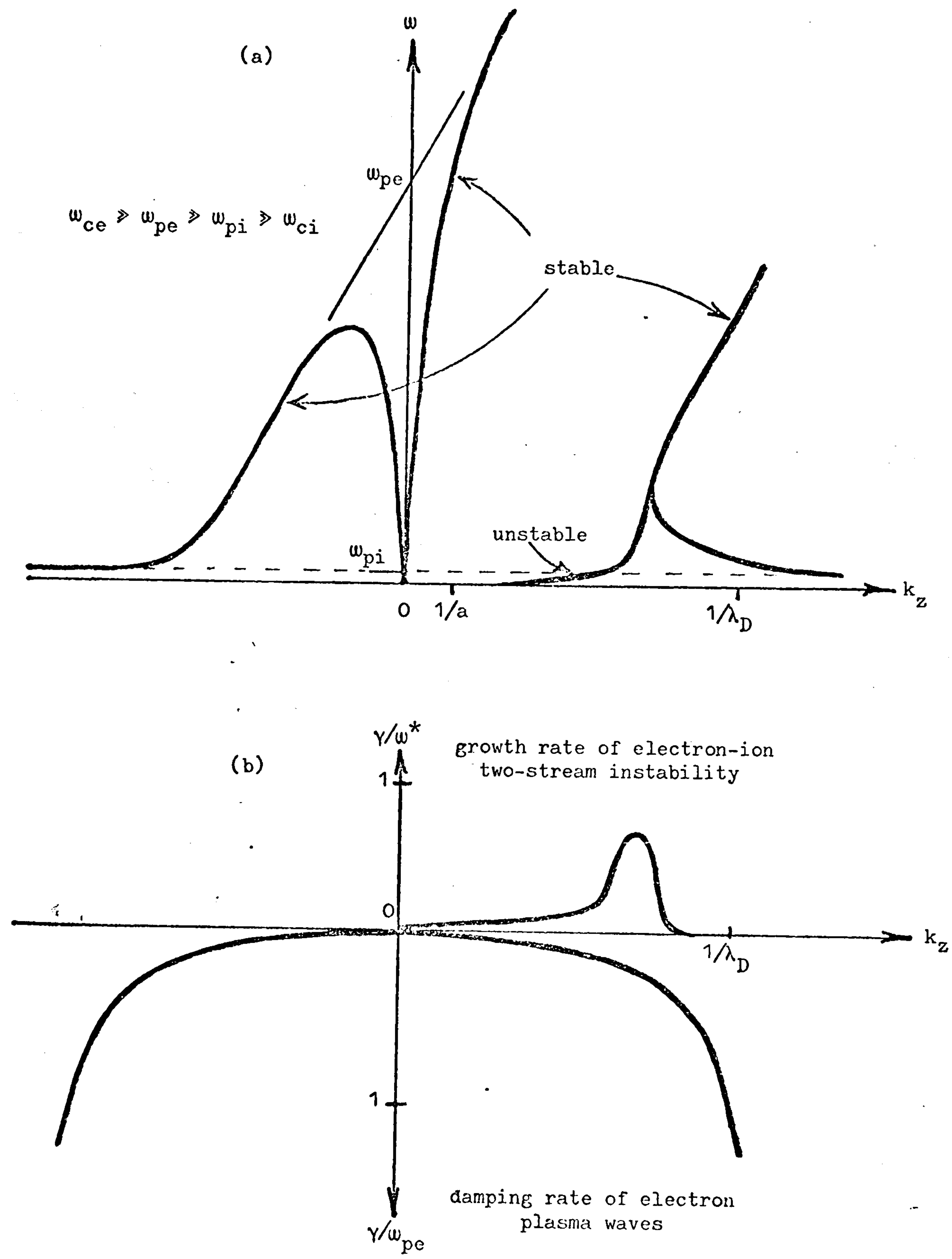

Fig.2.6
The dispersion of the (0,0) mode of electrostatic oscillations which occur in a plasma column with $T_e = T_i$, electrons drifting, $v_d > 1.3\ v_e$, with respect to stationary ions in the frequency range $\omega_{ce} \gg \omega \gg \omega_{pi}$

(a) real part of ω ; (b) imaginary part of ω

2.5 FURTHER COMMENTS

2.5.1 Electron Acceleration in a Steady Field E_o

The linear theory so far has assumed a steady drift velocity, whereas in the experiment the electrons are accelerated from thermal equilibrium by a steady electric field E_o. Thus initially

$$v_d = -\frac{eE_o t}{m} . \qquad \ldots (2.19)$$

In the cold fluid theory γ, for a given unstable wavelength $2\pi/k$, is a function of (kv_d) so that as the electrons accelerate the growth rate of a wave k, will vary in time. We can use the results of cold fluid theory to estimate the growth after v_d has reached a sufficient magnitude such that

$$\left| \frac{1}{v_d} \frac{dv_d}{dt} \right| \ll \gamma , \qquad \ldots (2.20)$$

i.e. this means that the rate of change of the growth rate is much slower than the growth rate itself. If the amplitude of the wave in thermal equilibrium is $\tilde{\varphi}_k(0)$, then at time t, the amplitude is:

$$\tilde{\varphi}_k(t) \approx \tilde{\varphi}_k(0)\ e^{\int_0^t \gamma(t')dt'} . \qquad \ldots (2.21)$$

Physically, when v_d becomes $> 1.3\ v_e$ a wide range of wavelengths are unstable, i.e. $0 < k \leqslant \frac{\omega_{pe}}{v_d}$. For wavelengths $\gg \lambda_D$, γ begins at a low value, since $k \ll \frac{\omega_{pe}}{v_d}$, but as v_d increases, γ increases to γ_{max} when $k \simeq \frac{\omega_{pe}}{v_d}$. After this, γ rapidly drops to zero and the wave stops growing, (see Fig.2.1(a)); most of the growth has occurred when $\gamma < \gamma_{max}$. This point was made by SISOMENKO and STEPANOV (1971). In Appendix A.1, we show that an estimate of the right-hand-side of (2.21) is:

$$\left.\begin{aligned} \tilde{\varphi}_k(t) &\approx \tilde{\varphi}_k(0)\ e^{\eta\,\omega_{pi} t} \quad \text{where} \quad \eta \sim 1 \\ \text{for} \quad t &\approx \frac{m\,\omega_{pe}}{eE_o k} \end{aligned}\right\} . \qquad \ldots (2.22)$$

Thus an unstable wavelength $2\pi/k$, will reach a maximum amplitude :

$$\left.\begin{array}{ll} & \tilde{\varphi}_k(\max) \approx \tilde{\varphi}_k(0)\ \exp \dfrac{m\,\omega_{pe}\,\omega_{pi}}{e\,E_o\,k} \\ \text{at time} & t \approx \dfrac{m\,\omega_{pe}}{e\,E_o\,k} \end{array}\right\} . \qquad \ldots (2.23)$$

The timescale ω_{pi}^{-1}, implied by estimate (2.22) is the characteristic growth time of the electron-ion two-stream instability when driven by a steady field. For this argument to be valid, E_o must be sufficiently large so that the electrons are accelerated beyond the threshold $1.3\ v_e$, in a time $\leqslant \omega_{pi}^{-1}$. By analogy with the Dreicer field E_{Dr}, which was introduced in section 1.2, we define E_c :

$$E_c = \frac{m\,\omega_{pi}\,v_e}{e} \qquad \ldots (2.24)$$

Notice that $\qquad E_c \gg E_{Dr} \quad \text{if} \quad N_D \gg \sqrt{M/m}$.

In this context we will term those fields for which $E_o > E_c$ as <u>strong</u> fields. The maximum amplitude (2.23) is related to E_o/E_c by:

$$\tilde{\varphi}_k(\max) \approx \tilde{\varphi}_k(0)\ \exp \frac{1}{\dfrac{E_o}{E_c}\,.\,k\lambda_D} . \qquad \ldots (2.25)$$

Stepanov and Sizonenko (op.cit.) claim that the growth rate (2.22) is not sufficient to stabilise v_d by nonlinear particle motions parallel to the drift. At this stage we note that provided <u>sufficiently long wavelengths</u> can propagate in the plasma, it is possible to find a wave whose <u>linear</u> growth is $\propto e^{\omega_{pi}t}$ for many ion plasma periods, whereas the drift is $\propto t$. Whether or not growth will be maintained at this rate to sufficiently large amplitudes will be discussed in the next section.

2.5.2 Nonlinear Development; A Comparison with the Beam-Plasma Two-Stream Instability

As was pointed out in Chapter I, a systematic theory for the nonlinear development of the fast-growing two-stream instability does not appear possible; at present theoretical progress can only be achieved by making a priori assumptions about the nonlinear state. In this respect some progress has been made with the beam-plasma two-stream instability for which the linear 1-D theory is closely related to the electron-ion two-stream instability. That is, $D(\omega,k)$ for a weak, cold electron beam, (density n_b, temperature T_b, and drift v_d), penetrating a warm electron plasma (n_o, T_o), is identical to equation (2.15) provided the substitutions

$$\frac{n_b}{n_o} \rightarrow \frac{m}{M} \quad \text{and} \quad \frac{T_b}{T_o} \rightarrow \frac{m}{M}\frac{T_i}{T_e}$$

are made and the frame of reference is changed from the ion 'beam' frame to the 'warm' electron frame, (γ is the same in either frame but ω_r is Doppler shifted by $\pm kv_d$).

The initial nonlinear saturation of the beam-plasma instability has been explained by a particle trapping theory (see O'NEIL et al. (1971)). The phenomenological description is that the fastest growing wave $(k \simeq \frac{\omega_{pe}}{v_d})$, dominates the $\underline{\tilde{E}}$ spectrum after a few oscillation periods and its amplitude $\tilde{\varphi}_o$, grows until, when viewed in an inertial frame travelling at the phase velocity of the wave k, beam electrons are reflected by the potential minima, i.e. the beam electrons begin to be 'trapped' by the wave. In Fig.2.7 we show the velocity distributions of both sets of particles as seen in the wave frame.

The onset of trapping of the beam electrons occurs when

$$2e\tilde{\varphi}_o = \tfrac{1}{2}m(\Delta v)^2$$

where

$$\Delta v = \frac{1}{2^{4/3}}\left(\frac{n_b}{n_o}\right)^{\frac{1}{3}} v_d \qquad \left(v_d \gg 1.3\sqrt{\frac{KT_o}{m}}\right)$$

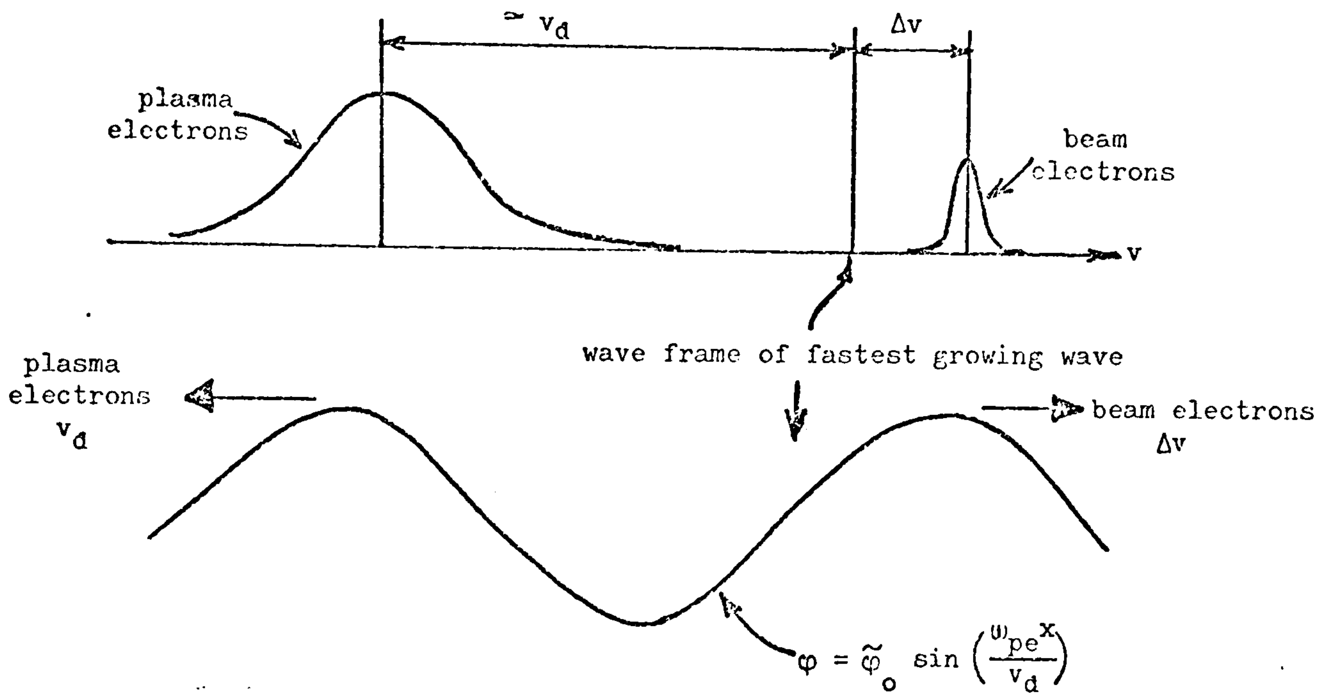

Fig.2.7
Velocity distribution of beam-plasma instability as seen from the frame of reference of the fastest growing wave

The energy density W, of the collective oscillation is then :

$$W_t = \tfrac{1}{2}\,\epsilon_o\,\tilde{E}^2 = \frac{1}{2^9}\left(\frac{n_b}{n_o}\right)^{4/3} n_o\, m\, v_d^2 \;.$$

In an earlier heuristic treatment, Drummond et al. (1970) predict a time assymptotic value of $W = 512\, W_t$. Using this value, we can estimate the parameter Γ_1 introduced in Chapter I, i.e.

$$\Gamma_1 \sim 10^{-8} \qquad \text{for} \qquad v_d \gtrsim \left(\frac{KT_o}{m}\right)^{\frac{1}{2}}$$

and n_b/n_o = electron-to-ion mass ratio for potassium. Since $\Gamma_2 \gg 1$, this theoretical model is an example of 'small wave, coherent turbulence', (see Fig.1.2). There is experimental evidence to support this picture for the initial amplitude saturation of the beam-plasma instability, (GENTLE and LOHR (1973)).

We should not expect the same phenomenon to occur in the electron-ion two-stream instability because the beam in this case consists of massive ions.

Thus for the onset of ion trapping,

$$2e\tilde{\varphi}_o = \tfrac{1}{2}M(\Delta v)^2$$

$$= \frac{1}{2^{8/3}}\left(\frac{M}{m}\right)^{\frac{1}{3}}\tfrac{1}{2}\,m v_d^2$$

For potassium ions, $$2e\tilde{\varphi}_o \simeq 6.6\,\tfrac{1}{2}m v_d^2$$

whereas the onset for trapping the warm electrons is

$$2e\tilde{\varphi}_o \sim \tfrac{1}{2}m v_d^2 .$$

Hence if $\tilde{\varphi}_o$ can grow to a sufficient amplitude it will trap the electrons before effecting the ion 'beam', so that $\Gamma_1 \sim 1$. However the growth rates calculated from linear theory are only valid for :

$$e\tilde{\varphi}_o \ll m v_d^2$$

(see Appendix A.1). Thus it is not certain that potential fluctuations can grow to sufficient amplitudes for trapping to be a nonlinear mechanism. Further comment on various nonlinear theories is made in Chapter VI. We conclude that although the predictions of γ from linear theory for the beam-plasma and the electron-ion two-stream instabilities are the same, their nonlinear developments are very different. In particular we might expect the electron-ion two-stream instability to generate a high level of collective fluctuations ($\Gamma_1 \sim 1$).

CHAPTER III

THE EXPERIMENT

3.1 THE PLASMA

The plasma device used for these experiments is the single-ended Q-machine 'THESEUS' which has been built at the UKAEA Culham Laboratory. The large amount of research experience that has been gained on this type of plasma over the last fifteen years is reviewed in the book '<u>Q-Machines</u>' by R.W. MOTLEY (1975). In this chapter we mention only those details relevant to this work.

The experiments are performed on a thermally ionized, potassium plasma column, radially confined by a strong (1 – 4 kG), uniform, axial magnetic field. The experimental arrangement is shown schematically in Fig.3.1.

Diagnostic access to the plasma is by electrostatic probes that can move either axially along the column or radially across the column or remain fixed at various positions in the column. Constructional details of these will be given where necessary in later sections.

Plasma is synthesised in a water-cooled ($\sim 15^{o}$C), evacuated (background pressure $\leqslant 5\times10^{-7}$ torr) stainless steel tube, internal diameter 15 cm, at a single grounded tungsten plate 6 mm thick and 25 mm diameter which is heated by electron bombardment on its back surface. The temperature of the front surface can be maintained between 2200^{o}K and 2600^{o}K and is kept uniform to within 100^{o}K by using the spiral shaped filaments shown in Fig. 3.1 as the source of bombarding electrons.

The electrons are produced by thermionic emission and the ions by surface ionization of potassium vapour. This vapour is produced in a thermostatically controlled oven, collimated into a uniform beam which is then directed on to the tungsten hot plate. For a reason that will become

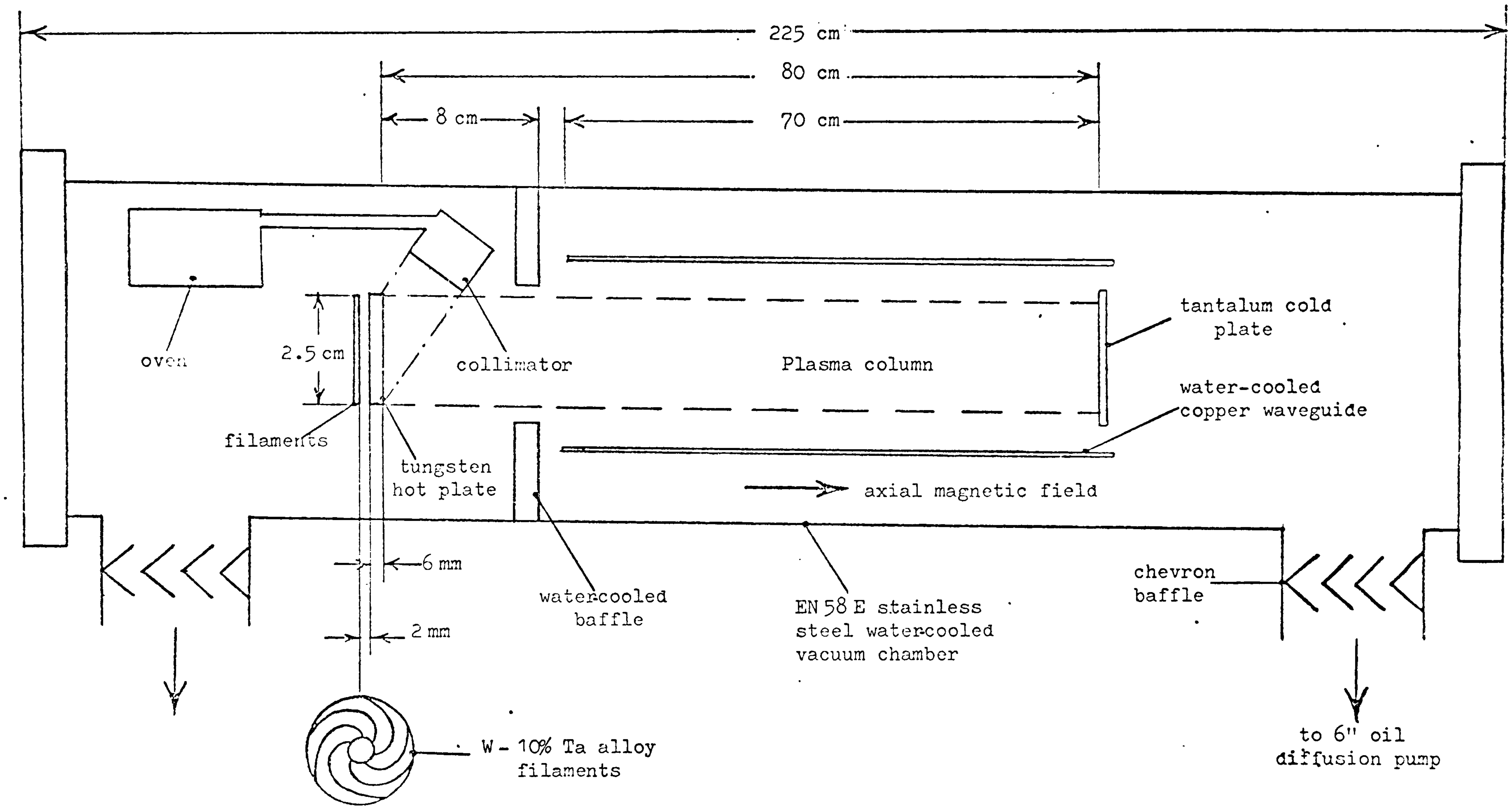

Fig.3.1
Schematic diagram of THESEUS single-ended Q-machine

clear in section 3.2, the flux of electrons leaving the ionizing surface is much greater than the flux of ions, so that the electron-rich space charge sheath between the hot plate and the plasma causes the plasma potential to be ~ -1 V with respect to ground. The column is terminated 80 cm from the hot plate by a cold, plane, tantalum disk which is d.c. isolated from ground. This plate reflects all but the fastest electrons so that the quiescent $F_e(v_z)$ is almost a complete 1-D Maxwellian with a temperature T_e, equal to the hot plate temperature T, (see SMITH (1971)). The ions are accelerated into the plasma by the electron-rich sheath at the hot plate and absorbed at the cold plate so that $F_i(v_z)$ has a drift velocity in the plasma column. Measurements of the ion energy distribution, (ANDERSON et al (1971), CLARK (1972)), indicate that $F_i(v_z)$ can be approximately represented by a drifting Maxwellian with a temperature $T_i \simeq T_e$ and a drift velocity $\sim 2\ (KT_i/M)^{\frac{1}{2}}$.

Over the range of plasma densities used in the experiment, the axial density is uniform to within 1%. The most reliable method of checking this is by measuring the variation of wavelength of electron plasma waves excited in the column at a frequency close to $\omega_{pe}/2\pi$. At these frequencies, the wavelength is very sensitive to changes of the electron density (see Chapter IV). A radial profile of the ion saturation current to a cylindrical Langmuir probe, (diameter 0.1 mm, length 3 mm), indicates that the column diameter $\simeq 2.6$ cm, (Fig.3.2).

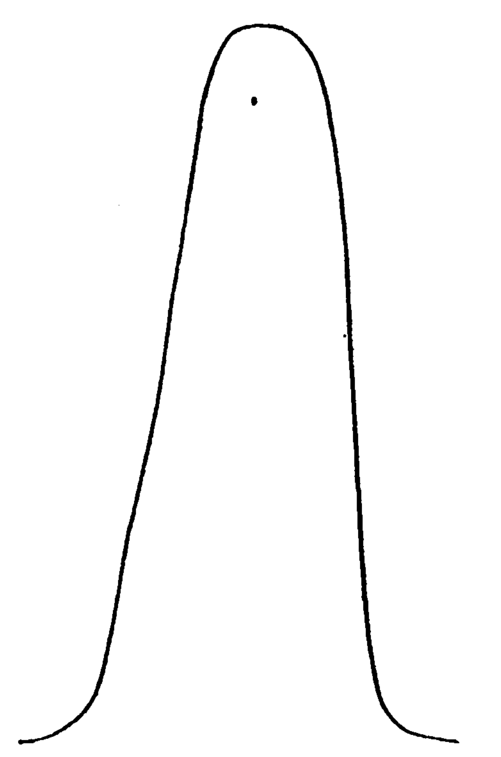

Fig.3.2
The radial profile of the ion saturation current to a Langmuir probe at a density 6×10^9 cm^{-3}; maximum current = 7.2 μA, horizontal scale: 1 cm div^{-1}

Under these operating conditions the plasma is almost quiescent. In practice it is impossible to completely suppress all electrostatic instabilities, particularly those associated with the radial variation of plasma potential, (Motley (op. cit.) pp.67-82). However the non-thermal level of fluctuations under these conditions is very small compared to that produced by the pulsed electron currents; the initial conditions are very close to thermal equilibrium. Table 3.1 gives a list of the relevant plasma parameters.

TABLE 3.1

INITIAL PLASMA CONDITIONS

number density	n	10^9-10^{10} cm^{-3}
electron plasma frequency	$\omega_{pe}/2\pi$	300-1000 MHz
ion plasma frequency	$\omega_{pi}/2\pi$	1.1-3.8 MHz
axial magnetic field	B_z	2-4 kG
electron cyclotron frequency	$\omega_{ce}/2\pi$	5.5-11 GHz
ion cyclotron frequency	$\omega_{ci}/2\pi$	75-150 kHz
electron and ion temperatures	$T = T_e \simeq T_i$	$\simeq 2500^\circ K \simeq 0.2$ eV
electron thermal velocity	v_{eo}	2×10^7 cm s^{-1}
Debye length	λ_D	100-30 μm
column length	ℓ	80 cm
column radius	a	1.3 cm
number of particles per Debye cube	N_D	$10^3 - 3.10^2$
electron-neutral collision mean free path	λ_{en}	$\sim 10^3$ cm *
ion-neutral collision mean free path	λ_{in}	$\sim 10^2$ cm *
background neutral gas density	n_n	$\sim 10^{10}$ cm^{-3} *

* These estimates are based on the assumption that the partial pressure of neutral potassium vapour in the plasma column is no greater than the total pressure measured at the vacuum chamber wall.

3.2 THE EXPERIMENT

An experiment to study the evolution of a plasma from the above initial conditions to a turbulent state resulting from the electron-ion two-stream instability, requires an electron drift, $v_d > 1.3\, v_{eo}$. The plasma equilibrium arising from a steady electron drift may bear little relation to the initial quiescent conditions since it will depend on plasma production and loss processes at the two ends.

These considerations suggest that, if the timescale characterising the growth of the two-stream instability is short compared with the time taken for electrons to travel the length of the column, it should be possible to study the evolution of the instability by inducing a pulsed electron drift. (In practice it was not found possible to induce steady electron drifts of the same magnitude as v_{eo}.) The relevant timescales for a pulsed experiment are shown in Table 3.2.

TABLE 3.2

TIMESCALES FOR A PULSED EXPERIMENT

pulse repetition period	$\tau_1 \geqslant 10^{-3}$ s	variable
electron containment time, $\frac{\ell}{v_d}$	$\tau_2 \sim 10^{-6}$	$\propto \frac{1}{v_d} < \frac{1}{1.3\, v_{eo}}$
pulse duration	$\tau_3 \sim 10^{-6}$	variable
growth timescale for two-stream instability, ω_{pi}^{-1}	$\tau_4 \sim 10^{-7}$	$\propto \frac{1}{n^{\frac{1}{2}}}$ (for $n \sim 10^9\ cm^{-3}$)

The requirement

$$\tau_1 \gg \tau_2 \geqslant \tau_3 \gg \tau_4 \qquad \ldots (3.1)$$

gives a lower limit to the plasma density suitable for the experiment. An upper limit is given by the requirement

$$N_D \gg 1 \qquad \ldots (1.1)$$

Also, if we accelerate the electrons with a uniform field E_o, applied at $t = 0$, then from equation (2.24) we require,

$$E_o > E_c = \frac{m v_{eo} \omega_{pi}}{e} \quad . \qquad \ldots (3.2)$$

Over the range of densities in Table 3.1, E_c varies from 7 to 20 V m^{-1}.

It is possible to draw pulsed currents from the plasma by using the circuit in Fig.3.3(a). Positive going voltage pulses with a risetime τ_R, of 20 ns are applied via a 1 µF decoupling capacitor to the cold plate, with a repetition rate determined by the time taken for the plasma column to return to equilibrium. (The optimum rate, which is found empirically, depends on the amplitude and duration of the voltage pulses but always lies in the range 100–1000 Hz.) The coaxial cable feed and the cylindrical waveguide provide a low inductance return path for the current from the hot plate to the pulse generator.

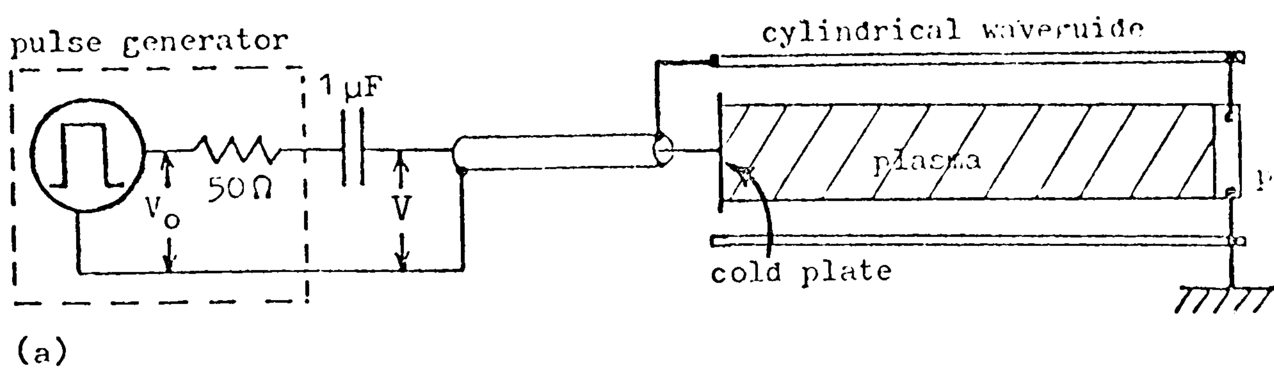

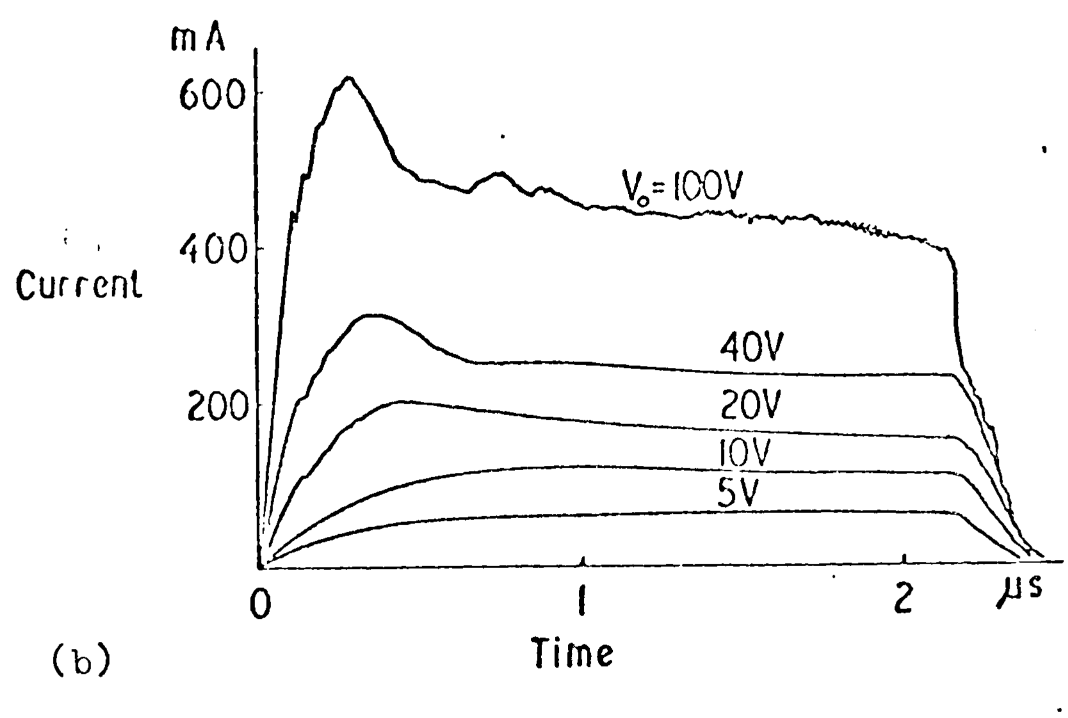

Fig.3.3
(a) Schematic arrangement of the experiment
(b) Current at the cold.plate

Figure 3.3(b) shows how a $2\,\mu s$ duration current pulse $I(t)$, varies with V_o, the open circuit pulse generator voltage. In general for low V_o, i.e. $\leqslant 5\,V$, the current pulse can remain steady for 20–30 μs, but for $V_o \sim 100\,V$ it rapidly decays after 3–4 μs. If $V_o \geqslant 20\,V$ then an initial current overshoot occurs and there is a large increase in the level of potential fluctuations detected by electrostatic probes immersed in the plasma (see Chapter V). The current is not effected by the magnetic field provided it exceeds 1 kG, below which the initial plasma density diminishes. Neither is the current effected by the hot plate temperature provided it exceeds a critical value ($\sim 2{,}500^oK$) ; presumably the hotplate must provide a sufficient electron flux to balance the loss of electrons at the cold plate.

These results pose two questions:

(a) Does the current at the cold plate represent a uniform electron drift in the plasma column? (We should not expect a uniform field E_0, in a collisionless plasma since the plasma would shield the cold plate potential in a time $\omega_{pe}^{-1} \ll \tau_R$.)

(b) Can we estimate $v_d(t)$ for the electrons by assuming

$$v_d(t) = \frac{I(t)}{\pi a^2 ne} \qquad \dots (3.3)$$

where n is constant and determined by the initial conditions?

To answer both questions completely we require knowledge of $n(z,t)$ and $v_d(z,t)$, which can be determined unambiguously from measurement of the dispersion of electron plasma waves and is dealt with in Chapter IV. It would seem from these results that after the overshoot, when the current is constant (i.e. $t \sim 1\,\mu s$), relation (3.3) is a good approximation for the electron drift all along the column. In section 3.4 we give a theory which explains how a uniform electron drift might be set up in a collisionless plasma column by applying a positive potential to the cold plate.

3.3 ELECTRICAL MEASUREMENTS

A log-log plot of plasma current I, versus potential difference between the end plates V, at $t = 1\,\mu s$ for a density of $6 \times 10^9\ cm^{-3}$ * is shown in Fig.3.4.

Below a critical value I_c, the current appears to be space-charge limited (i.e. $I = KV^{\frac{3}{2}}$), whereas above I_c correspondingly larger voltages are required to drive the current. The onset of fluctuations and the current overshoot also occur when $I > I_c$. In Fig.3.5 we see that if relation (3.3) holds, then I_c corresponds to the critical drift velocity for the onset of the two-stream instability, equation (2.16).

These results suggest a simple model for the plasma column. The potential applied to the cold plate is dropped across a space-charge limited sheath in series with the plasma column. For $I < I_c$ the plasma is quiescent and has a negligible resistance, but for $I > I_c$ the plasma becomes unstable to the two-stream instability which leads to a turbulent plasma with an appreciable resistance. The field E_0, in the turbulent plasma can be estimated by subtracting the extrapolated sheath potential drop V_s, from the potential V, at the cold plate, viz:

$$E_0 = \frac{V_{pl}}{\ell} = \frac{V - V_s}{\ell} \simeq \frac{V - (I/K)^{\frac{2}{3}}}{\ell} \quad . \qquad \ldots (3.4)$$

The estimate of the column conductance $1/R$, at $t = 1\,\mu s$ for various densities, is shown as a function of current in Fig.3.6, along with the corresponding values of V_{pl}. For correspondingly large currents, $1/R$ appears to become independent of I, although the trend is not so clear at lower densities.

In Fig.3.7 we compare the limiting values of $1/R$ with the 'classical' value, computed from equation (1.10), and the value predicted

* The density of the quiescent plasma, (i.e. without the current pulse), was deduced from an estimate of the electron plasma frequency by measuring the dispersion of electron plasma waves, (see Chapter IV).

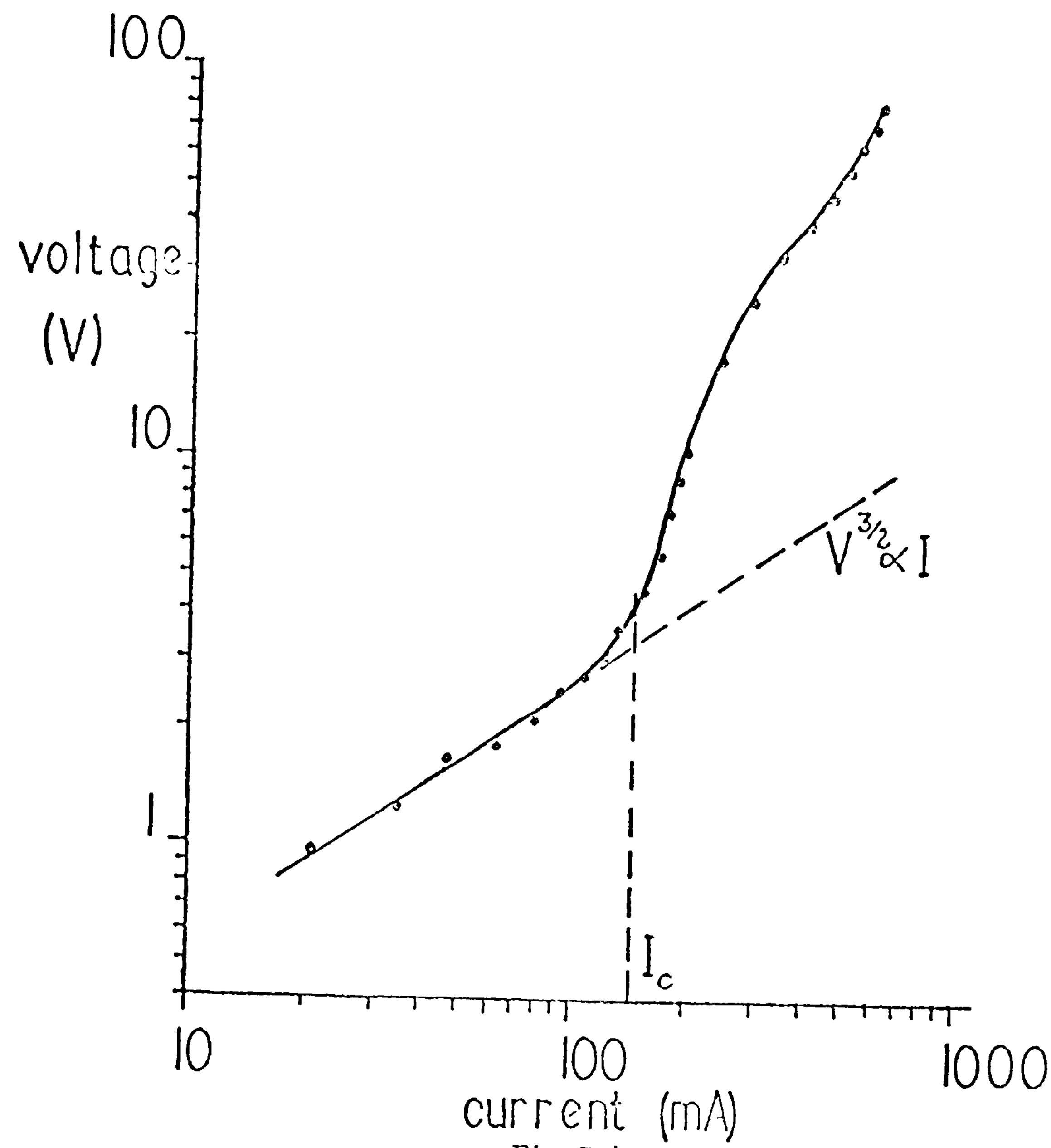

Fig.3.4
Pulsed current-voltage relationship at 1 μs for $n = 6 \times 10^9$ cm^{-3}

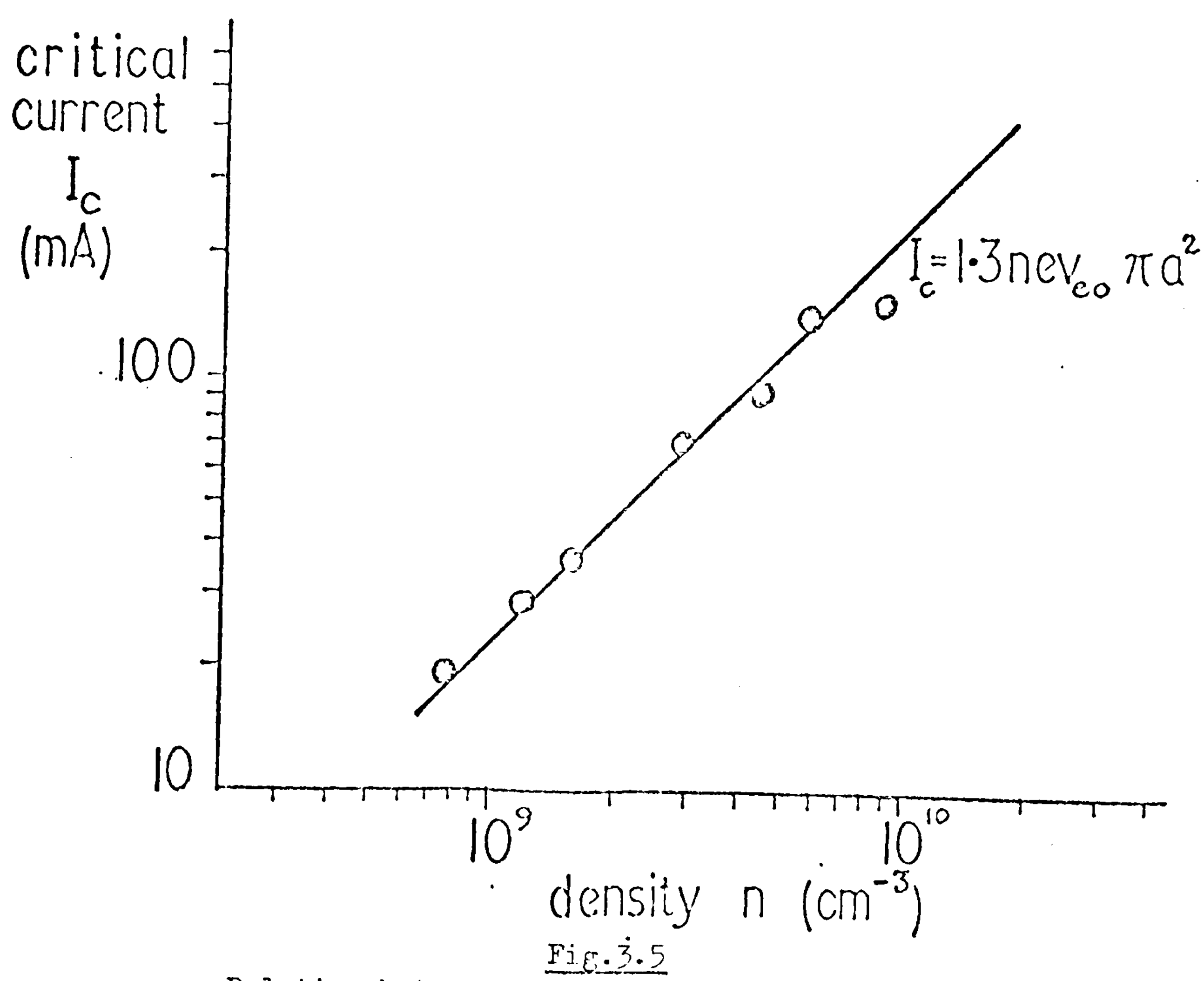

Fig.3.5
Relation between critical current and density

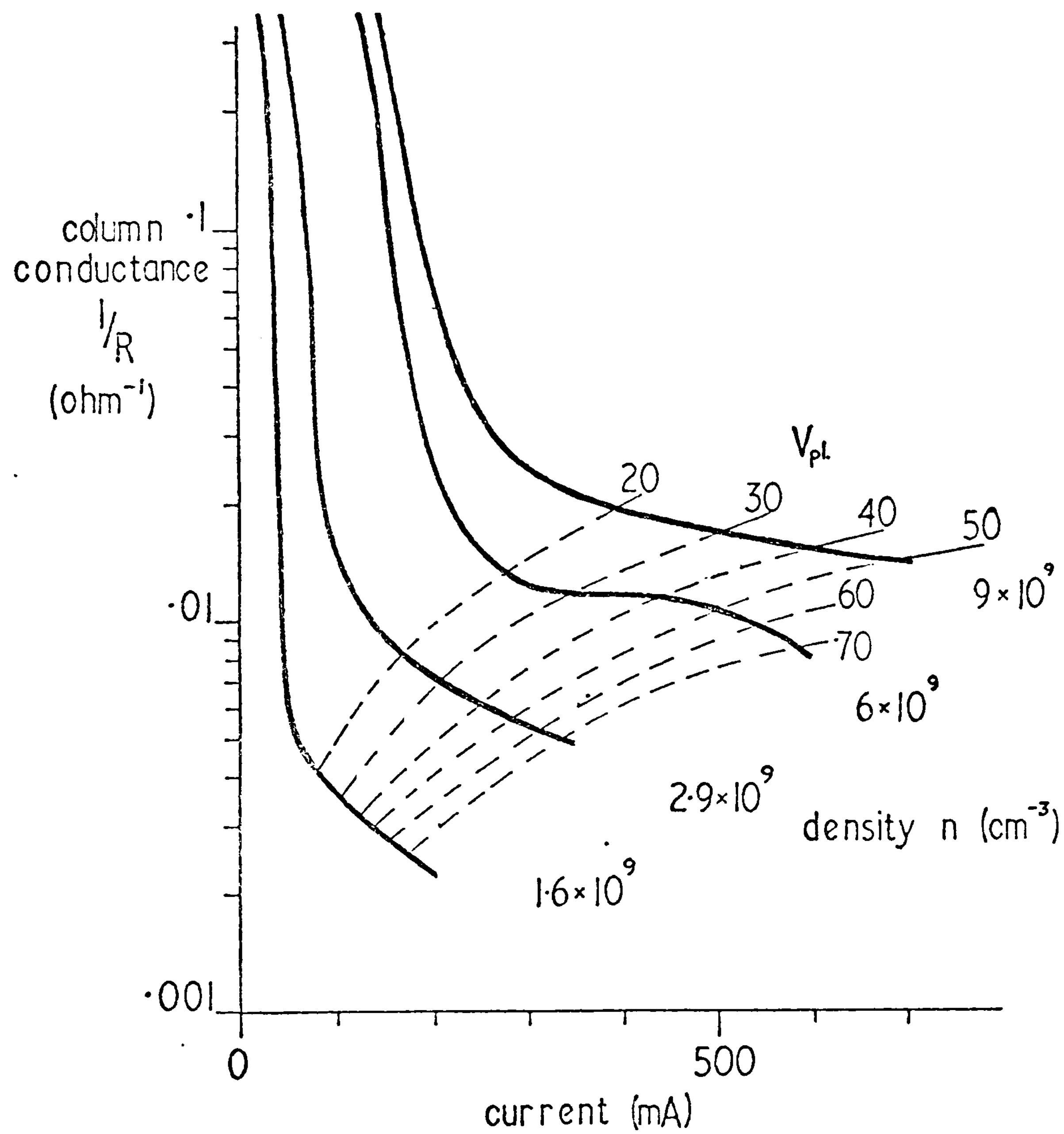

Fig.3.6
Variation of column conductance at 1 μs with density and current

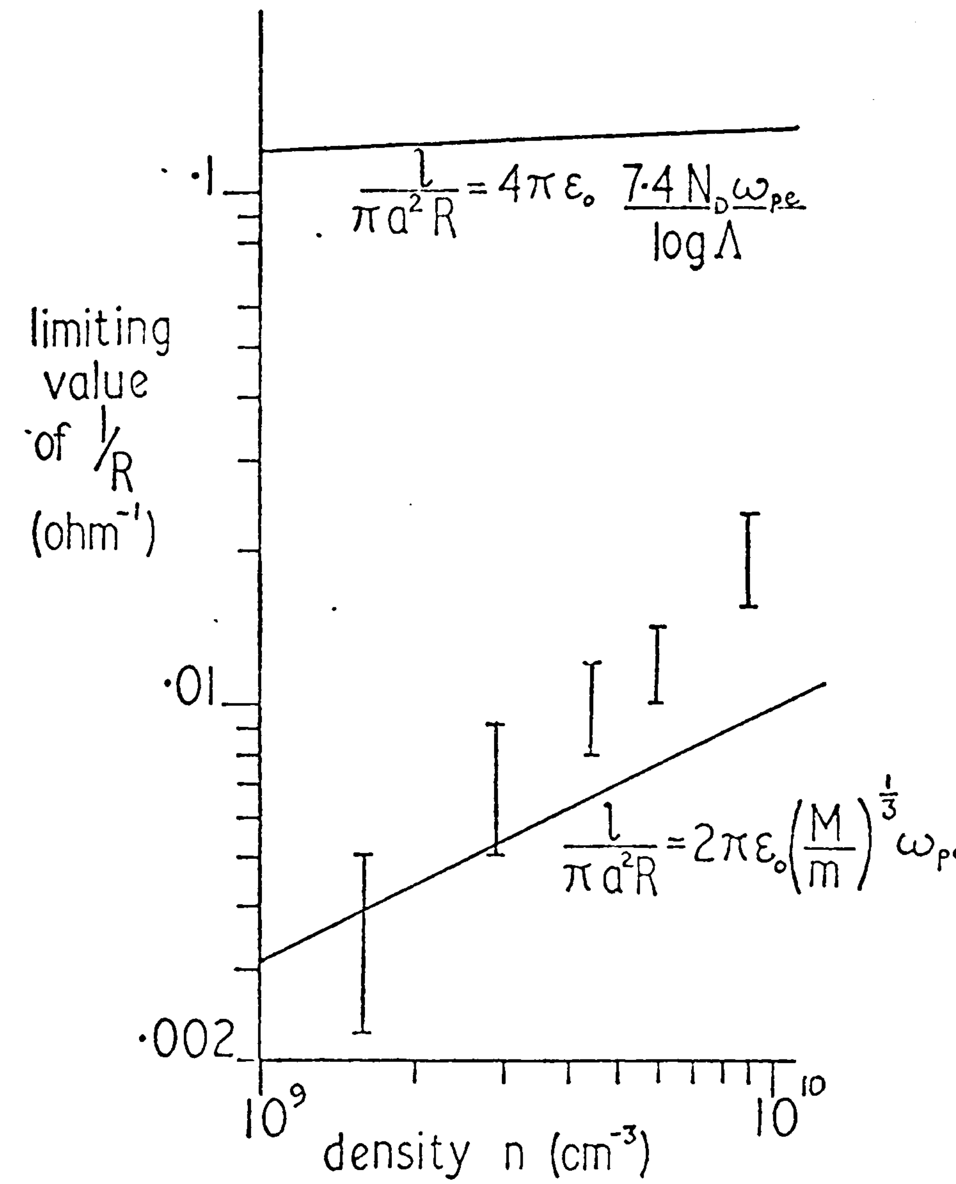

Fig.3.7
The variation of the limiting value of the column conductance with density compared with the variation predicted by classical conductivity (1.10) and the variation predicted by the empirical scaling law (1.12) of Hamberger & Friedman

by the scaling (1.12) measured by Hamberger and Friedman (see section 1.2). Further comment on these results will be made in the next chapter.

Finally, Fig.3.8 shows how the perveance K, of the sheath (measured for $I < I_c$), varies with density; (again at low densities the $V^{\frac{3}{2}}$ law is not so clearly evident as in Fig.4.5). The relation $K \propto n$ shows that if K is determined by

$$K = \frac{4\varepsilon_o}{9}\left(\frac{2e}{m}\right)^{\frac{1}{2}} \frac{\pi a^2}{d^2} \qquad \ldots (3.5)$$

which is the Langmuir-Child formula for a space-charge limited diode with cold electrons,(see e.g. VON ENGEL (1955), p.13), then the sheath dimension d, is

$$d \simeq 5\lambda_D \qquad \ldots (3.6)$$

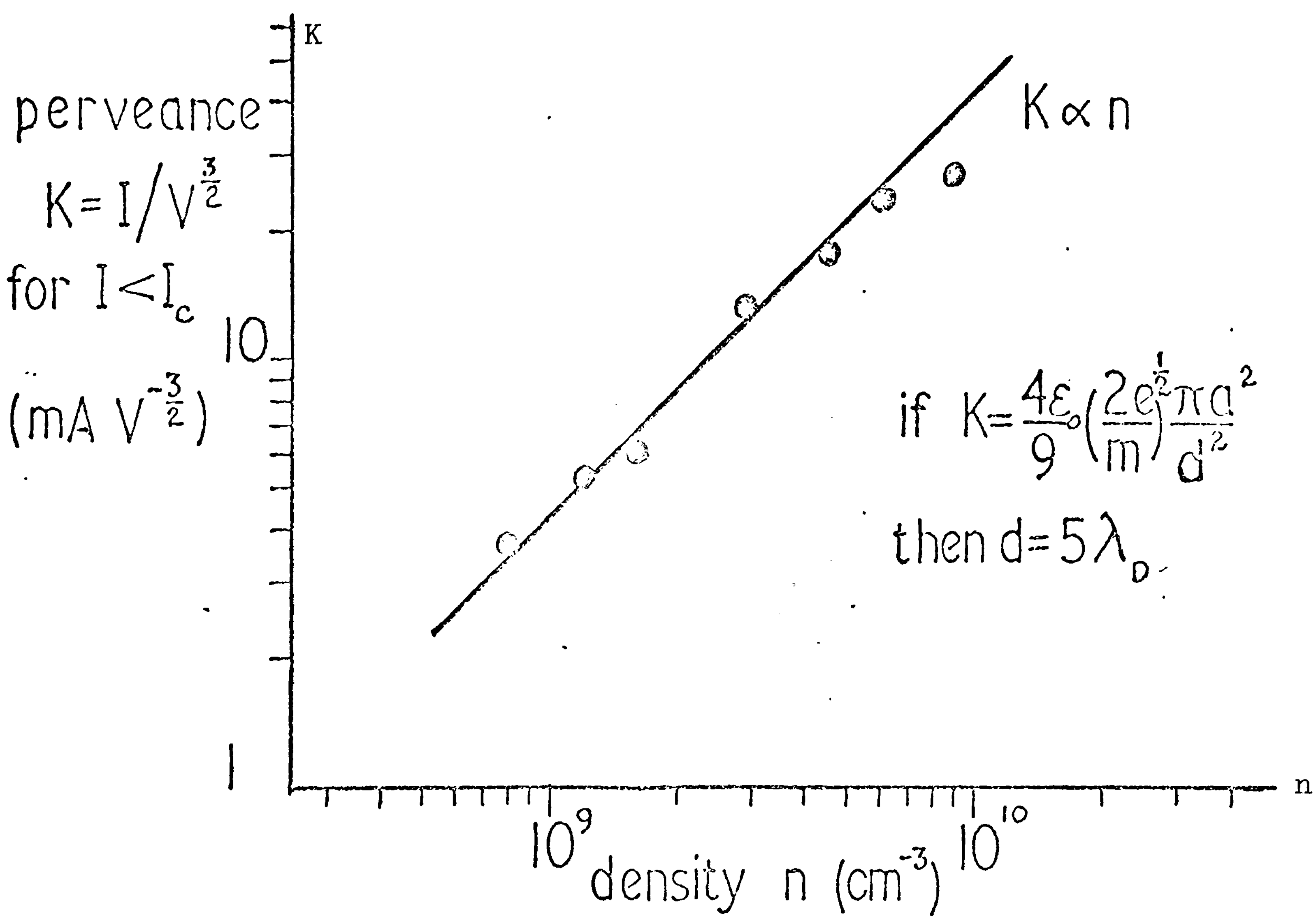

Fig.3.8

Relation between sheath perveance and density

3.4 A THEORY DESCRIBING THE ESTABLISHMENT OF AN ELECTRON DRIFT IN A COLLISIONLESS PLASMA COLUMN

In this section we give a cold fluid theory which describes the column response to a positive voltage pulse applied to the cold plate of a collisionless plasma, i.e. this theory is applicable only for $I < I_c$.

3.4.1 The Transmission Line Equations for a Cold Electron Plasma Column

The potential of the cold plate is raised by applying a voltage pulse with a risetime τ_R, such that

$$\omega_{pi}^{-1} \gg \tau_R \gg \omega_{pe}^{-1} . \qquad \ldots (3.7)$$

This does not produce a uniform axial electric field in the plasma column because the potential varies slowly in terms of the electron timescale ω_{pe}^{-1}, so that the electrons can easily move to screen the cold plate from the plasma by establishing an electron sheath. (We shall ignore the ion dynamics in this problem, although a positive potential on the cold plate upsets the ion equilibrium on a timescale M/m times larger than the transit time for electrons in the column.)

The boundary conditions at the cold plate are substantially altered in that electrons approaching the plate will be absorbed instead of reflected. This produces an electron density rarefaction which moves away from the cold plate down the column towards the hot plate. The propagation of this electron density perturbation can be described in terms of the dispersion of low frequency $(\omega \sim \tau_R^{-1} \ll \omega_{pe})$, electron plasma waves in the column.

As in section 2.3, we consider the model of a cold, collisionless plasma, completely filling a cylindrical waveguide in a strong magnetic field, $(\omega_{ce} \gg \omega_{pe})$. (The dispersion in a partially-filled waveguide is discussed in Appendix A.3.)

Provided $\omega/k \ll c$, the dispersion of electron plasma waves for $\omega^2 \gg \omega_{pi}^2$ is given by, (see equation (A2.2) in Appendix A.2),

$$\frac{\omega^2}{\omega_{pe}^2} = \frac{k_z^2 a^2}{k_z^2 a^2 + p_{\mu\nu}^2} . \qquad \ldots (3.8)$$

A perturbation of arbitrary radial and azimuthal variation can be described by a superposition of eigenmodes, but a plane cold plate will principally excite the lowest order (0,0) mode. The low frequency ($\omega^2 \ll \omega_{pe}^2$), long wavelength ($k_z^2 a^2 \ll (2.4)^2$), electron plasma waves will be non-dispersive in that $\omega/k \simeq$ constant, i.e. potential perturbations of the form

$$\varphi(r,z,t) = \tilde{\varphi} J_0 \left(\frac{2.4r}{a}\right) e^{i(k_z z - \omega t)} \qquad \ldots (3.9)$$

(with similar expressions for density and velocity), have a dispersion relation :

$$\frac{\omega}{\omega_{pe}} \simeq \frac{k_z a}{2.4} \qquad \ldots (3.10)$$

Equation (3.10) can be derived from the linearised 1-D electron continuity and momentum equations with a long wavelength approximation for Poisson's equation, viz:

$$\left.\begin{aligned} \frac{\partial \tilde{n}}{\partial t} &= - n_0 \frac{\partial \tilde{v}}{\partial z} \\ \frac{\partial \tilde{v}}{\partial t} &= \frac{e}{m} \frac{\partial \tilde{\varphi}}{\partial z} \\ \frac{\partial^2 \tilde{\varphi}}{\partial r^2} + \frac{1}{r}\frac{\partial \tilde{\varphi}}{\partial r} + \frac{\partial^2 \tilde{\varphi}}{\partial z^2} &\simeq - \left(\frac{2.4}{a}\right)^2 \tilde{\varphi} = \frac{\tilde{n} e}{\epsilon_0} \end{aligned}\right\} \qquad \ldots (3.11)$$

The a.c. conduction current carried by these waves is

$$\left.\begin{aligned} I(z,t) &= \tilde{I}\, e^{i(k_z z - \omega t)} \\ \text{where} \quad \tilde{I} &= - \int_0^a n_0\, e\, v(r)\; 2\pi r\, dr \\ &= n_0\, e\, \tilde{v} A \end{aligned}\right\} \qquad \ldots (3.12)$$

where

$$A = 2\pi a^2 \int_0^1 x J_0(2.4x)\, dx$$

$$= 2\pi a^2 \frac{J_1(2.4)}{2.4} \simeq 0.43\, \pi a^2 \qquad \ldots (3.13)$$

(see e.g. GRADSHTEYN and RYZHIK (1965) p.683). Now we can re-write equations (3.11)

$$\left.\begin{aligned} \frac{\partial I}{\partial t} &= -\frac{1}{\bar{L}} \frac{\partial \varphi}{\partial z} \\ \frac{\partial \varphi}{\partial t} &= -\frac{1}{\bar{C}} \frac{\partial I}{\partial z} \end{aligned}\right\} \qquad \ldots (3.14)$$

These are the equations for a loss-less transmission line where :

$$\left.\begin{aligned} &\text{inductance per unit length,} \quad & \bar{L} &= \frac{m}{n_o e^2 A} \\ &\text{capacitance per unit length,} \quad & \bar{C} &= \frac{\epsilon_o A\,(2.4)^2}{a^2} \end{aligned}\right\} \qquad \ldots (3.15)$$

Hence the velocity of propagation

$$u = \frac{1}{\sqrt{\bar{L}\,\bar{C}}} = \frac{\omega_{pe} a}{2.4} \qquad \ldots (3.16)$$

and the characteristic impedance

$$Z_o = \sqrt{\frac{\bar{L}}{\bar{C}}} = \frac{a}{2.4 A e} \sqrt{\frac{m}{n_o \epsilon_o}} \; . \qquad \ldots (3.17)$$

For a plasma column radius 1.2 cm and density 10^9 cm^{-3};

$$\left.\begin{aligned} u &= 9.4 \times 10^3 \text{ cm s}^{-1} \\ Z_o &= 1.4 \text{K}\,\Omega \end{aligned}\right\} \qquad \ldots (3.18)$$

The linearised equations (3.11) and (3.14) are a good approximation provided

$$\left.\begin{aligned} \tilde{\varphi} &\ll \frac{mu^2}{e} \\ \tilde{I} &\ll \frac{mu^2}{e} \cdot \frac{1}{Z_o} \end{aligned}\right\} \qquad \ldots (3.19)$$

(see equation (A1.3) appendix A.1).

Using the values (3.18) we have

$$\tilde{\varphi} \ll 600\,\text{V}$$
$$\tilde{I} \ll 1 \text{ amp} \qquad \ldots (3.20)$$

These conditions are well satisfied, so that the equivalent circuit for the plasma column when $I < I_c$,(i.e. when the column is not resistive), is represented, to a good approximation, by a loss-less transmission line.

3.4.2 The Equivalent Circuit

The equivalent circuit for the experiment is shown in Fig.3.9.

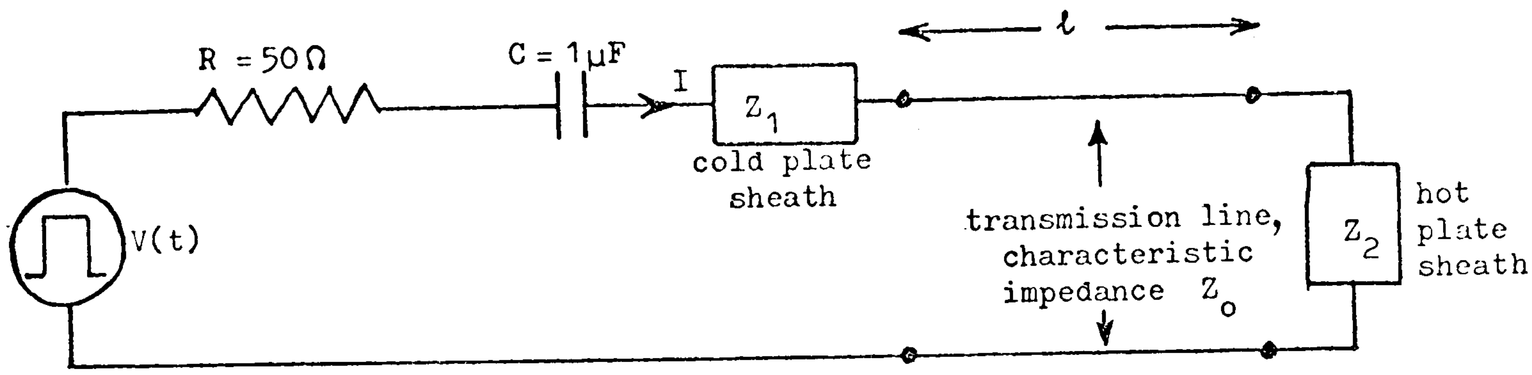

Fig.3.9
Equivalent circuit for the experiment

To estimate the nonlinear impedances Z_1 and Z_2 we use simple but appropriate sheath models. For the cold plate we assume a space-charge limited, electron-rich sheath, i.e. $V^{\frac{3}{2}} = I/K$. Then

$$Z_1(I) = \frac{1}{K^{\frac{2}{3}} I^{\frac{1}{3}}} \; . \qquad \ldots (3.21)$$

The value of $Z_1(I)$ can be estimated from the conditions; we choose in particular, $n = 5 \times 10^9 \text{ cm}^{-1}$, $I = 20\,\text{mA}$ (see Fig.3.12). Thus from Fig. 3.8, $K \simeq 12 \times 10^{-3}\,\text{A}\,\text{V}^{-\frac{3}{2}}$, then

$$Z_1 \simeq 70\,\Omega$$

At the hot-plate we have a large reservoir of electrons in the electron-rich sheath. If we assume

$$I = -\,I_R\, e^{-eV_s/KT}$$

where I_R is the electron current due to thermionic emission and V_s is the potential difference between the hot-plate and the plasma, then the incremental impedance

$$Z_2 = \frac{dV}{dI} = \frac{KT}{e} \cdot \frac{1}{I_R} \qquad \ldots (3.22)$$

In the experiment $I_R \sim 6\,A$ and $KT/e \sim 0.2V$ thus $Z_2 \sim 10^{-2}\ \Omega$.

To a good approximation we can consider Z_1 as constant and ignore Z_2 and C in Fig.3.9 so that our circuit is just the pulse generator loaded with a short-circuited transmission line of length ℓ, i.e.

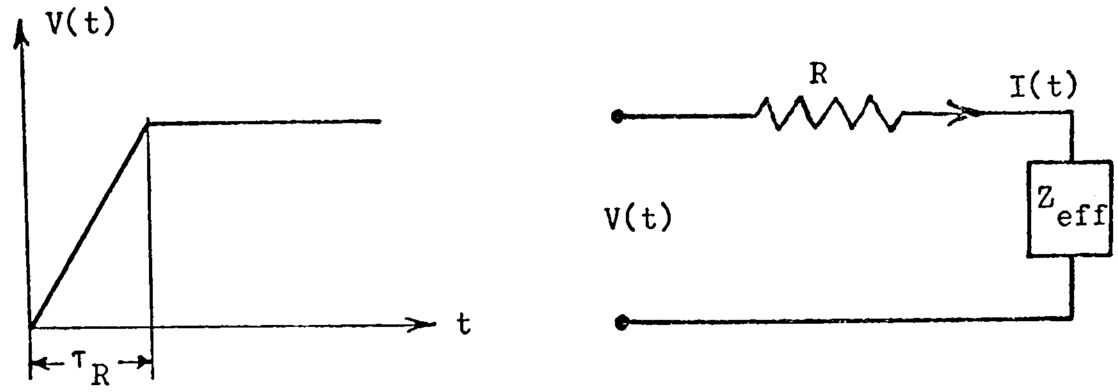

where

$$V(t) = V_o\, G(t) = \frac{V_o}{\tau_R}\left[tH(t) - (t-\tau_R)\, H(t-\tau_R)\right]$$

and

$$Z_{eff} = i\, Z_o \tan \frac{\omega\ell}{u}$$

(see e.g. BLEANEY and BLEANEY (1965), p.309).

The standard method of determining $I(t)$ is by use of Laplace transforms, viz:

$$I(t) = \int_{-i\infty}^{+i\infty} \tilde{I}(s)\, e^{st}\, ds \qquad \ldots (3.23)$$

where

$$\tilde{I}(s) = \frac{\tilde{V}(s)}{R + Z_o \tanh (s\ell/u)} \qquad \ldots (3.24)$$

and

$$\tilde{V}(s) = \frac{V_o}{\tau_R s^2}\left[1 - e^{-s\tau_R}\right] \qquad \ldots (3.25)$$

Manipulating equation (3.24),

$$\tilde{I}(s) = \frac{\tilde{V}(s)}{R + Z_o}\ \frac{1 + e^{-s/s_o}}{1 - \rho\, e^{-s/s_o}}$$

$$= \frac{\tilde{V}(s)}{(R + Z_o)}\left\{1 + \frac{(\rho+1)}{\rho}\sum_{n=1}^{\infty} \rho^n\, e^{-ns/s_o}\right\} \qquad \ldots (3.26)$$

where the reflection coefficient,

$$\rho = \frac{Z_o - R}{Z_o + R} \qquad \ldots (3.27a)$$

and the time for a pulse to travel up the column and back,

$$\frac{1}{s_o} = \frac{2\ell}{u} \; . \qquad \ldots (3.27b)$$

In the experiment $\tau_R < \frac{2\ell}{u}$. Substitution of equations (3.26) and (3.25) into (3.23) will determine $I(t)$, however it can be seen by inspection that the solution takes the form (3.28) shown in Fig.3.10 :

$$I(t) = \frac{V_o}{(R + Z_o)} \left[G(t) + \left(\frac{1+\rho}{\rho}\right) \sum_{n=1}^{\infty} \rho^n \, G\left(t - \frac{2n\ell}{u}\right) \right] \qquad \ldots (3.28)$$

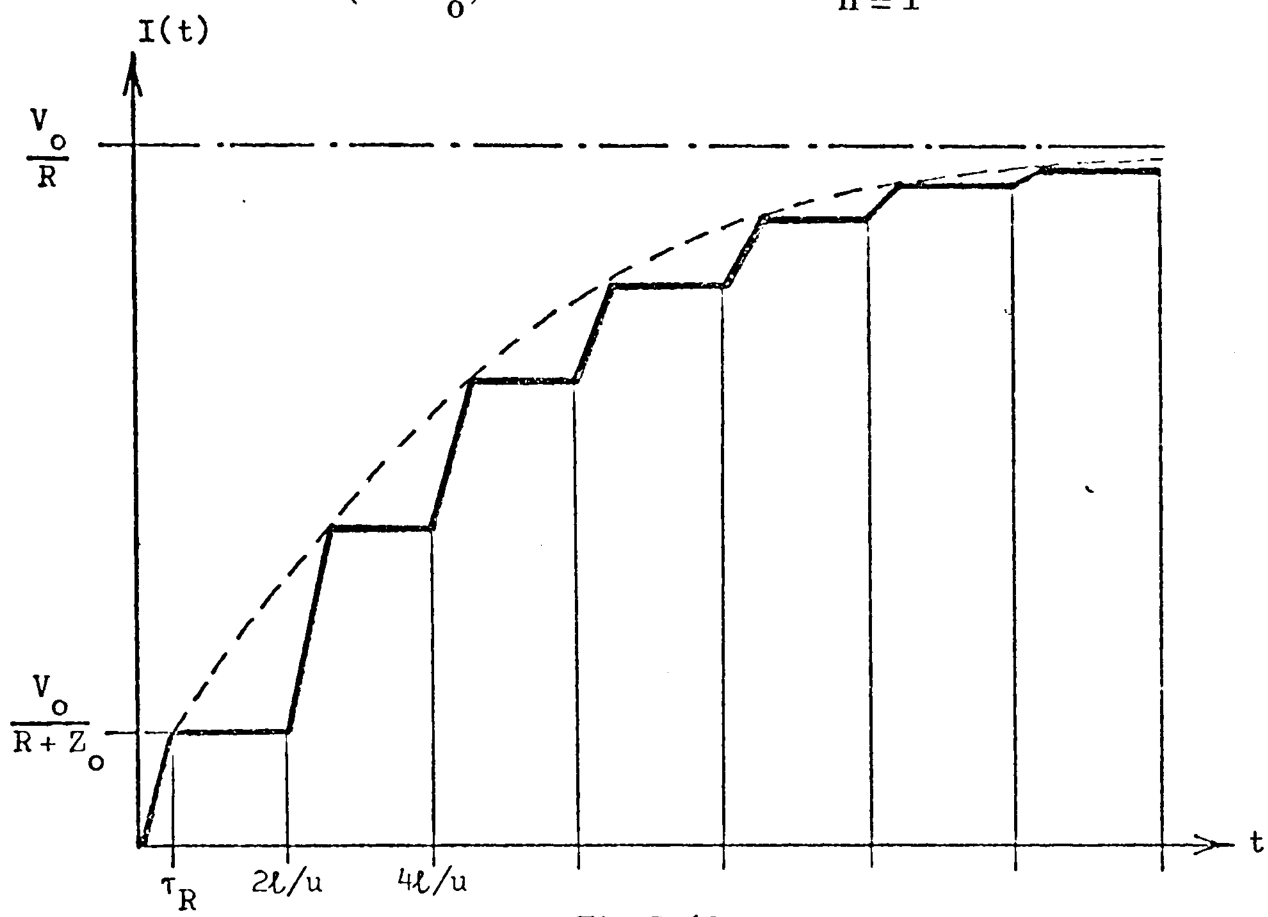

Fig.3.10
Electron current at the cold plate

The envelope of $I(t)$ (dashed line in Fig.3.10), is described by the function

$$I(p) = \frac{V_o}{R+Z_o} \left[1 + \left(\frac{1+\rho}{1-\rho}\right)(1 - \rho^p) \right]$$

$$= \frac{V_o}{R} - \frac{V_o}{R+Z_o} \cdot \frac{Z_o}{R} \, \rho^p \qquad \ldots (3.29)$$

where $p = \frac{u}{2\ell}(t - \tau_R)$. Thus

$$\frac{dI}{dp} = \frac{V_o}{R+Z_o} \cdot \frac{Z_o}{R} \cdot \frac{\rho^p}{\log_e(1/p)} \; . \qquad \ldots (3.30)$$

The function (3.29) obeys the differential equation,

$$L \frac{dI}{dt} + R\,I = V_o \; , \qquad \ldots (3.30)$$

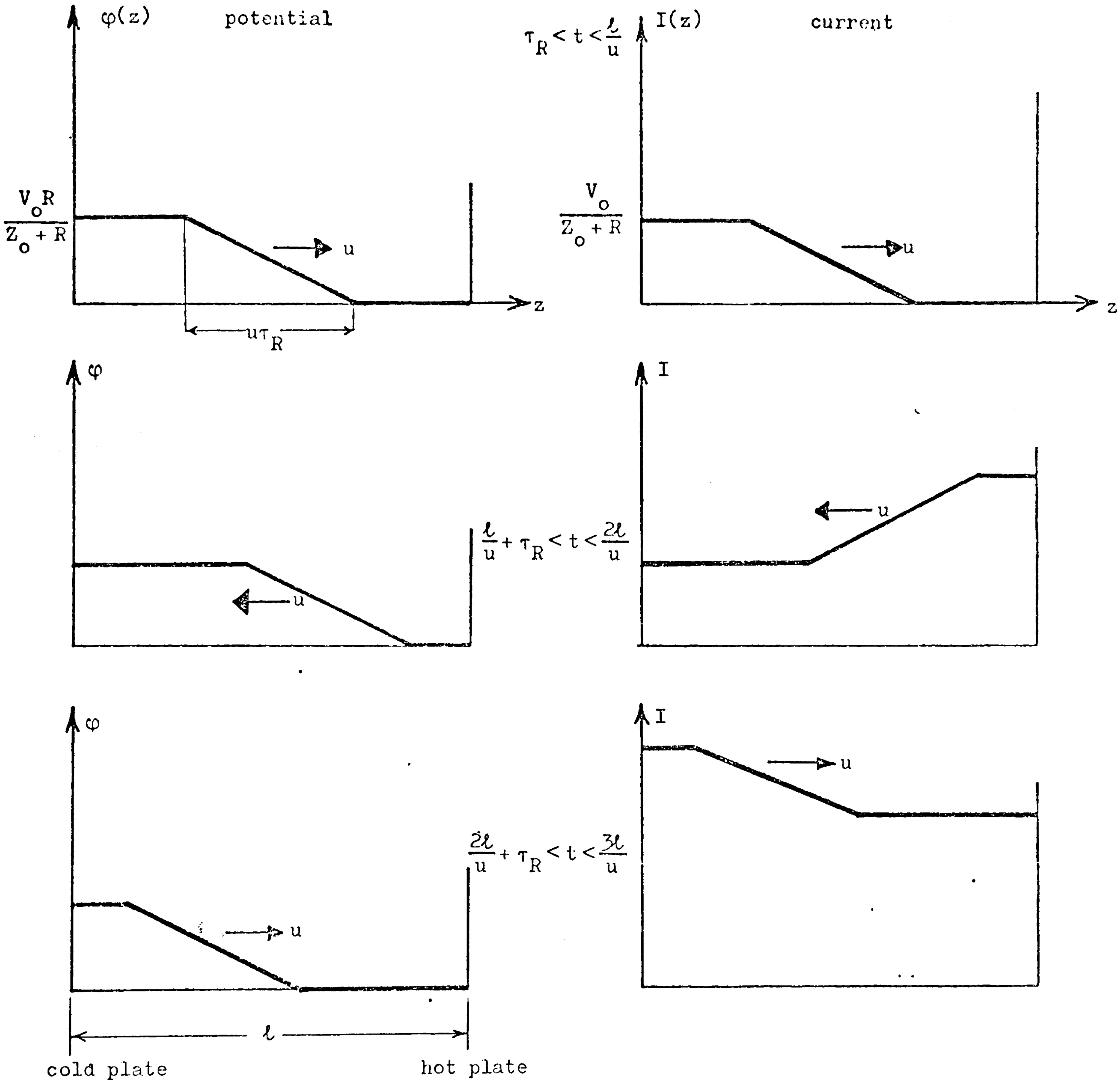

Fig.3.11

The potential and the electron current in the plasma column at three sequential instances showing how the electron current is established where

$$L = \frac{2\ell}{u} \cdot \frac{R}{\log_e(1/\rho)} \quad .$$

If $Z_o \gg R$ then

$$L \simeq \frac{\ell Z_o}{u} = \frac{\ell m}{n_o e^2 A} \quad . \qquad \dots (3.30)$$

The effective inductance L, is just the inertial inductance of the plasma column, i.e. equation (1.8).

Physically, a potential ramp travels up and down the column at a velocity u, being totally reflected at the hot plate and partially reflected (with a coefficient of reflection ρ), at the cold plate. In this way the electron drift in the column is built up in steps as shown in Fig.3.11. For timescales $\gg 2\ell/u$, the electrons in the column are uniformly accelerated so that the maximum current is limited by R and the risetime of the current by the electron inertial inductance L, of the column.

3.4.3 Comparison with Experiment

The stepped nature of the rising current at the cold plate is clearly seen in Fig.3.12 which shows a typical current trace for $I < I_c$. Also shown is the signal received from an electrostatic probe situated midway along the column. The interpretation of this is complicated by the plasma-probe coupling which tends to differentiate plasma potential fluctuations (see Chapter V), but measurements of the spatial variation of this signal indicate that it represents a disturbance propagating up and down the column.

The parameters u, Z_o and L estimated from Fig.3.12 are compared with the theoretical predictions in Table 3.3. The discrepancy is probably due to the fact that equations (3.9) and (3.10) are not good approximations for the long wavelength dispersion in a partially-filled waveguide where $b \simeq 2a$.

TABLE 3.3

Experiment (see Fig.3.12)	Theory (for a completely-filled waveguide) $n = 5 \times 10^9$ cm^{-3}
$u = 5.6 \times 10^9$ cm s^{-1}	$u = 2 \times 10^9$ cm s^{-1} from (3.16)
$Z_o = 400\ \Omega$	$Z_o = 700\ \Omega$ from (3.17)
$L = 10\ \mu$H (inductance of the external circuit $\simeq 0.5\ \mu$H)	$L = 26\ \mu$H from (3.30)

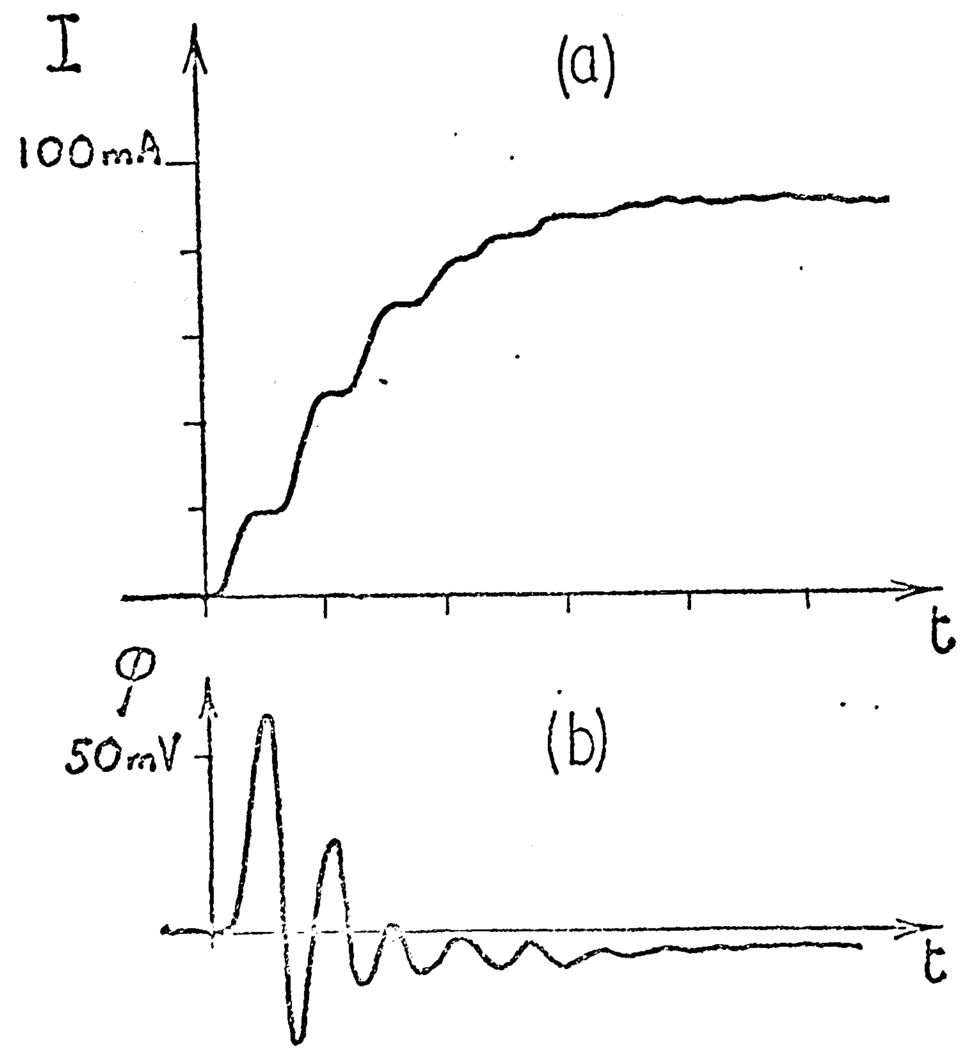

Fig.3.12

(a) The current at the cold plate for $I < I_c$, $n_o = 5 \times 10^9$ cm^{-3}, $V_o = 10$ V ;

(b) The signal received (into $50\,\Omega$ load) from an electrostatic probe midway along the column; time axis: 50 ns div^{-1}

The experimental value of u suggests that the eigenfunctions (3.9), for long wavelengths are better approximated by, (see Appendix A.3),

$$\varphi = \tilde{\varphi} J_0 \left(2.4 \frac{r}{c}\right) e^{i(k_z z - \omega t)} \qquad \ldots (3.31)$$

where

$$c \simeq 2.8\, a$$

Applying this correction to equation (3.12) for A and using the experimental value of u produces better agreement for L , but hardly effects Z_0 , viz :

$$Z_0 = 720\,\Omega \quad , \quad L = 12\,\mu H \ .$$

A better theory would include the correct long wavelength dispersion for a partially-filled waveguide and the effects of the nonlinear sheath impedance Z_1, but the physics would be substantially the same as the simple theory presented here. The physics for the establishment of an electron drift when the plasma is resistive is somewhat different and will be discussed in Chapter IV.

CHAPTER IV

A PLASMA DIAGNOSTIC: DISPERSION OF ELECTRON PLASMA WAVES

4.1 INTRODUCTION

An understanding of the physics of the experiment requires knowledge of $F_{i,e}(\underline{v},\underline{r},t)$. In this chapter we show that time-resolved measurements of the dispersion of electron plasma waves can give useful information about the space-averaged value of $F_e(v_z,t)$ and in particular provide a good measure of the moments n, v_d and v_e.

Measurements of the dispersion of small amplitude electron plasma waves in a Q-machine plasma column have been reported in the literature, (BARRETT et al. (1968) and FRANKLIN et al.(1974)). $F_e(v_z)$ was known in these experiments with some accuracy, so that the good agreement found between the predictions of linear theory and experiment suggests that measurement of the dispersion when $F_e(v_z)$ is unknown may be a method for gaining information about the electrons.

Figure 4.1(a) shows that the dispersion of lightly damped waves has three distinct regions when $a \gg \lambda_D$ and $\omega_{ce} \gg \omega_{pe}$, while Fig.4.1(b) shows the effect of electron drift, (cf Fig.2.6).

4.2 TIME-RESOLVED MEASUREMENT OF THE DISPERSION

The previous measurements of the dispersion were carried out under steady conditions, by launching a wave from a transmitter probe connected to an r.f. oscillator and measuring its phase variation along the column with a receiver probe connected to an r.f. interferometer, so that wavelength could be measured as a function of frequency, (see e.g. FRANKLIN et al (op.cit.)). However in a pulsed experiment the wavelengths will in general change during the pulse making this technique unsuitable. This problem is overcome by means of an electronic sampling circuit which is described in the next section. This technique effectively takes

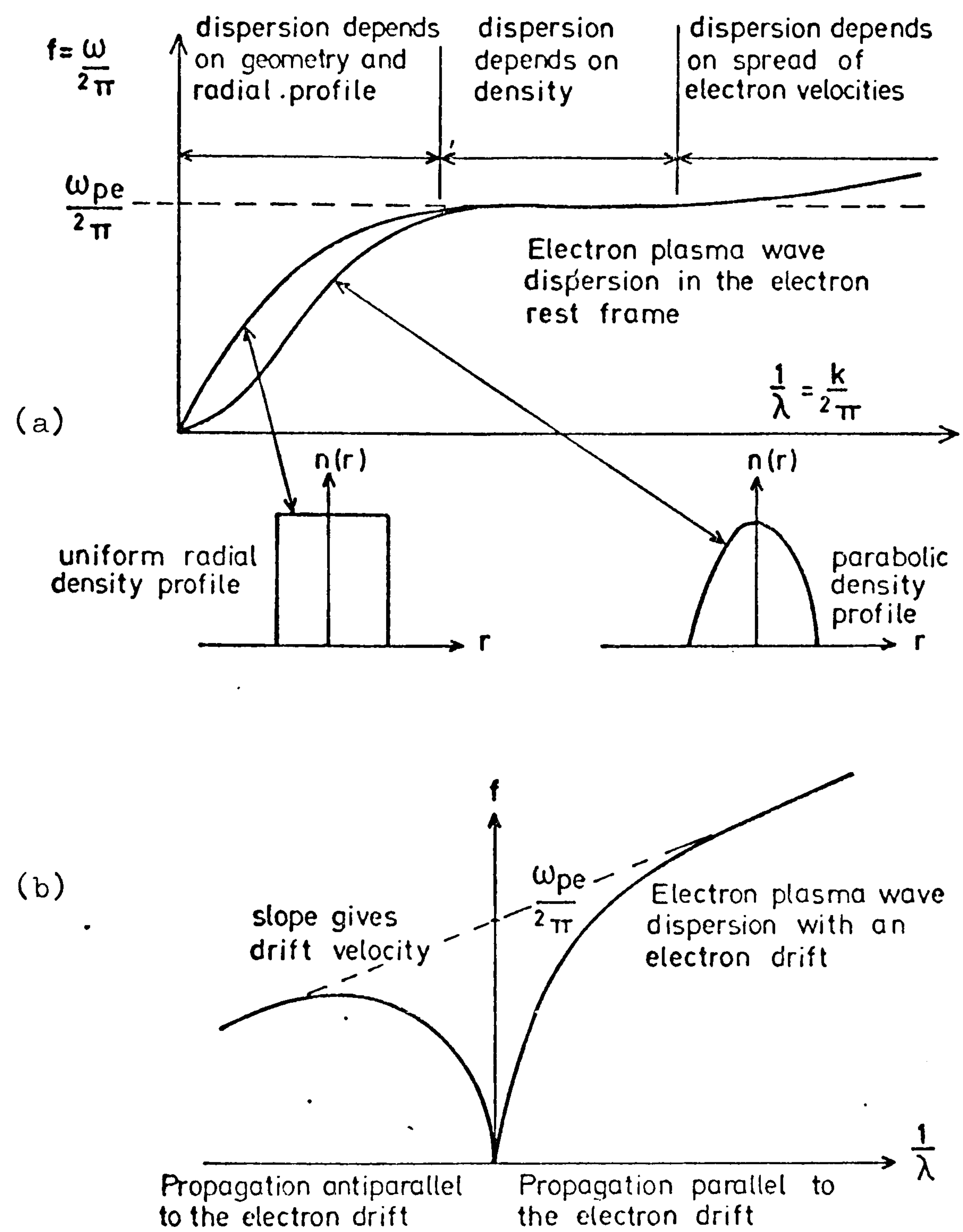

Fig.4.1
Dependence of the electron plasma wave dispersion on the various plasma parameters

'snapshots' of the instantaneous wavelength at a given frequency by recording the spatial variation of the instantaneous phase of the wave from an ensemble average taken over many pulses.

Interpretation of such measurements is possible if the parameters determining the dispersion relation are changing on a timescale much longer than the oscillation period of the waves, and a lengthscale much shorter than their wavelengths.

In Table 4.1 we show that these conditions exist in the experiment for lightly damped electron plasma waves.

TABLE 4.1

Growth timescale for two-stream instability ω_{pi}^{-1}	$\tau_4 \sim 10^{-7}$ s $\propto \frac{1}{n^{\frac{1}{2}}}$
Electron plasma wave period	$\tau_5 \sim 10^{-9}$ s $\propto \frac{1}{n^{\frac{1}{2}}}$
Electronic sampling gate width	$\tau_6 \simeq 3\times10^{-10}$ s fixed
Lengthscale for two-stream instability	$\omega_{pe}/v_d \sim 10^{-2}$ cm
Wavelength of lightly damped electron plasma waves, (determined emipirically)	$2\pi/k_z \leq 0.5$ cm

4.3 ELECTRONIC SAMPLING TECHNIQUE

Figure 4.2 shows the arrangement and design of the r.f. probes. The loop part preferentially couples to the lowest order (0,0) mode but does not couple effectively to high frequency ($\omega \geqslant \omega_{pe}$), short wavelength ($ka \gg 1$) waves for which the cross-wire is effective. As well as providing a low inductance coaxial return path for the current pulse, the cylindrical waveguide (diameter 5.1 cm) , has a cut-off frequency $\sim$5 GHz, so that electromagnetic resonances in the column and direct electromagnetic coupling between the probes are diminished for frequencies below $\sim$1 GHz. All these features help to give clean, sinusoidal interferometer traces.

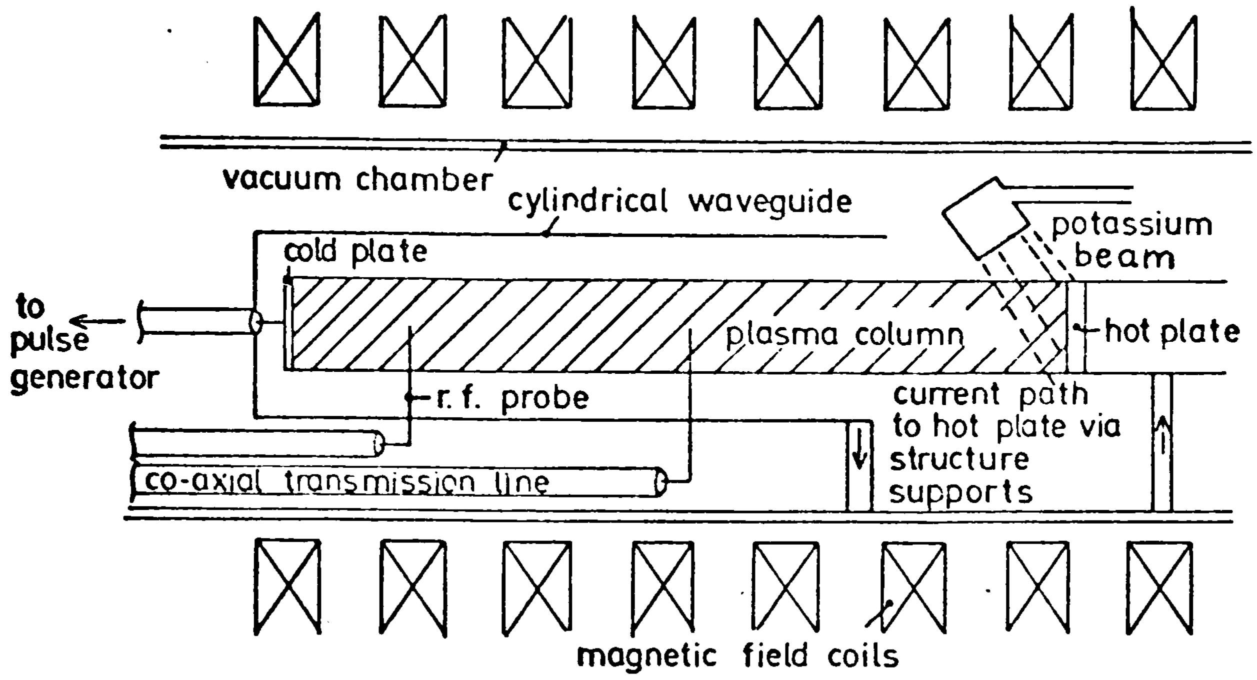

Fig.4.2(a)
Schematic arrangement of the experiment

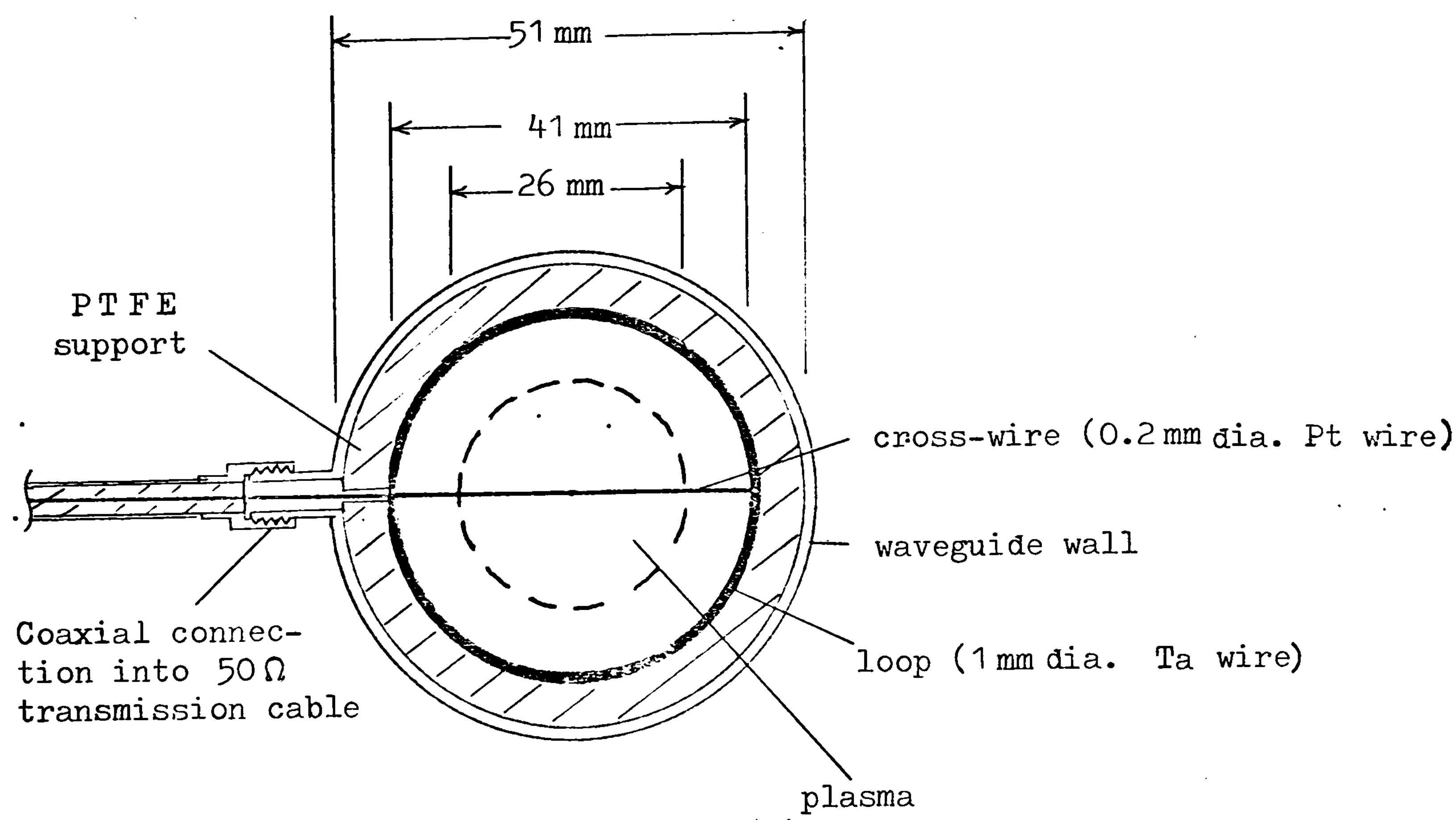

Fig.4.2(b)
Detail of r.f. probe design

Figure 4.3(a) shows the electronic sampling circuit. The transmitter continuously excites an electron plasma wave at a fixed frequency $\omega_o/2\pi$. The sampling oscilloscope samples after a fixed time-delay from the start of each voltage pulse from the main pulse generator, by measuring the amplitude of the received signal when the sampling gate is open, (duration 350 ps). The d.c. output of the sampling unit is the amplitude of this instantaneous signal averaged over many pulses, the number being determined by the external integrating circuit. As the transmitter-receiver separation is slowly increased, (at a rate ~ 0.2 cm s^{-1}), the d.c. output oscillates as the phase of the wave varies along the column, provided the phase of the transmitted signal does not change from sample to sample. This condition is maintained by triggering the sampling unit with a signal derived from both the voltage pulse and the transmitted signal, as shown in Fig.4.3(b).

The trigger level of the sampling unit is set to trigger when the r.f. output of the balanced mixer is close to a maximum. The sampling gate opens for fixed phase of the transmitted signal but at fixed time-delay after the start of each current pulse, with a jitter equal to the period of oscillation of the transmitted signal.

Thus the received signal is:

$$R(t) = A\cos\left(k_z(t)z - \omega_o t\right) \qquad \ldots (4.1)$$

where

$$\left|\frac{1}{k_z}\frac{dk_z}{dt}\right| \ll \omega_o .$$

If the sampling unit samples at $t = t_o$ for each pulse, then the d.c. output is:

$$Y(z) = \langle A\cos\left(k_z(t_o)z - \omega_o t_o\right)\rangle$$

$$= A\cos\left(k_z(t_o)z + \delta\right) \qquad \ldots (4.2)$$

where δ is a constant phase angle.

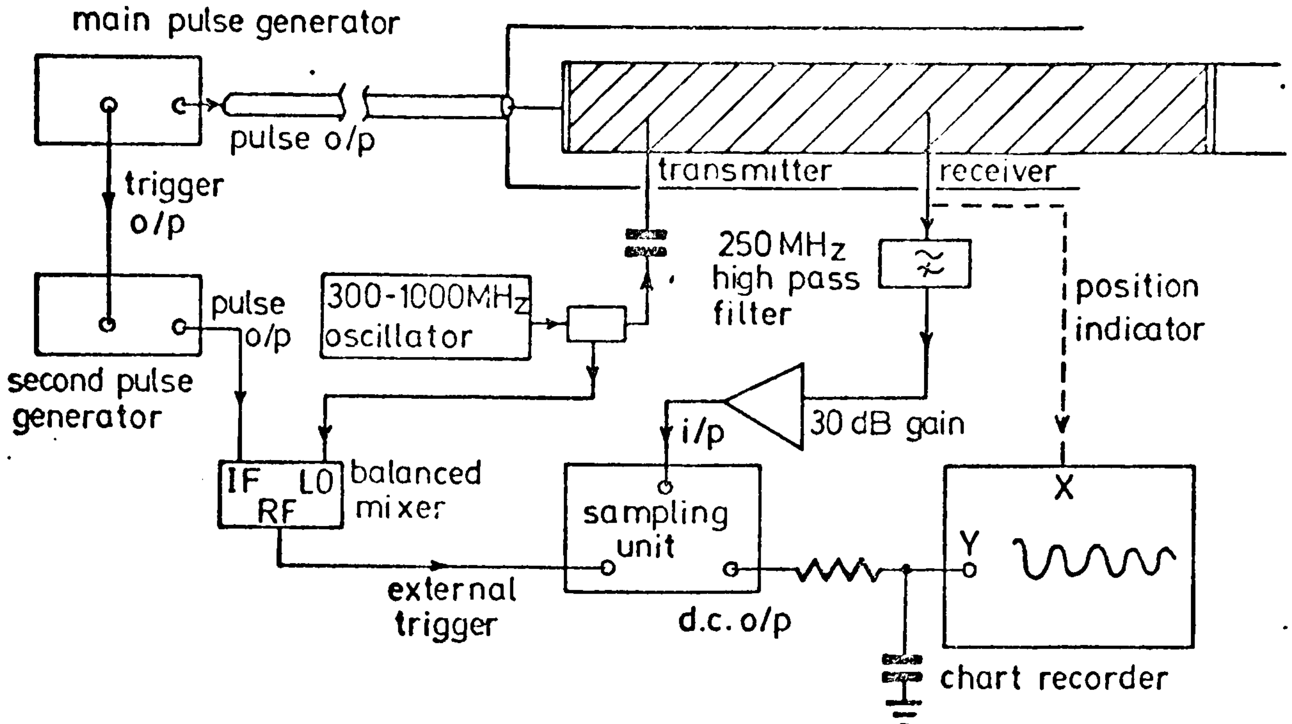

Fig.4.3(a)
Circuit for measuring time-resolved electron plasma wave dispersion

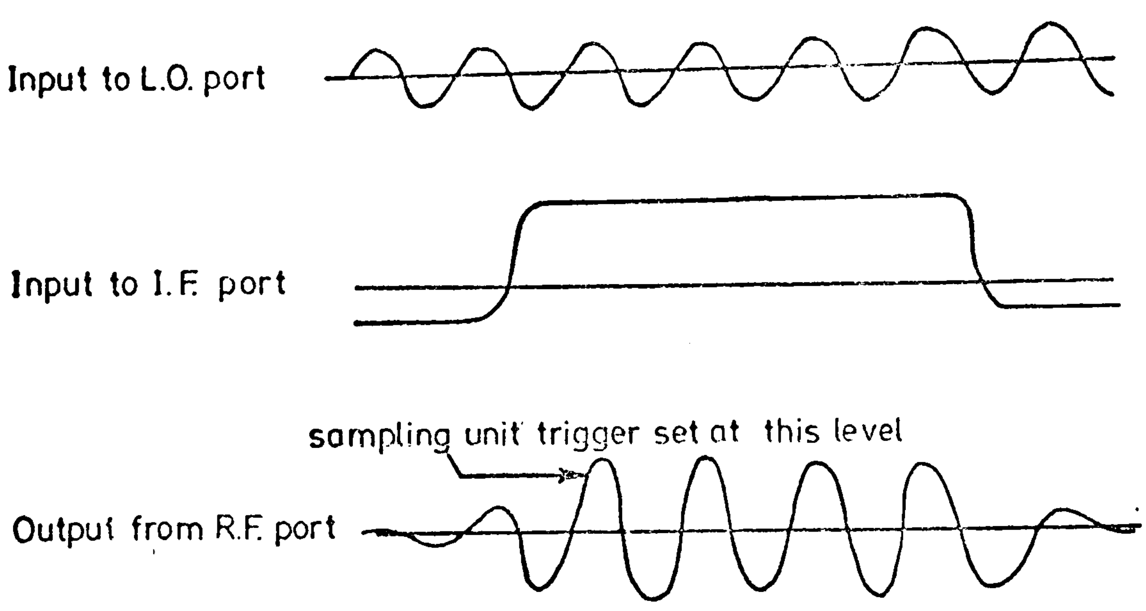

Fig.4.3(b)
Input and output signals at the balanced mixer

This signal is fed to the y-axis input of an x-y recorder and a voltage proportional to the probe separation is fed to the x-axis input. Measurements of the wavelengths parallel and antiparallel to the electron current are made by interchanging the transmitter and receiver probes, although the receiver will detect both waves, particularly at long wavelengths, because of reflections at the end plates.

In practice this is not a serious problem for moderate wavelengths. However it is possible to distinguish between the two waves by a modification shown in Fig.4.4(a). The time-delay for the sampling gate now varies in proportion to the transmitter-receiver separation.

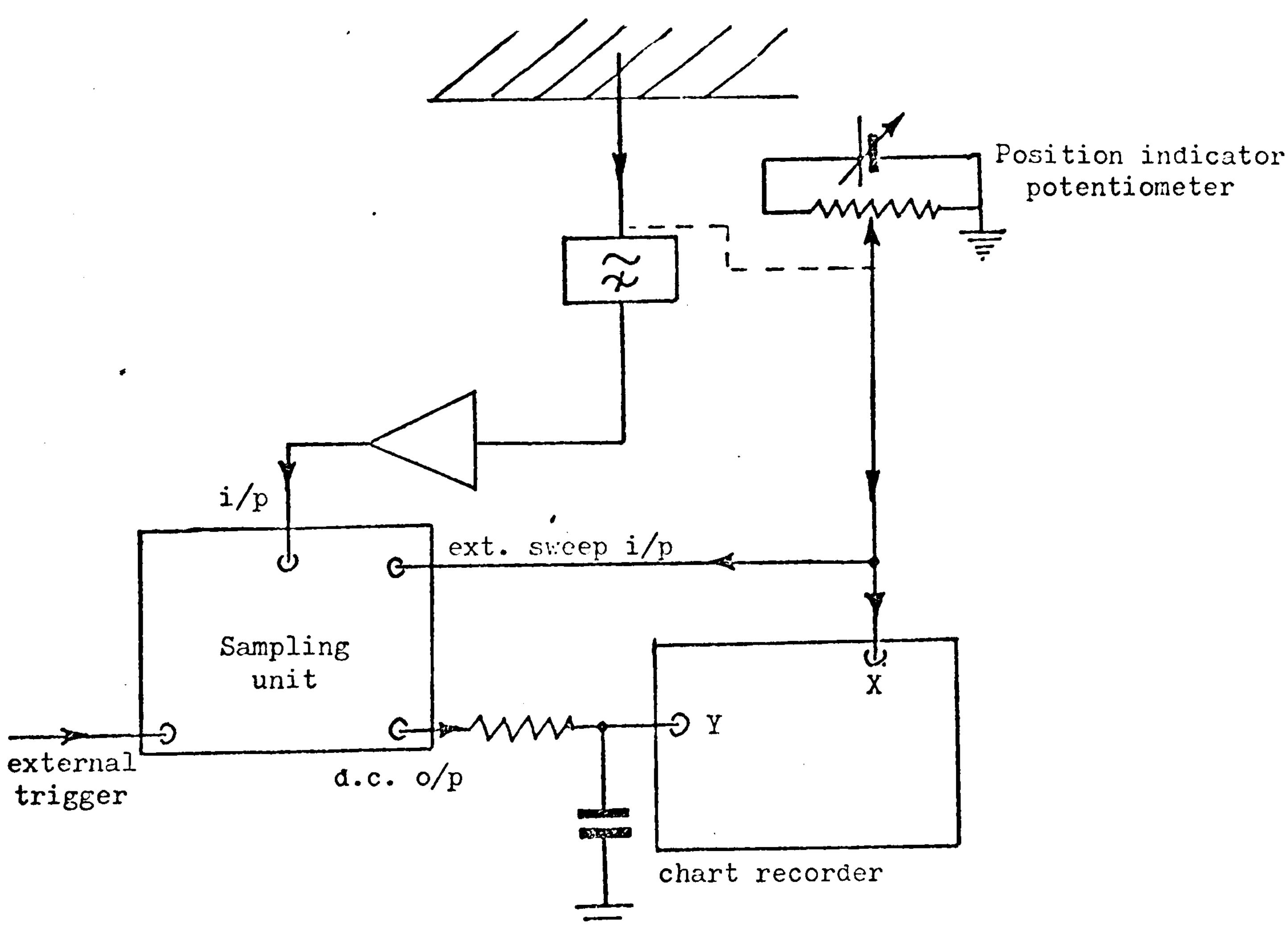

Fig.4.4(a)

Modification to circuit (Fig.4.3(a)) which varies the sampling gate time-delay in proportion to the transmitter-receiver separation

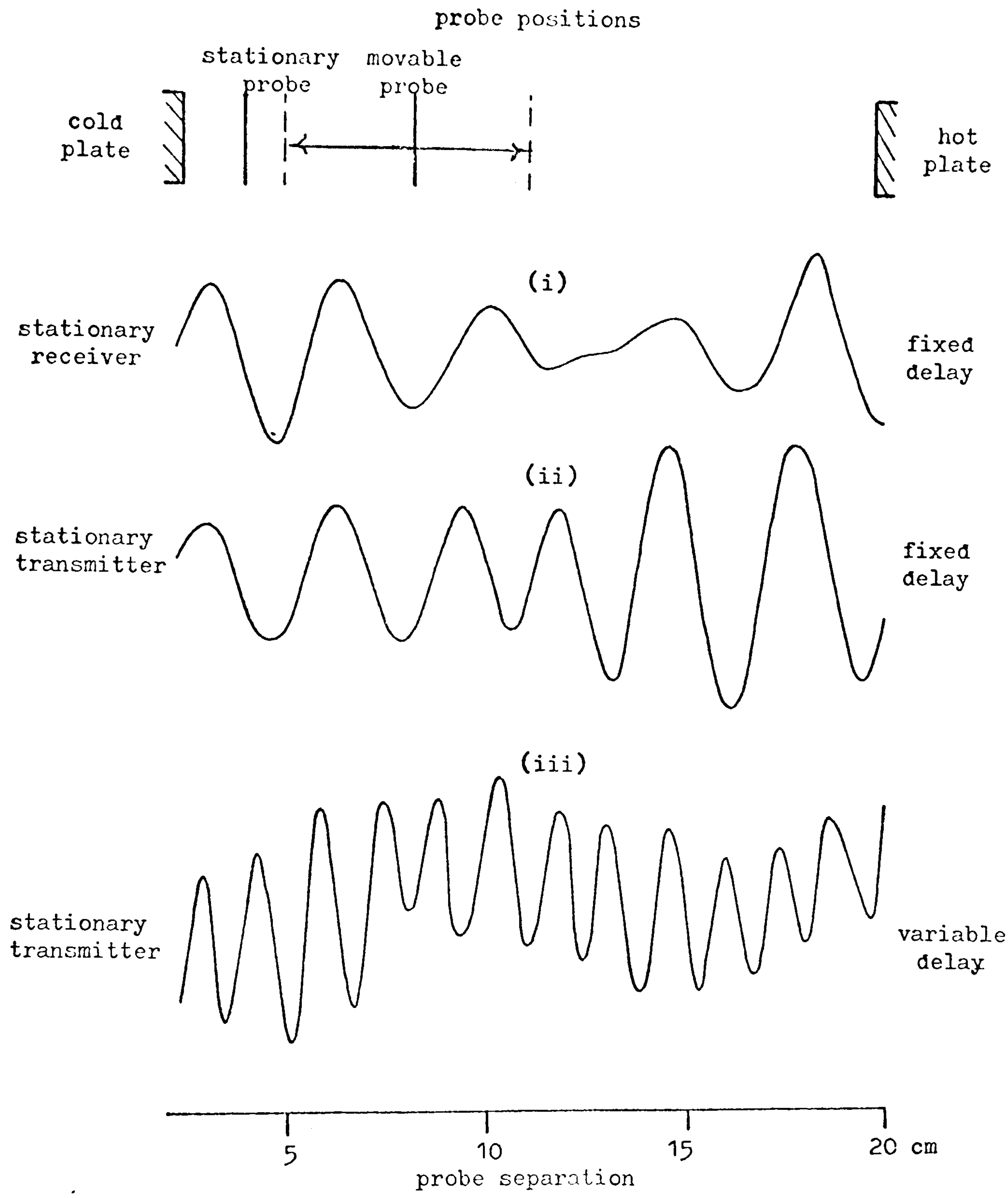

Fig.4.4(b)

An example of interferometer traces at $t = 0.3\,\mu s$ for a transmitter frequency $\omega_0/2\pi = 320$ MHz, plasma frequency $\omega_{pe}/2\pi = 540$ MHz

(i) & (ii) - traces obtained for parallel and antiparallel propagation respectively with a fixed sampling gate time-delay.

(iii) - Trace obtained with a time-delay which increases at a rate of $0.001\,\mu s$ per cm of probe separation; the antiparallel wavelength calculated from (4.8) is 2.8 cm.

The time-delay per unit distance α, is adjusted so that there is no phase variation with distance for one of the waves, but the phase variation of the other wave is now increased. The received signal is effectively sampled in the inertial frame of the wave with stationary phase and the observed frequency of the other is Doppler-shifted from the laboratory frame. Thus the received signal is

$$R(t) = A\cos(k_+(t)\, z - \omega_o t) + B\cos(k_-(t)\, z + \omega_o t) \qquad \ldots (4.3)$$

where the wavelengths $2\pi/k_+$ and $2\pi/k_-$ are for waves propagating in the +z and -z directions respectively, where $k_+ \approx k_-$. The sampling unit now samples at $t = t_o + \alpha z$, where

$$\omega_o^{-1} < \alpha\,(z_1 - z_2) \ll \left| \frac{1}{k_\pm} \frac{dk_\pm}{dt} \right|^{-1} \qquad \ldots (4.4)$$

Condition (4.4) requires that the maximum time-delay $\alpha(z_1 - z_2)$, is much shorter than the timescale for a change in the wavelength.

The d.c. output to the X-Y recorder is

$$Y(z) = \langle A\cos[k_+(t_o)z - \omega_o t_o - \alpha\omega_o z] + B\cos[k_-(t_o)z + \omega_o t_o + \alpha\omega_o z]\rangle \qquad \ldots (4.5)$$

If α is adjusted such that

$$k_+(t_o) = \alpha\omega_o , \qquad \ldots (4.6)$$

then equation (4.5) becomes:

$$Y(z) = A\cos\delta + B\cos(k_{eff} z + \delta) \qquad \ldots (4.7)$$

where the effective wavelength $2\pi/k_{eff}$, is related to the wavelength in the laboratory frame by

$$k_- = k_{eff} - \alpha\omega_o . \qquad \ldots (4.8)$$

An example is shown in Fig.4.4(b).

4.4 RESULTS

Figure 4.5 shows typical interferometer traces (with a fixed time-delay), for a particular frequency, where $t = 0$ is the beginning of the current pulse. At $t = 0$ the wavelengths are equal for both directions, but for $I > I_c$ and $t > 0$ the traces, which were taken between 15 and 35 cm from the cold plate, fall into two classes.

(a) $t < 0.2\ \mu s$

For $t < 0.2\ \mu s$ the traces indicate that the wavelengths are changing with position, implying that an initial transient propagates along the column. Interpretation of these results is facilitated by knowledge of the plasma behaviour for $t > 0.2\ \mu s$ so a discussion of this is postponed until section 4.7.

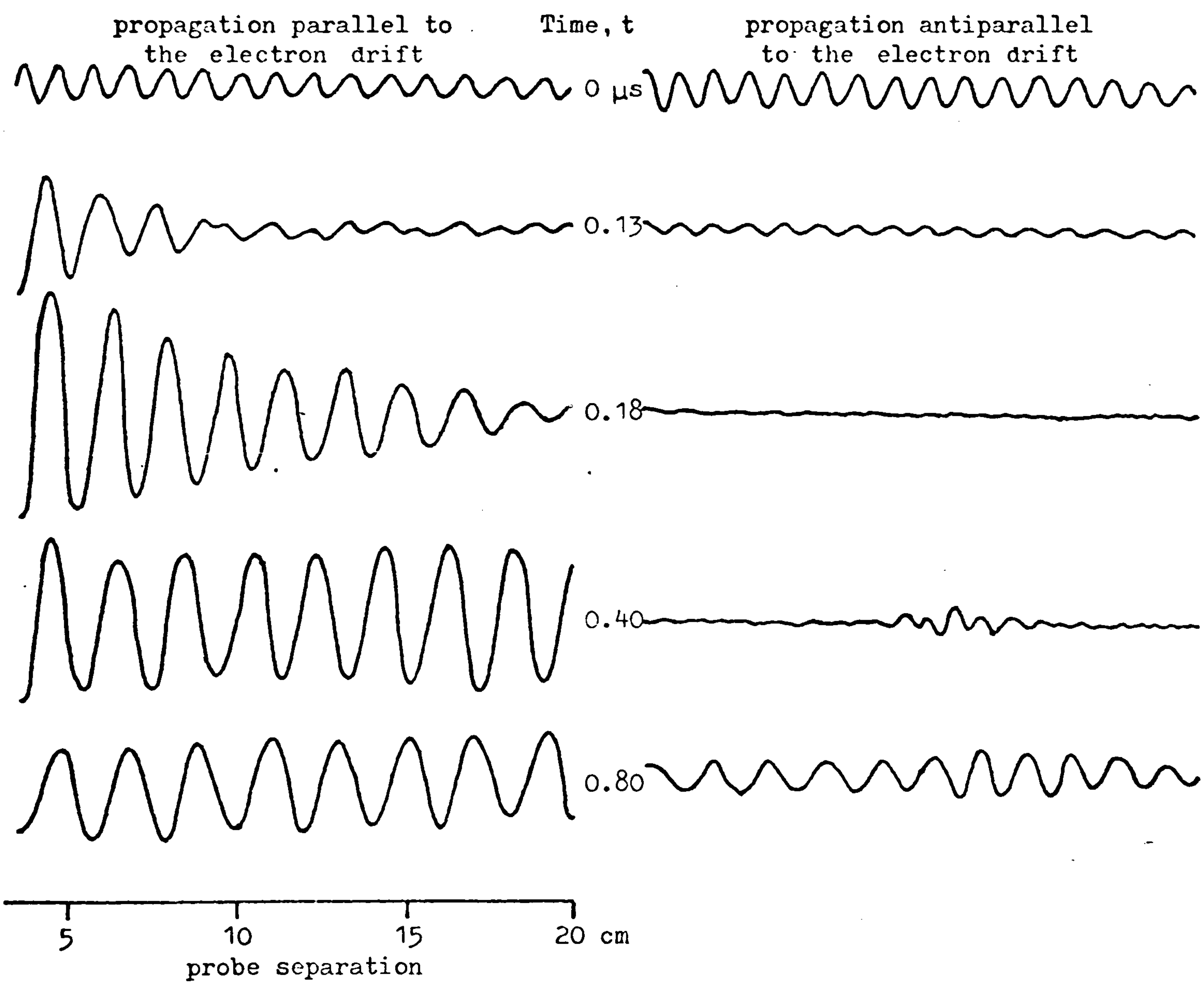

Fig.4.5

Typical interferometer traces at different times for transmitter frequency 720 MHz, plasma frequency 740 MHz

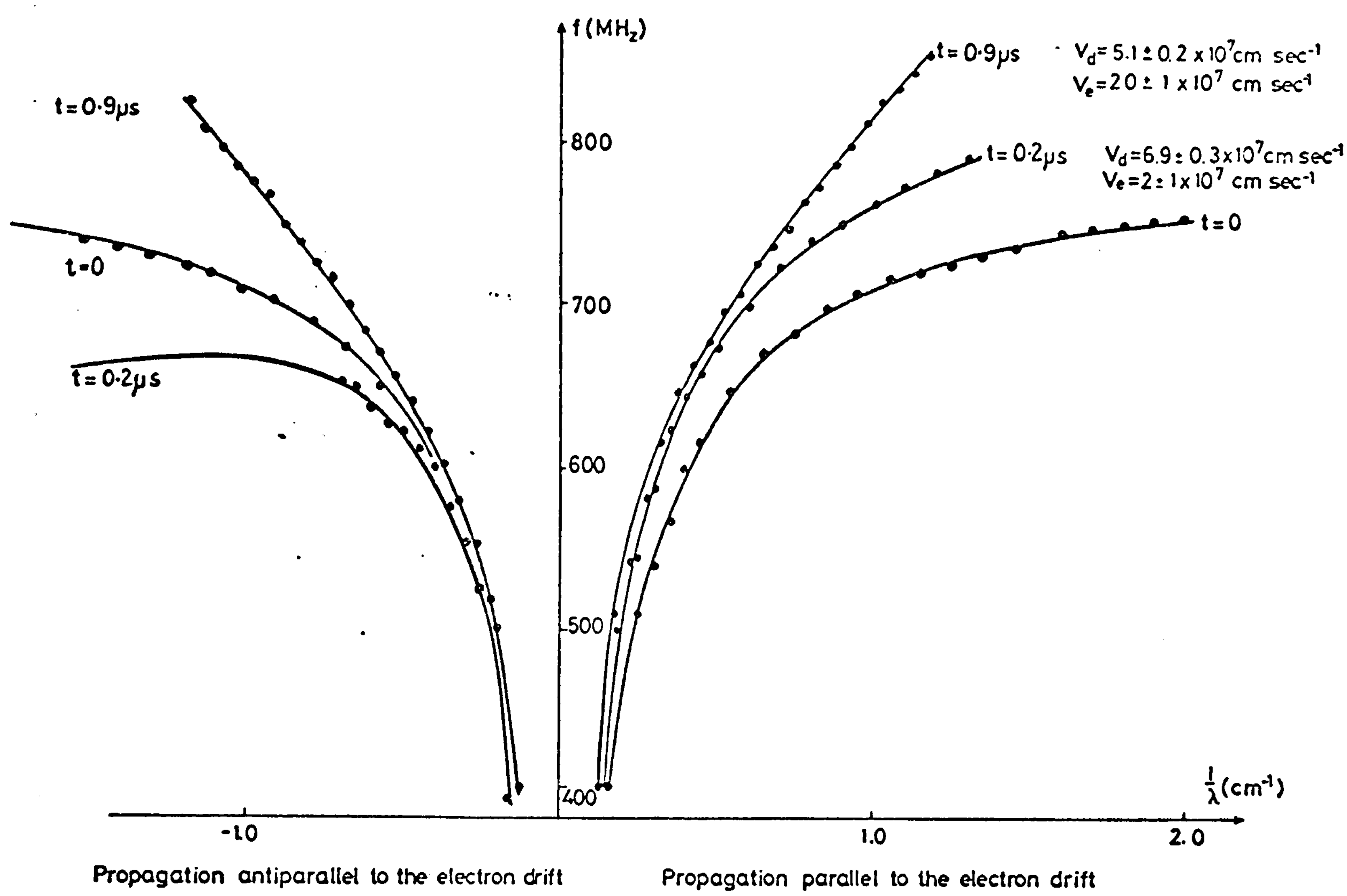

Fig.4.6

Typical measured dispersion curves for a pulse amplitude $V_o = 40\,V$

(b) $t \geqslant 0.2\ \mu s$

For distances ≤ 35 cm from the cold plate the wavelengths are spatially uniform and it is possible to measure the dispersion of undamped waves with wavelengths between 1 and 5 cm. Fig.4.6 shows a typical result for $t = 0$, 0.2 and 0.9 μs. The solid lines are theoretical curves fitted to the experimental data by the method outlined in the next section.

4.5 ANALYSIS

The analysis of the experimental data is the reverse of the usual theoretical problem, viz. given the dispersion of electron plasma waves $D(\omega, k_z)$, what is the distribution of electron velocities $F_e(v_z)$? Although in principle $F_e(v_z)$ can be determined uniquely from a complete knowledge of $D(\omega, k_z)$, a limited number of experimental points provides only restricted information of $F_e(v_z)$, i.e. the fitting parameters will be the low order velocity moments of $F_e(v_z)$. At first sight it would seem that three or more parameters can be fitted to the experimental data in an arbitrary manner. However the following analysis is a systematic fitting procedure in which the velocity moments are fitted in sequence with decreasing precision, starting at the zeroth order moment, followed by the first, and so on up to the fourth order moment, beyond which the uncertainty becomes greater than the estimate.

The details of the dispersion of electron plasma waves for boundary conditions found in the experiment are discussed in Appendix A.3, where it is shown that, in general the geometrical and thermal factors effecting $D(\omega, k_z)$ can be separated, viz :

$$\frac{\omega^2}{\omega_{pe}^2} = G(k_z) \int_{-\infty}^{+\infty} \frac{F_e(v_z)\, d\, v_z}{\left(1 - \frac{k_z v_z}{\omega}\right)^2} \quad . \qquad \ldots (4.9)$$

For the rest of the chapter the subscripts 'z' are implicitly understood.

Experimentally we measure how the dispersion changes from its initial form at $t = 0$, so that if we assume the column radius, a, does not alter between 0 and t we can eliminate $G(k)$ by taking the ratio

$$\left(\frac{\omega_t}{\omega_0}\right)^2 = \frac{n_t}{n_0} \; \frac{\left.\int_{-\infty}^{+\infty} \frac{F_e(v)\; dv}{(1 - kv/\omega)^2}\right|_t}{\left.\int_{-\infty}^{+\infty} \frac{F_e(v)\; dv}{(1 - kv/\omega)^2}\right|_{t=0}} \quad . \qquad \ldots (4.10)$$

where a wavelength $2\pi/k$, has frequencies ω_t at time t , and ω_0 at $t = 0$. If ω/k has a small imaginary part, (i.e. lightly damped waves), then the integrals in equation (4.10) can be evaluated to a good approximation by assuming ω/k as real and taking the principal value, (see e.g. JACKSON (1960)). For $\frac{\omega}{k} > v$, the denominator can be expressed in a binomial expansion and if we further assume that $F_e(v) \simeq 0$ for $v^2 \geq (\frac{\omega}{k})^2$, then:

$$\left.\begin{aligned}\int_{-\infty}^{+\infty} \frac{F_e(v)\,dv}{(1-kv/\omega)^2} &\simeq \int_{-\infty}^{+\infty} F_e(v)\left(1+2\frac{kv}{\omega}+3\left(\frac{kv}{\omega}\right)^2 \ldots\right) dv \\ &= \sum_{p=o}^{\infty} (p+1)\,\frac{A_p}{(\omega/k)^p} \\ \text{where} \qquad A_p &\simeq \int_{-\infty}^{+\infty} v^p\, F_e(v)\,dv \\ A_o &= 1\end{aligned}\right\} \qquad \ldots (4.11)$$

Initially we assume that the dispersion at $t=0$ is for a cold plasma so that the integral in the denominator of (4.10) is unity. Then equation (4.10) becomes:

$$\left.\begin{aligned}\left(\frac{\omega_+}{\omega_o}\right)^2 &= \frac{n_t}{n_o}\left[1+\frac{2A_1}{|\omega/k|}+\frac{3A_2}{|\omega/k|^2}+\ldots\right] \\ \left(\frac{\omega_-}{\omega_o}\right)^2 &= \frac{n_t}{n_o}\left[1-\frac{2A_1}{|\omega/k|}+\frac{3A_2}{|\omega/k|^2}-\ldots\right]\end{aligned}\right\} \qquad \ldots (4.13)$$

where the $+$ and $-$ subscripts refer to parallel and antiparallel propagation respectively.

Adding and subtracting the two expansions (4.13) for frequency ratios which have the same phase speed $|\omega/k|$, leads to :

$$\frac{1}{2}\Sigma = \frac{1}{2}\left\{\left(\frac{\omega_+}{\omega_o}\right)^2+\left(\frac{\omega_-}{\omega_o}\right)^2\right\} = \frac{n_t}{n_o}\left[1+3A_2\,\zeta+5A_4\,\zeta^2\ldots\right] \qquad \ldots (4.14)$$

$$\frac{1}{2}\frac{\Delta}{\sqrt{\zeta}} = \frac{1}{2}\frac{1}{\sqrt{\zeta}}\left\{\left(\frac{\omega_+}{\omega_o}\right)^2-\left(\frac{\omega_-}{\omega_o}\right)^2\right\} = \frac{n_t}{n_o}\left[2A_1+4A_3\,\zeta\ldots\right] \qquad \ldots (4.15)$$

where

$$\zeta = \frac{1}{(\omega/k)^2}\ .$$

Thus Σ and $\frac{\Delta}{\sqrt{\zeta}}$ can be computed from the dispersion data taken at time t, and $t=0$ and plotted as a function of ζ. Even and odd moments of $F_e(v)$ can be deduced from the coefficients of a least squares polynomial fit,(in practice no higher than a quadratic), to the two plots. The procedure is summarised schematically in Fig.4.7, and an example of the polynomial fitting shown in Fig.4.8(a).

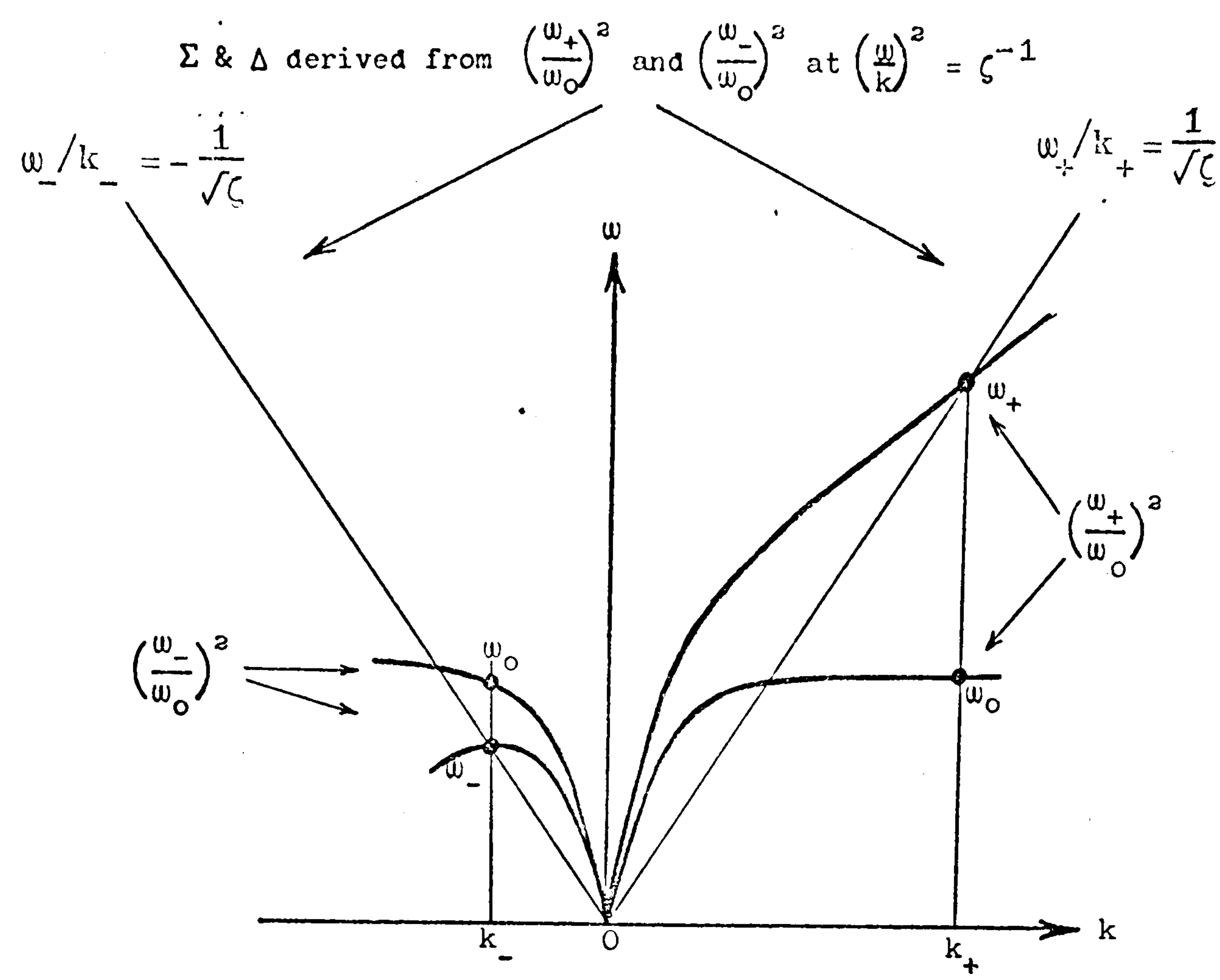

Fig.4.7
Scheme for computing Σ and Δ

The three assumptions made in the analysis can be checked *a posteriori*. Firstly the assumption that G(k) remains constant between 0 and t. This assumes that the radial density profile, which effects the dispersion at long wavelengths, does not change between 0 and t. Inspection of the plots of Σ and $\Delta/\sqrt{\zeta}$ for small ζ (i.e. long wavelengths), indicates that this is not so, (see Fig.4.8(a)). After the coefficients have been fitted to Σ and $\Delta/\sqrt{\zeta}$ it is possible to work backwards from the long wavelength data points and determine how the long wavelength dispersion has changed at time t, due to a change in the radial density profile. The result of this procedure is shown in Fig.4.8(b) suggesting that the density profile broadens at later times (*cf* Fig.4.1(a)), however it is difficult to deduce reliable quantitative data from such a measurement.

Secondly, the assumptions for the validity of the expansion (4.11) can be checked by ensuring that velocities computed from the fitted coefficients are much smaller than the phase velocities of the waves used in the analysis. A consequence of this is that the value of $\frac{1}{2}\Sigma$ must

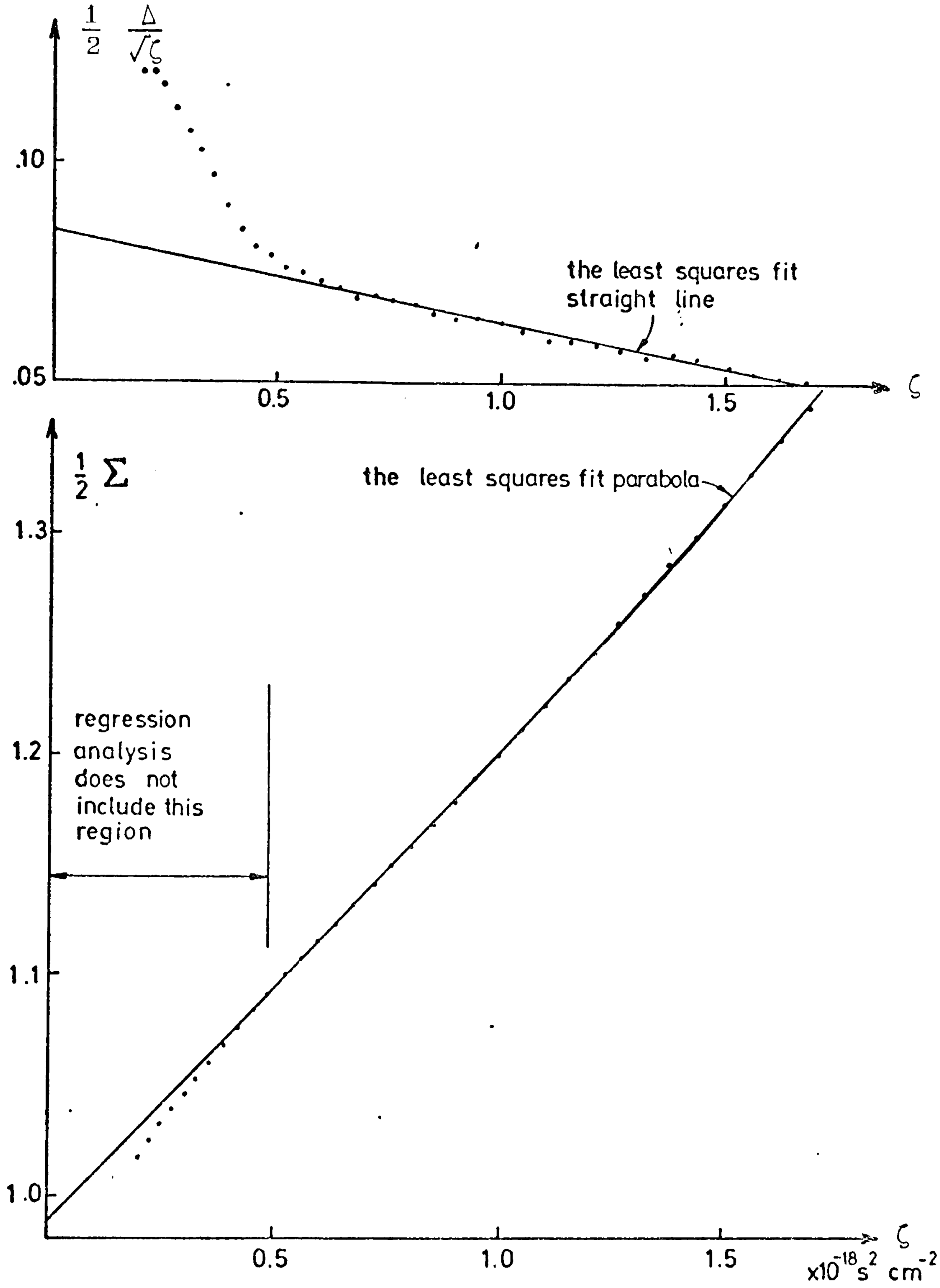

Fig.4.8(a)
Graphical determination of the first five velocity moments of the electron distribution function

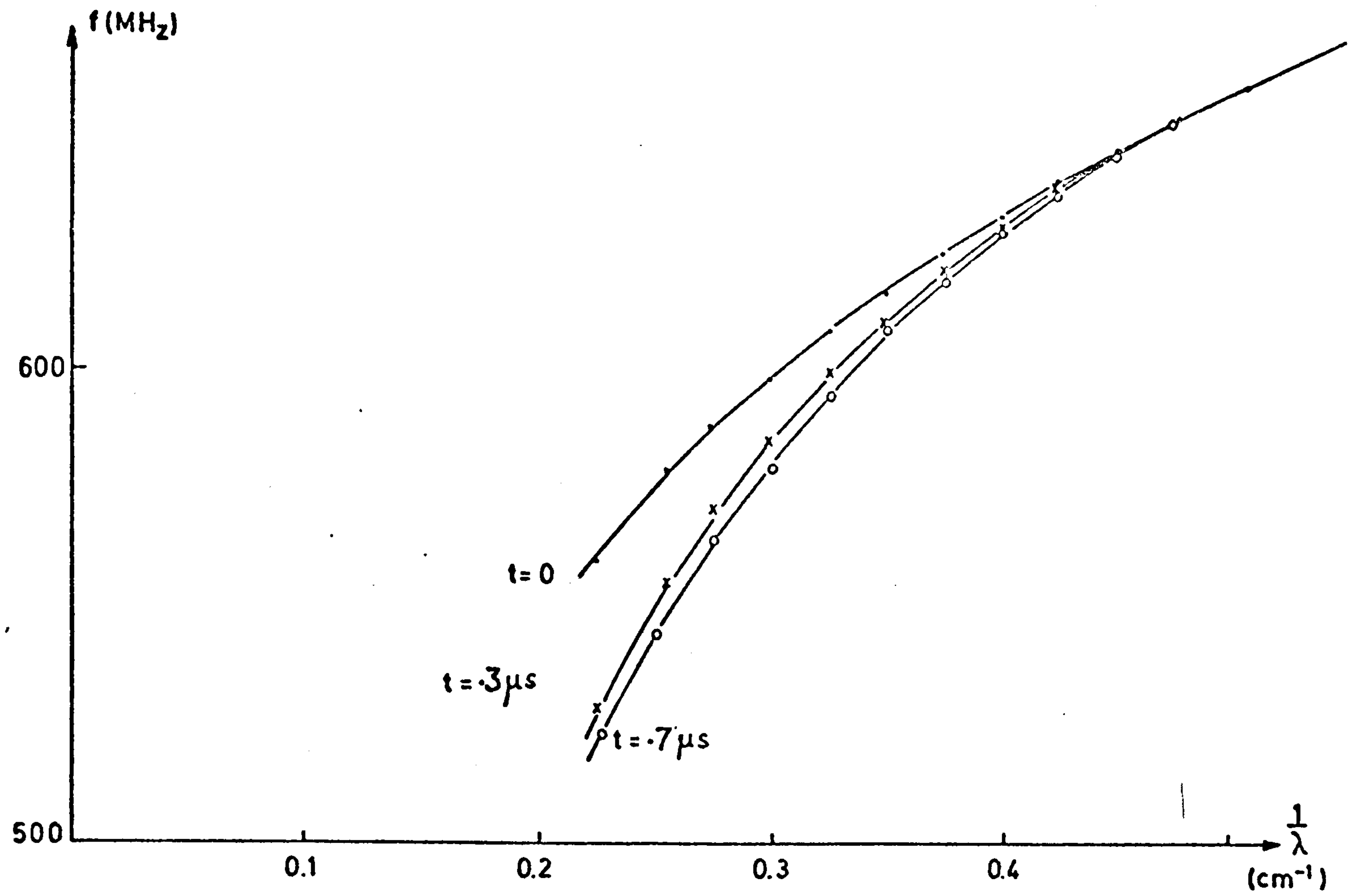

Fig.4.8(b)
The change of the long wavelength dispersion in the electron drift frame for a pulse amplitude $V_o = 100\,V$, $n_o = 6\times10^9\ cm^{-3}$

always be close to unity, (in practice $0.8 \leqslant \frac{1}{2}\Sigma \leqslant 1.4$).

Thirdly, the assumption that the dispersion for a cold plasma can be used at $t = 0$ is checked by estimating the correction to equation (4.10) for a finite temperature plasma at $t = 0$; i.e. if

$$\left(\frac{\omega_o}{\omega_{pe}}\right)^2 \simeq G(k)\left[1 + \frac{3v_{eo}^2}{(\omega_o/k)^2}\right] \qquad \dots (4.16)$$

where $v_{eo} = 2\times10^7\ cm\ s^{-1}$, then the correction to term A_2 in equation (4.12) is $\sim v_{eo}^2$, and the correction to term A_3 is $\sim \frac{3}{2}v_{eo}^2 v_d$. These corrections are smaller than the uncertainties in A_2 and A_3.

4.6 DISCUSSION OF THE RESULTS FOR $t > 0.2\,\mu s$

A series of measurements of the dispersion for $t > 0.2\ \mu s$, were taken at two plasma densities with pulsed current amplitudes, $I > I_c$. In order to achieve reasonable accuracy, about forty points are required for each dispersion curve so that collecting and analysing data is very time-consuming. In Appendix A.4 there is a description of two variants of the basic technique which can be used to speed up the process.

Figure 4.9 shows the evolution of the first five velocity moments in the electron rest frame for

$$0.4 \le t \le 0.9 \ \mu s$$

where

$$\left.\begin{aligned} v_d &= \int_{-\infty}^{+\infty} v \, F_e(v) \, . \, dv \\ v_e^2 &= \int_{-\infty}^{+\infty} (v-v_d)^2 \, F_e(v) \, dv \\ v_a^3 &= \int_{-\infty}^{+\infty} (v-v_d)^3 \, F_e(v) \, dv \\ v_b^4 &= \int_{-\infty}^{+\infty} (v-v_d)^4 \, F_e(v) \, dv \end{aligned}\right\} \quad \ldots (4.17)$$

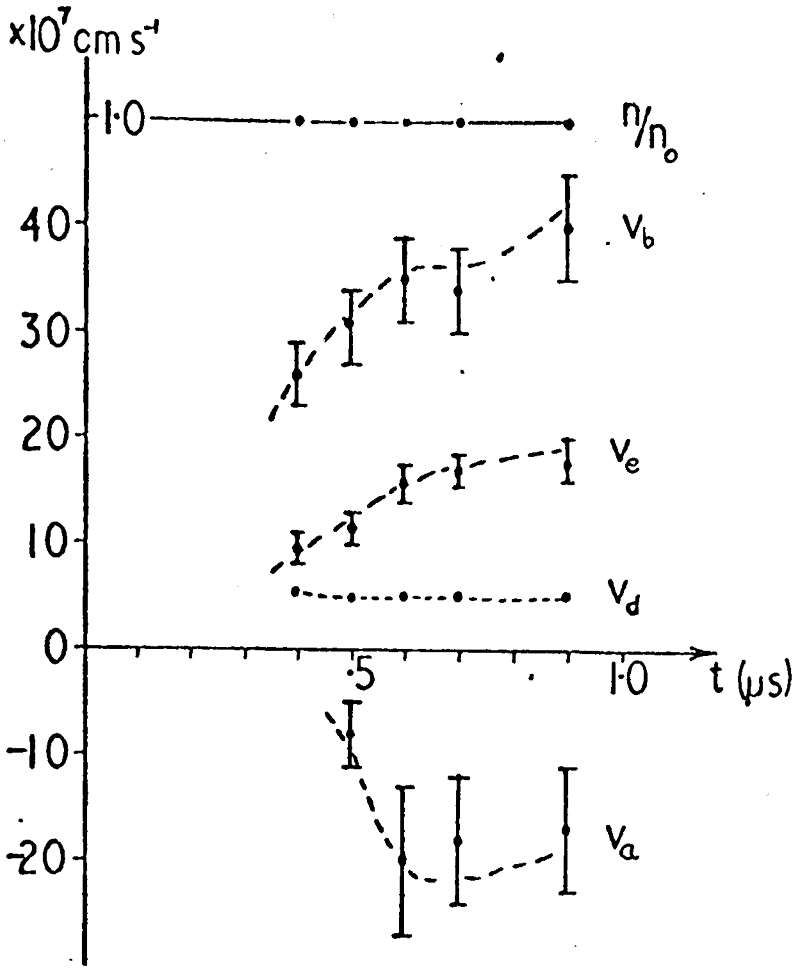

Fig.4.9
Evolution of the first five velocity moments of the electron distribution function parallel to B_z (in the electron frame); $n = 6 \times 10^9 \ cm^{-3}$, $V_o = 40 V$

This data exhibits the following general features:

(a) The electron density for $0.4 \le t \le 0.9 \ \mu s$ remains constant and equal to the initial density n_o.

(b) The drift velocity remains more or less constant during this period, and the product

$$I = - n_o \, e \, v_d A \qquad \ldots (4.18)$$

is consistent with the current measured at the cold plate.

(c) The electron r m s velocity v_e, very quickly exceeds v_d and continues to increase implying substantial electron 'heating'.

(d) Although there is a large uncertainty in the estimate of v_a it definitely becomes negative, i.e. in the ion rest frame v_a has the <u>opposite sign</u> to v_d.

Thus in the electron drift frame, $F_e(v - v_d)$ is asymmetric (as is also the wave dispersion when Doppler-shifted by kv_d). This indicates that in velocity-space the electron velocities are preferentially scattered towards the direction of the ion drift, see Fig.4.10.

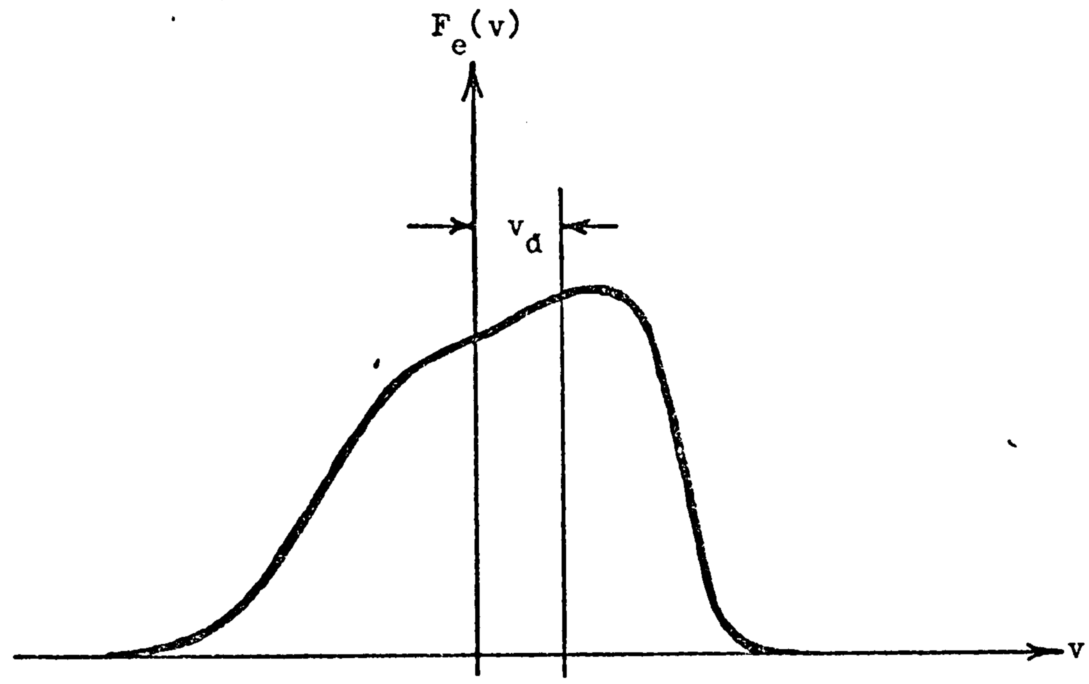

ion zero-momentum frame   electron zero-momentum frame

Fig.4.10

Shape of $F_e(v)$ when $\int v^3 F_e\, dv$ has the opposite sign to $\int v F_e\, dv$ in the ion rest-frame

Figure 4.11 shows the evolution of n, v_d and v_e between 0.2 and 2 μs for different pulsed currents at two densities. Generally, as the voltage across the plasma V_{pl} is increased, the density decays more rapidly and v_e reaches a maximum at earlier times, while the drift is more or less constant. The maximum value for $\frac{1}{2} m v_e^2$ is close to $e V_{pl}$ implying that most of the electrical dissipation has gone into increasing the parallel kinetic energy; e.g. for $n = 6 \times 10^9$ cm^{-3}, $V_{pl} \simeq 60\,V$, $I \simeq 600\,mA$ for 1 μs, thus the energy input $\simeq 36 \times 10^{-6}$ J, while the column contains a total of $\sim 2.4 \times 10^{12}$ electrons. If distributed uniformly, this represents a maximum energy of ~ 90 eV per electron compared with the maximum value of $(\frac{1}{2} m v_e^2)_{parallel} \sim 70$ eV.

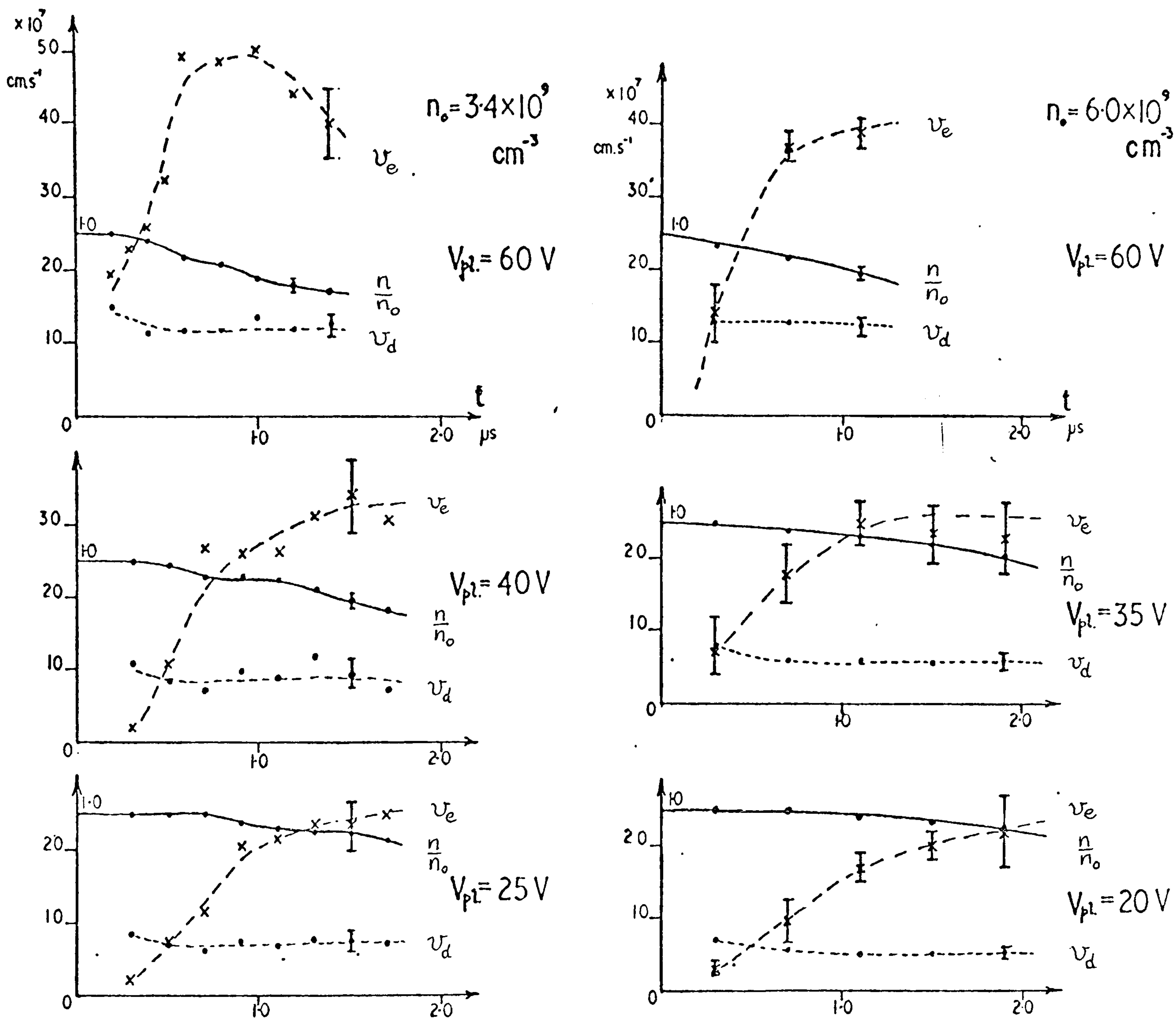

<u>Fig.4.11</u>
Evolution of n, v_d and v_e (in the electron frame), for different pulsed currents at two densities

Figure 4.12 shows that the relation between the maximum value of v_e and the time taken to reach it is consistent with a simple picture of a kinetic energy confinement time $\propto \ell/v_e$.

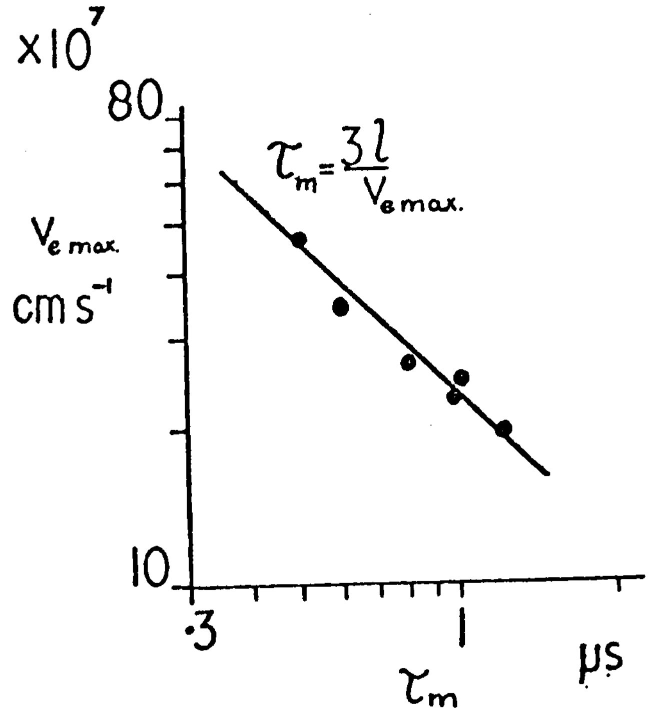

Fig.4.12
Relation between the time taken τ_m, for v_e to reach a maximum value $v_{e\,max}$

It is possible to estimate the effective electron-ion collision frequency ν_{eff}, from the initial rate of increase of v_e assuming more or less constant n and v_d, i.e. power dissipated per unit volume = $J E_o$, where J is the electron current density. With a steady drift velocity, $-eE_o = m v_d \nu_{eff}$. If we assume that all the dissipation goes into increasing the electron kinetic energy parallel to the drift, then:

$$J E_o = \frac{d}{dt}\left(\tfrac{1}{2} n m v_e^2\right). \qquad \dots (4.19)$$

Substituting for J and E_o:

$$\nu_{eff} = \frac{1}{2v_d^2}\frac{d(v_e^2)}{dt} \approx \frac{1}{2\,v_d^2}\frac{\Delta(v_e^2)}{\Delta t}. \qquad \dots (4.20)$$

In Fig.4.13, $\Delta(v_e^2)/v_d^2$ is plotted against Δt for the results at $n = 6 \times 10^9\ \text{cm}^{-3}$ showing that ν_{eff} has about the same value for all three currents. This result does not occur at the lower density, $n = 3.4 \times 10^9\ \text{cm}^{-3}$ but as Fig.4.14 shows the estimates of σ from ν_{eff} are consistent with the values estimated from the plasma column current-voltage characteristic at $t = 1\ \mu s$.

In Fig.4.14 the conductivity has been scaled with plasma frequency in order to compare the results with the scaling law (1.12) found by Hamberger and Friedman, (cf. Fig.3.7). The horizontal axis shows the

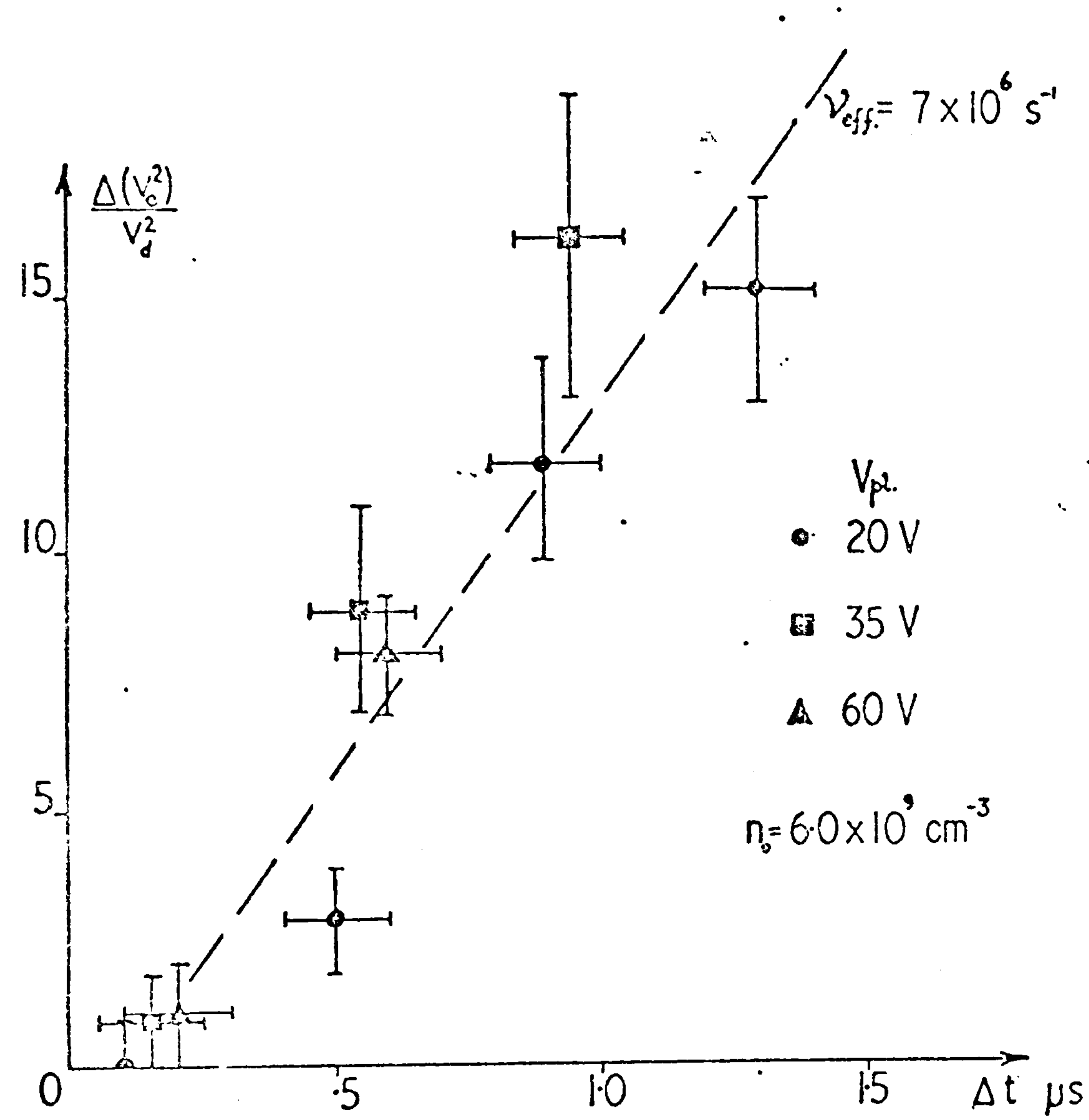

Fig.4.13

Estimation of ν_{eff} from the electron 'heating' rate

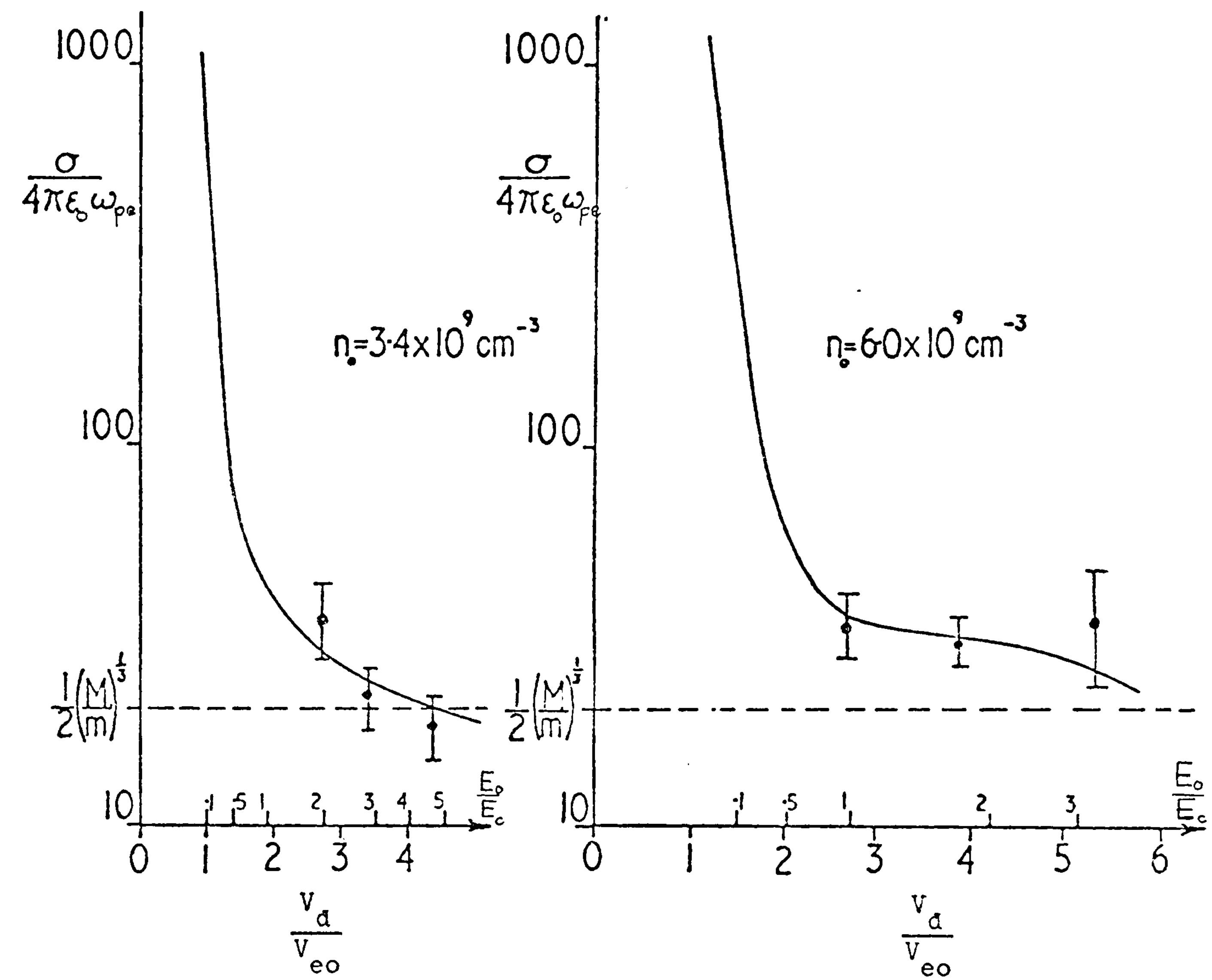

Fig.4.14

The relation between conductivity, σ, and drift velocity, v_d, for two densities. Solid line: estimate of σ from the I-V relation at 1μs; points: value of σ from the estimate of ν_{eff}

drift velocity (computed from equation (4.18)) normalised to the thermal velocity at $t = 0$. Also shown are the corresponding values of E_o/E_c at 1 μs (where E_o is computed from equation (3.4)).

With these results in mind we return to the initial stages of the current pulse.

4.7 THE INITIAL TRANSIENT (for $I > I_c$)

For pulsed currents $I > I_c$, before a uniform electron drift exists in the plasma column, there is an initial phase which is characterised by the following observations.

(a) For $t < 0.2$ μs (in the region 5 to 35 cm from the cold plate) the 'parallel' wave has a wavelength discontinuity which propagates towards the hot-plate while the 'anti-parallel' wave disappears if the frequency is close to $\omega_{pe}/2\pi$, (see Fig.4.5). This implies that an electron drift discontinuity propagates from the cold plate to the hot plate as shown schematically in Fig.4.15.

(b) This effect is not observed if $I < I_c$. (The dispersion measurements for $I < I_c$ are consistent with the predictions of the collisionless theory presented in Chapter III although the technique is not very sensitive to changes of $v_d < v_e$).

(c) The propagating drift discontinuity cannot be explained by the collisionless theory in Chapter III, because the estimated time for the discontinuity to reach the hot plate (~ 0.5 μs) is an order of magnitude greater than ℓ/u.

(d) The estimated time for a uniform electron current to be established in the column is equal to the duration of the current overshoot, (see Fig.3.3(b)).

(e) When the drift has become spatially uniform along the column, the density is the same as the initial density n_o.

(f) The phenomenon is associated with the onset of plasma resistivity.

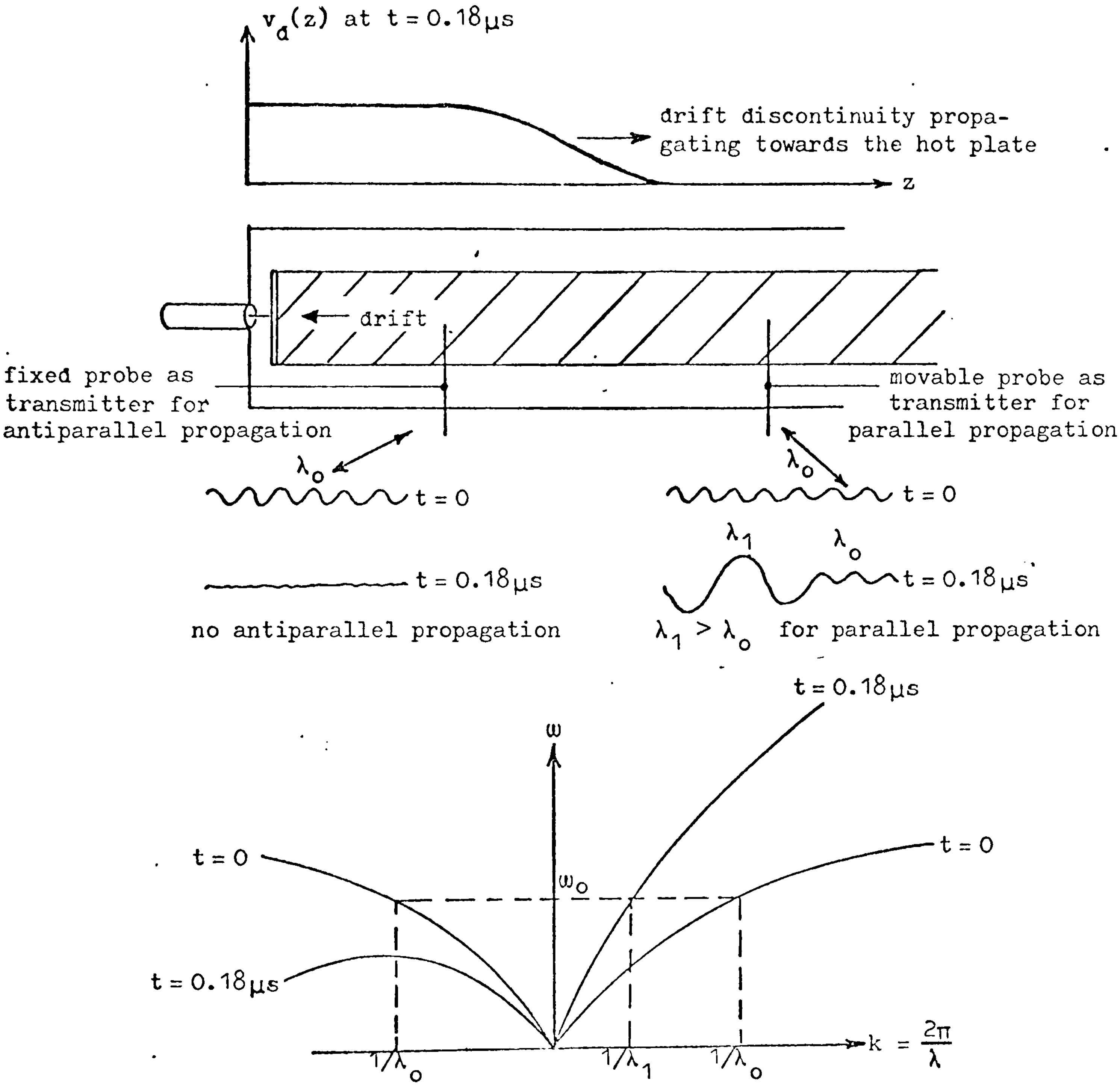

Fig.4.15

Dependence of parallel and antiparallel propagation at a fixed frequency $\omega_o/2\pi$, on the presence of a propagating electron drift discontinuity.

It might be possible to describe this transient with a theoretical model similar to the collisionless theory but with a phenomenological collision frequency ν_{eff}, in the 1-D electron momentum equation. Unfortunately the propagation velocity of the drift discontinuity is of the same order as the drift velocity so that it is not possible to linearise the momentum equation by neglecting $v \frac{\partial v}{\partial x}$; also the long scalelength approximation for Poisson's equation (3.11) may not hold in this problem. Thus even a simple cold fluid model requires a nonlinear solution of the electron continuity and momentum equations in conjunction with Poisson's equation. However, it is possible to discuss the physics of the phenomenon by making deductions from the experimental observations.

It would appear that there are two stages in the establishment of a large uniform electron drift $v_d \gg 1.3\, v_e$, in the plasma column. Firstly, as the potential of the cold plate is raised to $\sim 100\,V$ with rise-time τ_R, a potential ramp begins to propagate away from the cold plate as predicted by the collisionless theory. However when the electrons close to the cold plate have been accelerated to $v_d > 1.3 v_e$, the two-stream instability is excited, causing them to experience a deceleration due to the enhanced collision frequency, ν_{eff}. The space-charge density changes in such a way that the ramp 'collapses' and the potential difference is dropped across a short distance. (A small part of the ramp is left undeformed and separates from the main part to propagate back and forth in the column, as predicted by the collisionless theory.) The process is illustrated in Fig.4.16.

The dynamics of this potential front cannot be described by a collisionless theory. The experimental observations suggest it has three more or less distinct regions:

(a) A space-charge limited sheath adjacent to the cold plate where the potential drop, $V_s = I^{\frac{2}{3}}/K^{\frac{2}{3}}$.

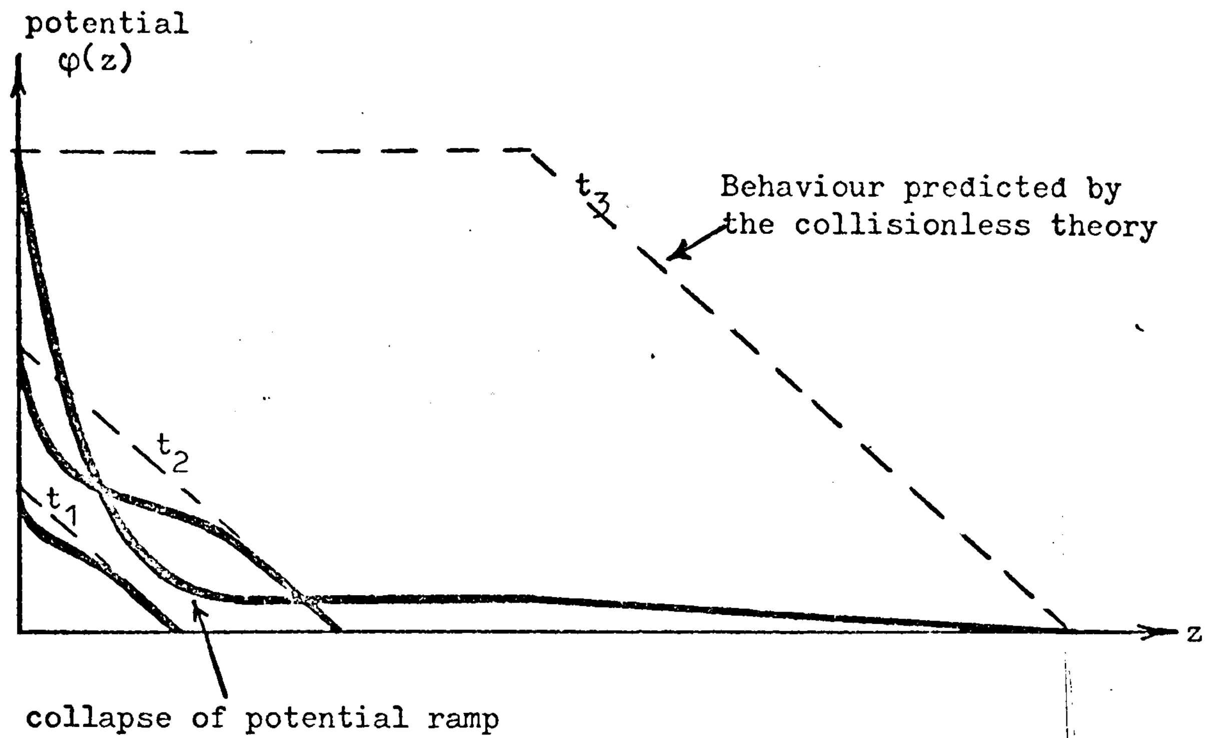

Fig.4.16
The inital stages of the transient for
$I \gg I_c$, $t_3 > t_2 > t_1$

(b) A region ($0 < z \leq s$) of more or less uniform electric field which maintains a uniform electron drift v_d, in a resistive plasma so that the potential drop V_σ, is given by

$$V_\sigma = \frac{I\,s}{\sigma A} \quad . \qquad \ldots (4.21)$$

(c) An acceleration region, i.e. a region where the conduction current is discontinuous, which propagates along the column with a velocity $\sim v_d$ establishing an electron drift but leaving the electron density unchanged from its initial value after it has passed by. The total current continuity is maintained by a displacement current, $\epsilon_0 \frac{\partial E}{\partial t}$. Because of the relatively slow propagation velocity, the electron continuity equation requires the potential profile of the acceleration region to change as it propagates. To illustrate this, consider an inertial frame z', travelling at the same velocity as the acceleration region, then as Fig. 4.17 shows, in order to maintain the same electron density before and after acceleration

$$\int_{\text{accel. region}} \frac{\partial n}{\partial t} \cdot dz' \approx n v_d \,. \qquad \ldots (4.22)$$

The displacement current is related to $\frac{\partial n}{\partial t}$ by Poisson's equation, hence it is impossible to find an inertial frame where $\frac{\partial \varphi}{\partial t} = 0$. This is to be contrasted with the collisionless theory where, for the propagation velocity, $u \gg v_d$, so that the potential ramp propagates along the column

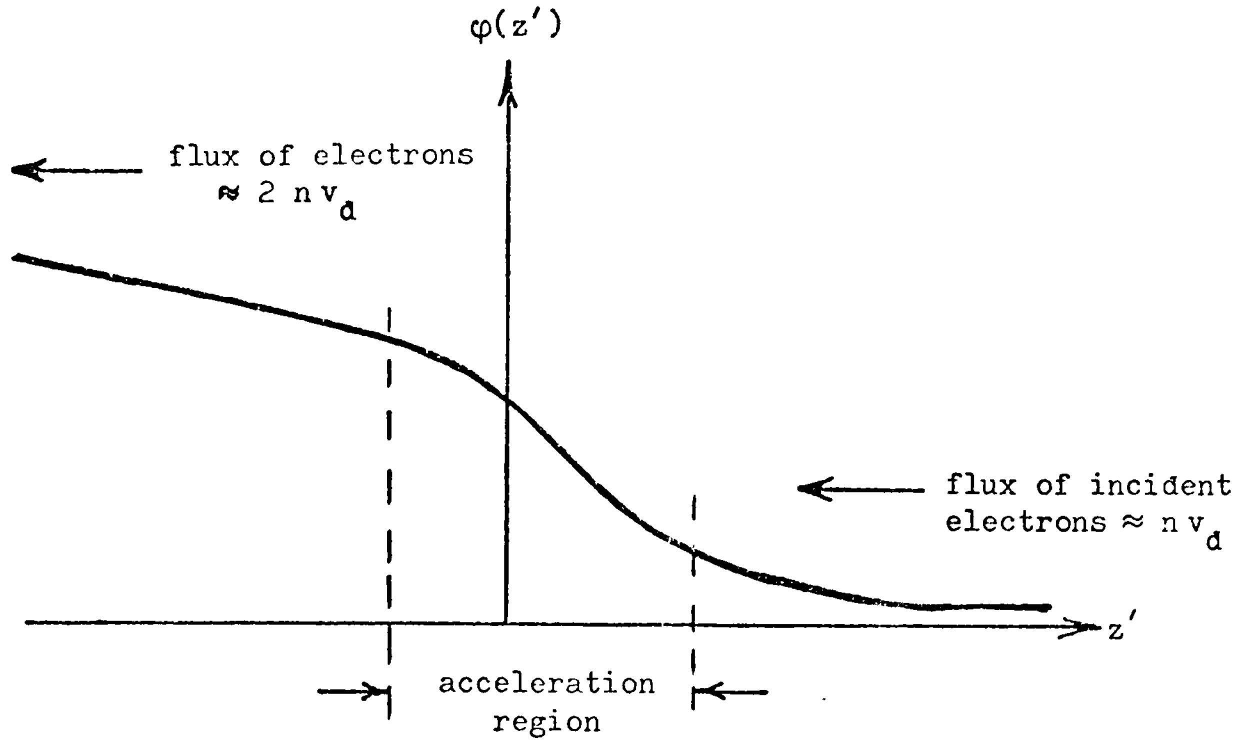

Fig.4.17
Potential profile in an inertial frame travelling at the same velocity as the acceleration region

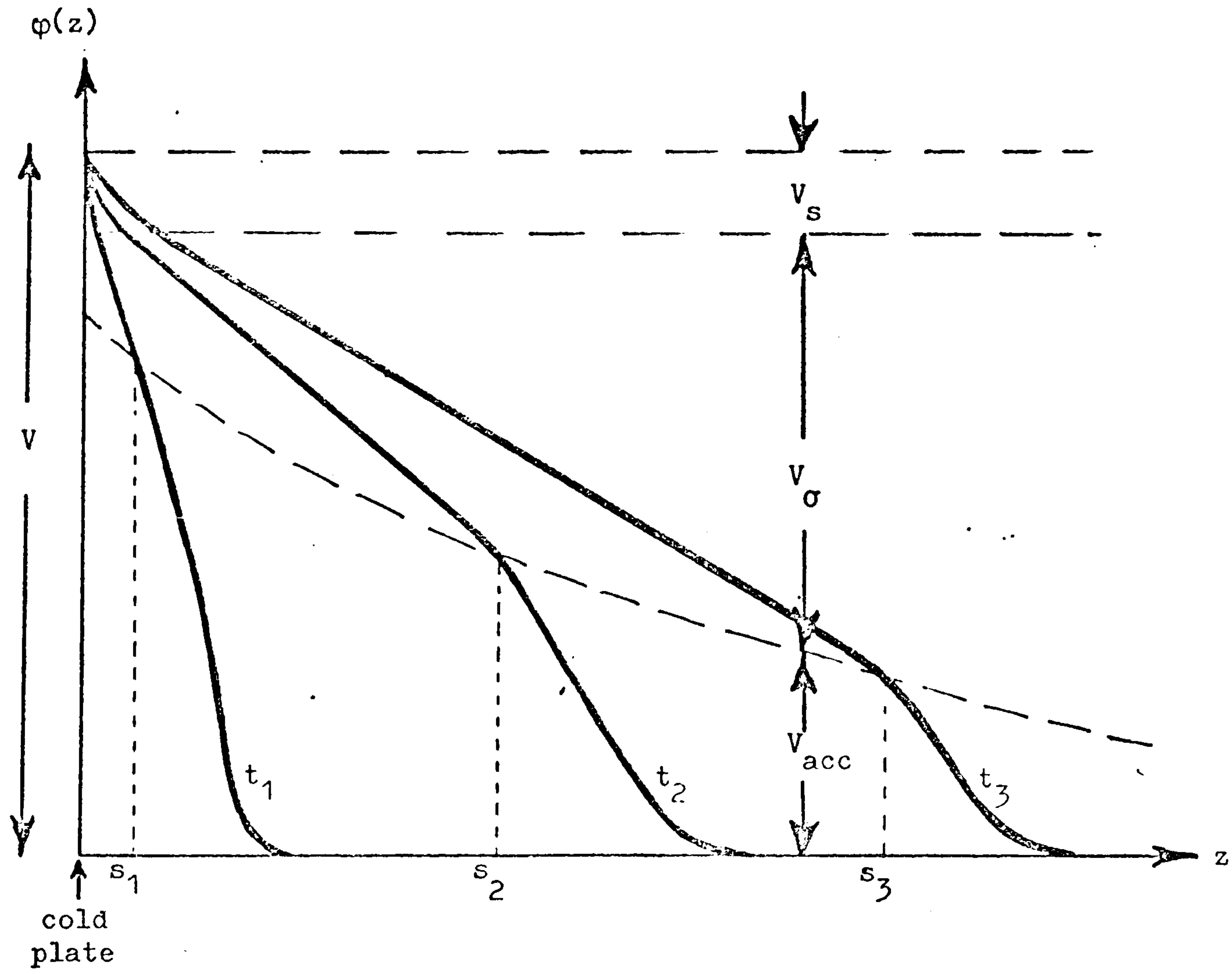

Fig.4.18
Schematic of the propagation of the potential front in a resistive plasma. $t_3 > t_2 > t_1$

undistorted leaving the density unchanged. (In the collisionless theory the displacement current is the changing radial electric field between the plasma and the waveguide wall, whereas in this case it is not clear where the major contribution to the displacement current is flowing. If the acceleration region is changing over scalengths $\geqslant a$ then the radial component of $\partial E/\partial t$ may be significant.)

Thus we can explain in a qualitative manner, how the current overshoot evident in Fig.3.3(b), occurs. In the early stages, just after the collapse of the potential ramp (Fig.4.16), $V_{acc} \simeq V$, so that the initial rising current observed at the cold plate is due to the acceleration of electrons by a comparitively large field in the region close to the cold plate. As the acceleration region moves along the column, its potential drop V_{acc}, decreases because $V_{\sigma} \propto s$, (see Fig.4.18). Thus the drift velocity of those electrons leaving the acceleration region and entering the uniform region, also decreases. In the uniform region the displacement current is very small, so that the current at the cold plate is proportional to the drift velocity produced by the acceleration region. Hence the current passes through a maximum and begins to decline. This decline ceases when the acceleration region has reached the hot plate, after which a more or less uniform drift prevails throughout the column.

4.8 CONCLUSION

In this chapter we have described how the measurement and interpretation of the dispersion of long wavelength electron plasma waves facilitates an elementary understanding of the response of the plasma to a large positive potential step applied to the cold plate. This diagnostic has indicated how the initial transient establishes an electron drift in the column without greatly effecting the initial quiescent density, (which is determined by the ion equilibrium), over a timescale $\sim 2\ \mu s$. If the electron drift velocity exceeds $1.3\sqrt{\frac{KT_e}{m}}$ (where $T_e = T_i$), the results from the dispersion and electrical measurements consistently indicate that the plasma has an anomalous conductivity σ. The estimates of σ are consistent with the empirical scaling law (1.12) found by Hamberger and Friedman in a pulsed toroidal discharge in a different density regime and with different ion masses, although the dispersion measurements indicate that limitations imposed by end losses make it difficult to determine how σ depends on n and E_o in this experiment. Further comment will be made in Chapter VI.

CHAPTER V

THE FLUCTUATION SPECTRUM

5.1 INTRODUCTION

This chapter concerns the potential fluctuations detected by electrostatic probes during the current pulse. The probes are of a simple construction: a short length of extruded, copper, coaxial cable, (characteristic impedance 50 ohms), which is coated with alumina and immersed in the plasma. The details are shown in Fig.5.1.

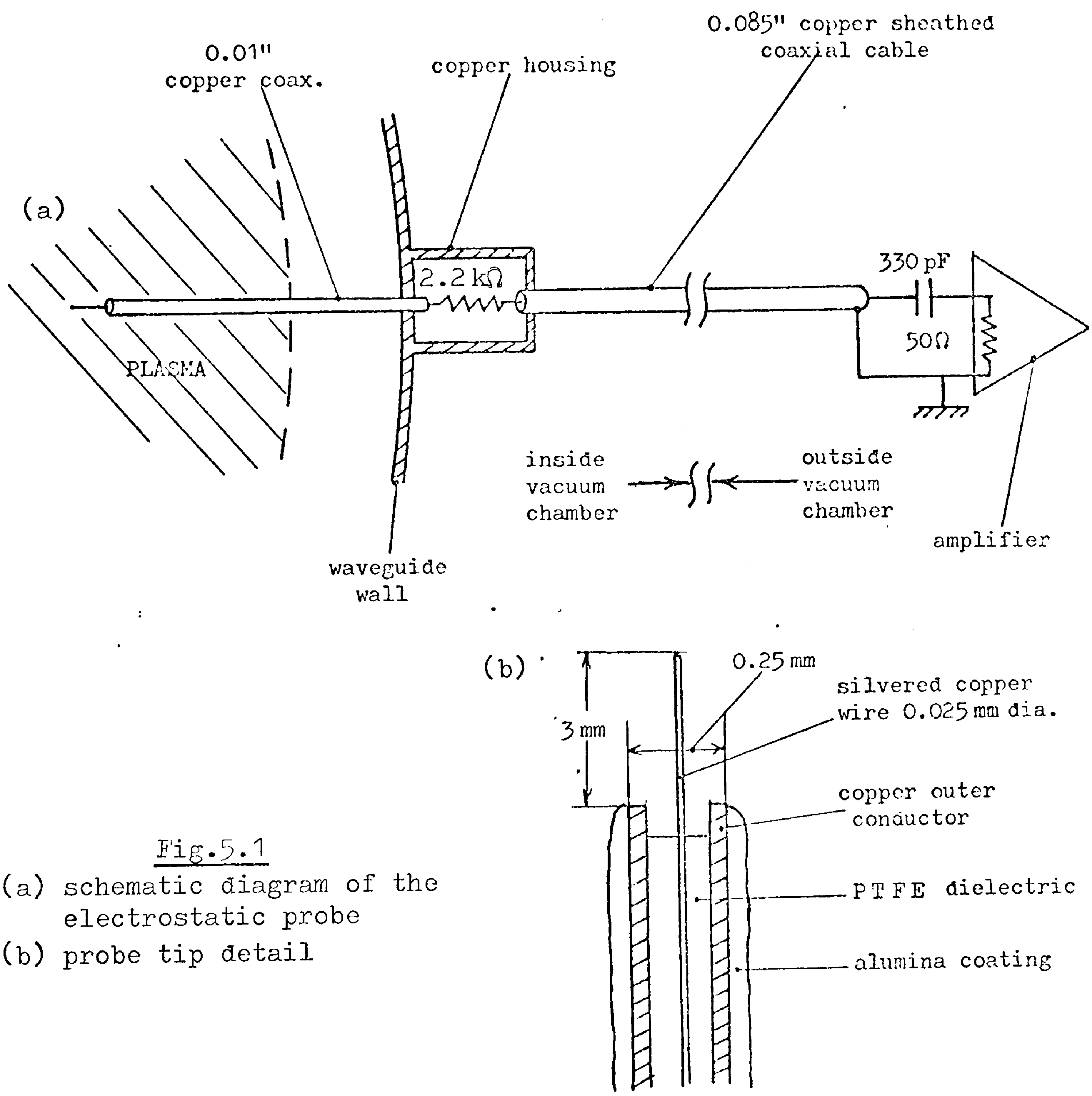

Fig.5.1
(a) schematic diagram of the electrostatic probe
(b) probe tip detail

Interpretation of the results from such a device is fraught with difficulties. However there are two advantages: simplicity and spatial resolution. Moreover other more sophisticated techniques which might be used to detect and measure density fluctuations, (e.g. laser scattering, microwave scattering, optical techniques, etc.) are unsuited to plasmas of these low densities ($< 10^{10}$ cm^{-3}).

We begin with a discussion of the information required from measurements of the potential fluctuations and then consider the problems associated with electrostatic probes in relation to these requirements.

5.2 FLUCTUATION MEASUREMENTS

Figure 5.2 shows typical oscilloscope photographs of the potential fluctuations in the frequency range 1-20 MHz detected by a single probe when $I > I_c$, i.e. the plasma has become resistive.

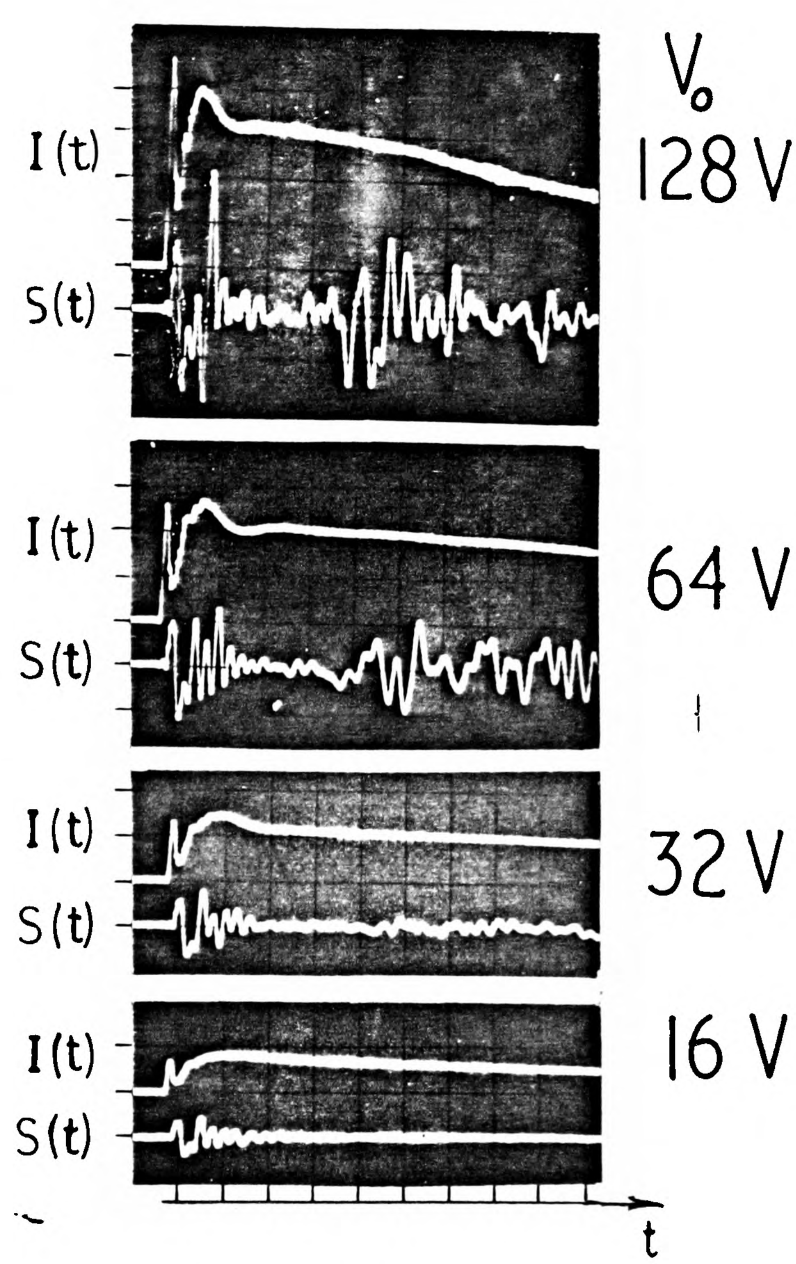

Fig.5.2
Single-shot oscilloscope photographs of the current I(t), and the signal S(t), detected by an electrostatic probe for different values of V_0 at 1 μs, demonstrating the onset of potential fluctuations. I scale: 400 mA div^{-1}; S scale (i.e. amplitude at the probe tip): 50 mV div^{-1}; t scale: 0.2 μs div^{-1}. (The initial spike on the I(t) trace corresponds to the charging of a stray capacitance in the external circuit.)

An example of a typical pair of photographs of fluctuations detected by two probes, closely spaced, during the <u>same</u> current pulse is shown in Fig.5.5.

We might ask the question: what information do we require from such data ? From the discussion in Chapter I, it follows that there are three qualities that characterise the fluctuation spectrum.

(a) The frequency spectrum or associated correlation times.

(b) The wave-vector spectrum or associated correlation lengths.

(c) The energy of the fluctuations (i.e. the absolute amplitude). Associated with this consideration is the quality of the fluctuations, e.g. are we detecting potential fluctuations or density fluctuations and are the two related ?

Qualities (a) and (b) raise the question: are the ω-spectrum and the k-spectrum related by a dispersion relation ? Let us consider their measurement in more detail.

5.2.1 Frequency Spectrum

For low frequencies with periods the same order as the duration of the current pulse, there is the conceptual problem of describing transient oscillations in terms of a frequency spectrum; yet we are particularly interested in this frequency range, since it is most likely that the ion dynamics are involved.

One possible analysis of the data is to Fourier-analyse numerically the traces of many photographs from single pulses, (bearing in mind the limitations at low frequencies) and determine the statistical trend for an ensemble of pulses; a time-consuming process which has been carried out for a toroidal experiment by HAMBERGER and JANCARIK (1972), (see Chapter VI). However in this experiment we can take advantage of the high rate of repetition of the pulses and devise an electronic sampling technique to detect the statistical trends of an ensemble which also avoids the conceptual problem connected with the Fourier analysis of transient oscillations.

We define the parameter $A(t_o, \tau)$, as the <u>ensemble average of the instantaneous auto-correlation</u>. This parameter describes how the instantaneous potential at time t_o, is correlated to the instantaneous potential at time $(t_o - \tau)$. Unlike Fourier analysis at low frequencies, it is meaningful to consider how this parameter evolves with time t_o. Thus during each pulse (i.e. experiment), the fluctuating potential detected by a single probe is

$$S(t_o) = S_o(t_o) + \tilde{S}(t_o) \qquad \ldots (5.1)$$

where $t_o = 0$ is the start of the pulse and,

$$\begin{aligned} \langle S(t_o) \rangle &= S_o(t_o) \\ \langle \tilde{S}(t_o) \rangle &= 0 \end{aligned} \qquad \ldots (5.2)$$

We define the function $A(t_o, \tau)$, as the normalised ensemble average of the instantaneous auto-correlation, viz:

$$A(t_o, \tau) = \frac{\langle \tilde{S}(t_o) \,.\, \tilde{S}(t_o - \tau) \rangle}{\langle \tilde{S}(t_o)^2 \rangle} \qquad \ldots (5.3)$$

The $\langle \; \rangle$ brackets imply an ensemble average taken from many pulses. Note that in the definition (5.2) we have subtracted the reproducible part of $S(t_o)$ so that $A(t_o, \tau)$ applies only to the random part of the fluctuating potential $\tilde{S}(t_o)$.

$A(t_o, \tau)$ cannot provide a complete statistical description for the ensemble of $S(t_o)$ since the averaging introduces an ambiguity. If the measured values of $A(t_o, \tau)$ indicate a short auto-correlation time, then this result has two possible interpretations. Either there are relatively coherent fluctuations during each pulse whose fluctuation frequency changes substantially from pulse to pulse, or the fluctuations in each pulse have short correlation times. This ambiguity is demonstrated in Fig.5.3.

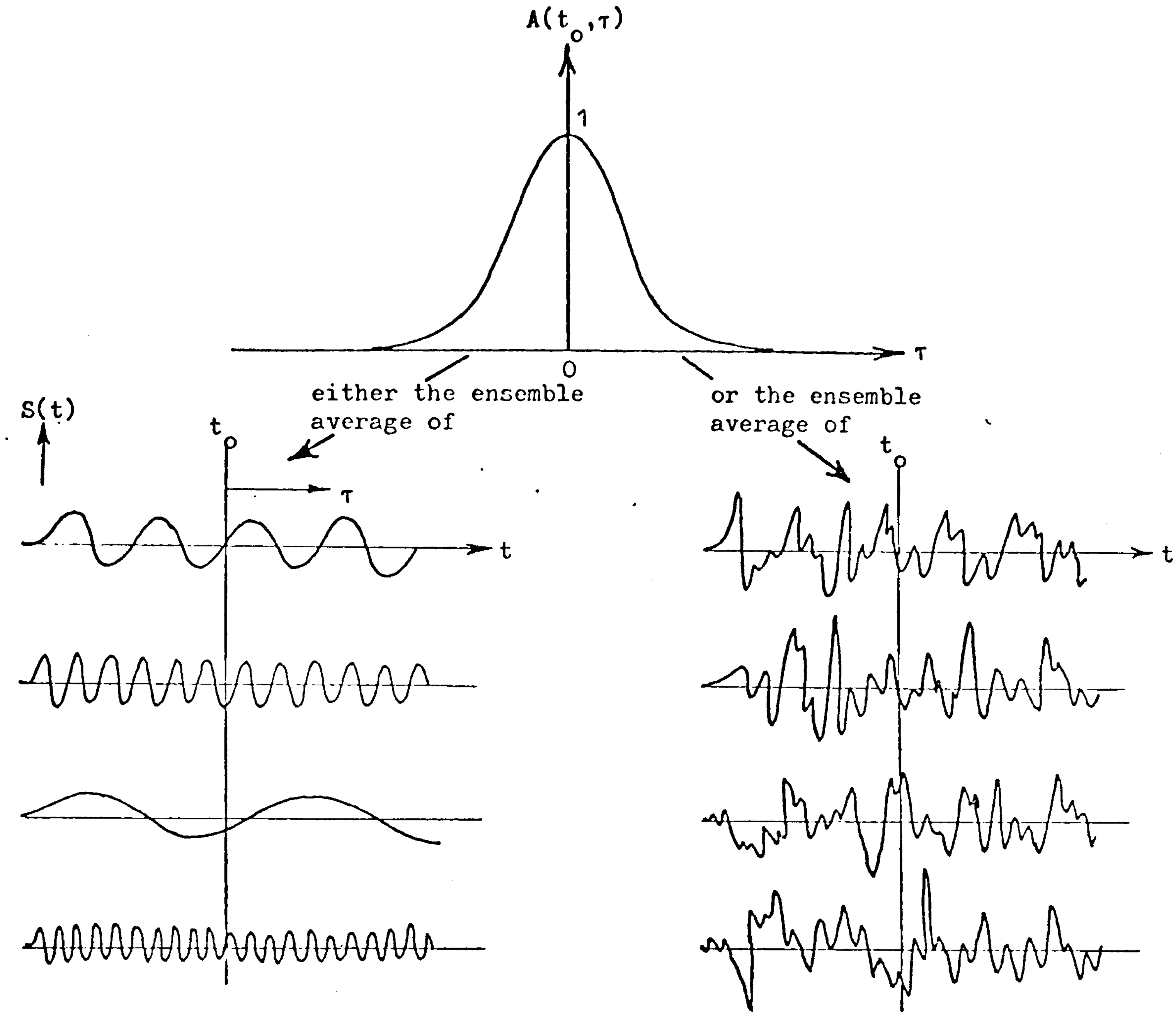

Fig.5.3
Two possible ensembles for a gaussian $A(\tau)$

A further problem connected with this ambiguity, is that if the fluctuation spectrum is broadband it is necessary to use filters in order to split it up into manageable parts,(e.g. to separate the high frequencies from the low frequencies). Then the frequency response of the filter will be folded into $A(t_o, \tau)$.

The experimental technique of measuring $A(t_o, \tau)$ for the low frequency fluctuations is described in section 5.3. At high frequencies these problems do not arise in the experiment, and it is possible to determine the ω-spectrum using an electronic spectrum analyser,(see section 5.4).

5.2.2 Wave-Vector Spectrum

Similar considerations apply to measurement of the $\underline{k}$-spectrum which requires comparing the fluctuation signals $\tilde{S}_1$ and $\tilde{S}_2$ detected by two probes separated by the vector $\underline{\xi}$. By analogy with $A(t_o, \tau)$ we define $C(t_o, \underline{\xi})$, the normalised ensemble average of the instantaneous two-probe cross-correlation:

$$C(t_o, \underline{\xi}) = \frac{\langle \tilde{S}_1(t_o, \underline{x}_o) \cdot \tilde{S}_2(t_o, \underline{x}_o - \underline{\xi}) \rangle}{\langle \tilde{S}_1(t_o, \underline{x}_o) \cdot \tilde{S}_2(t_o, \underline{x}_o) \rangle} \qquad \ldots (5.4)$$

In general both $A(\tau)$ and $C(\underline{\xi})$ are functions of both time t_o, and position $\underline{x}_o$.

5.3 PRACTICAL PROBLEMS ENCOUNTERED WITH ELECTROSTATIC PROBES

In the low density, low temperature plasma used in this experiment there are two serious practical problems.

5.3.1 Frequency Response and Absolute Amplitude Calibration

This involves the input impedance of the probe as seen by the plasma. The coupling of high frequency signals (i.e. $\omega \geqslant \omega_{pi}$), between plasma and probe is not understood in these low temperature, low density plasmas with strong magnetic field. Experimentally it seems that the probe detects displacement currents because altering the d.c. potential between probe and plasma has no effect on the received signal. If we assume that the coupling is capacitive where the capacitor C, is the probe sheath, (i.e. thickness $\sim \lambda_D$, area $\sim$ probe area and dielectric constant ~ 1), then for typical experimental conditions, $C < 10^{-13}$ F. The coaxial cable connecting the probe to the amplifier outside the vacuum chamber must be terminated with its characteristic impedance of 50 Ohms in order to eliminate reflections. On this basis the detection circuit is a high pass filter, see Fig.5.4.

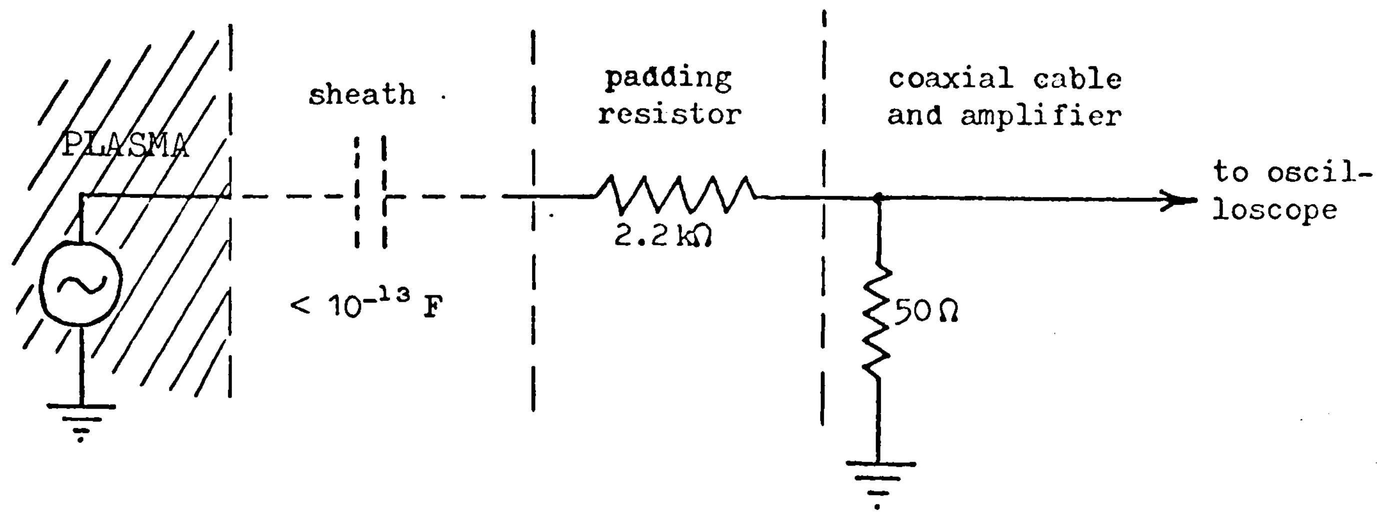

Low-cut frequency = $\frac{1}{2\pi RC}$ > 1 GHz

Fig.5.4

Model circuit for electrostatic probe

In practice this very weak plasma-probe coupling is a problem which is difficult to overcome. One possible solution is to use a high-impedance buffer amplifier situated very close to the probe. The input capacitance of the probe could also be reduced by having a double coaxial shield with the inner shield bootstrapped to the input signal, technically a difficult problem at high frequencies. In the present work, padding resistors (2.2 kΩ) were used to increase the impedance as shown in Fig.5.4, but these are not very satisfactory since the sensitivity is correspondingly reduced.

The consequences of this problem are twofold. Firstly the absolute amplitude and the frequency response are unknown, although they can be estimated with great uncertainty from the simple model suggested by Fig.5.4. Secondly, if the sheath thickness λ_D, is changing due to an increasing electron temperature, the frequency response will be changing with time, making it impossible to measure growth rates directly.

5.3.2 Local Disturbance of the Plasma

The probes and their electrostatic shields will disturb the plasma, influencing results for wavelengths which are the order of, or much less than the probe dimensions. In particular, a Fourier component of the spatial disturbance could provide an initial amplitude, for a growing wave, which is greatly enhanced above the level it would otherwise be in a quiescent plasma.

With these problems in mind we now discuss the results obtained from electrostatic probes.

5.4 LOW FREQUENCY FLUCTUATIONS, 3 - 20 MHz

The frequency range is to some extent arbitrarily defined by the available filters. The lowest frequency is determined by the 330 pF decoupling capacitor, (see Fig.5.1). Frequencies in this range are more likely to be the main source of ν_{eff} since the electron distribution function can only lose momentum by interacting with the ions. From Fig. 5.2 it can be seen that the fluctuations appear to start after 1 μs. It is difficult to draw any conclusions about growth rates since we know from the measurements in Chapter IV that the electron 'temperature' is rising during this time and the plasma probe coupling may be decreasing.

Oscilloscope photographs of single pulses were taken of fluctuations during the period $t_o = 1$ to 3 μs and then digitally Fourier-analysed by computer. Fig.5.5 shows a typical result for fluctuations detected by two probes within 0.5mm of each other during the same current pulse. Although there is some sort of structure, the frequency spectrum during a single pulse is quite broad. This structure varies from pulse-to-pulse and there seems to be very little or no correlation between signals from two probes close to each other.

The electronic circuit for measuring $A(t_o, \tau)$ is shown in Fig.5.6. The received signal is split into two channels which are fed into separate sampling units. The sampling units are triggered by a pulse from the main voltage pulse generator. One sampling unit samples the instantaneous voltage at a fixed time t_o, the other unit samples at a time $t_o - \tau$, which is slowly swept (about 1 μs per 3 min.), from $\tau = 0.25$ μs to $\tau = -0.25$ μs.

The outputs from the sampling units are low frequency pulses whose duration is the repetition time for the current pulses and whose amplitude

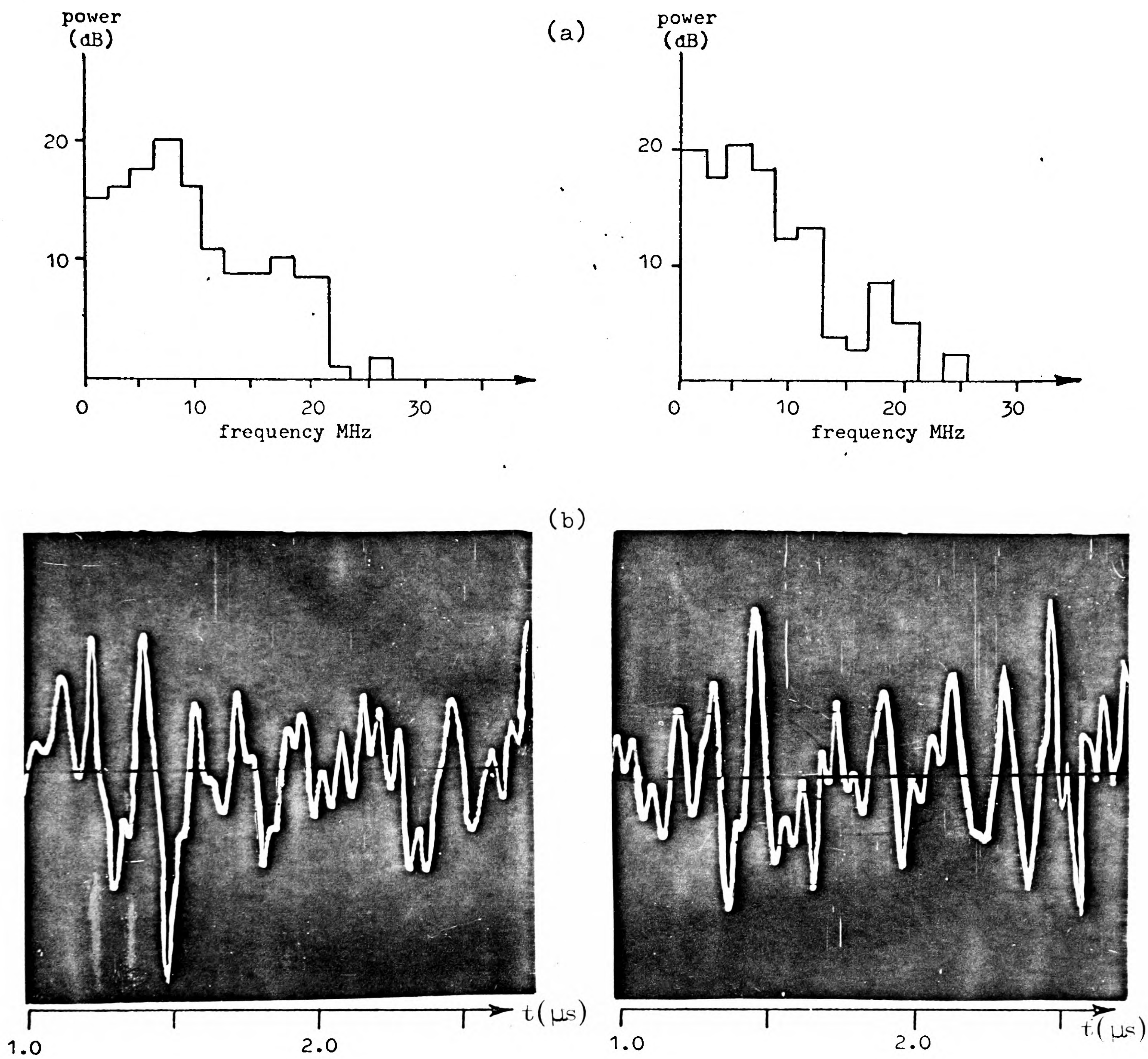

Fig.5.5

(a) A typical example of the computed low frequency power spectra;
(b) The corresponding potential fluctuations detected by two probes (separation $\simeq$ 0.5 mm) during the same current pulse;
$n_o = 8 \times 10^9$ cm^{-3} , $V_o = 40$ V

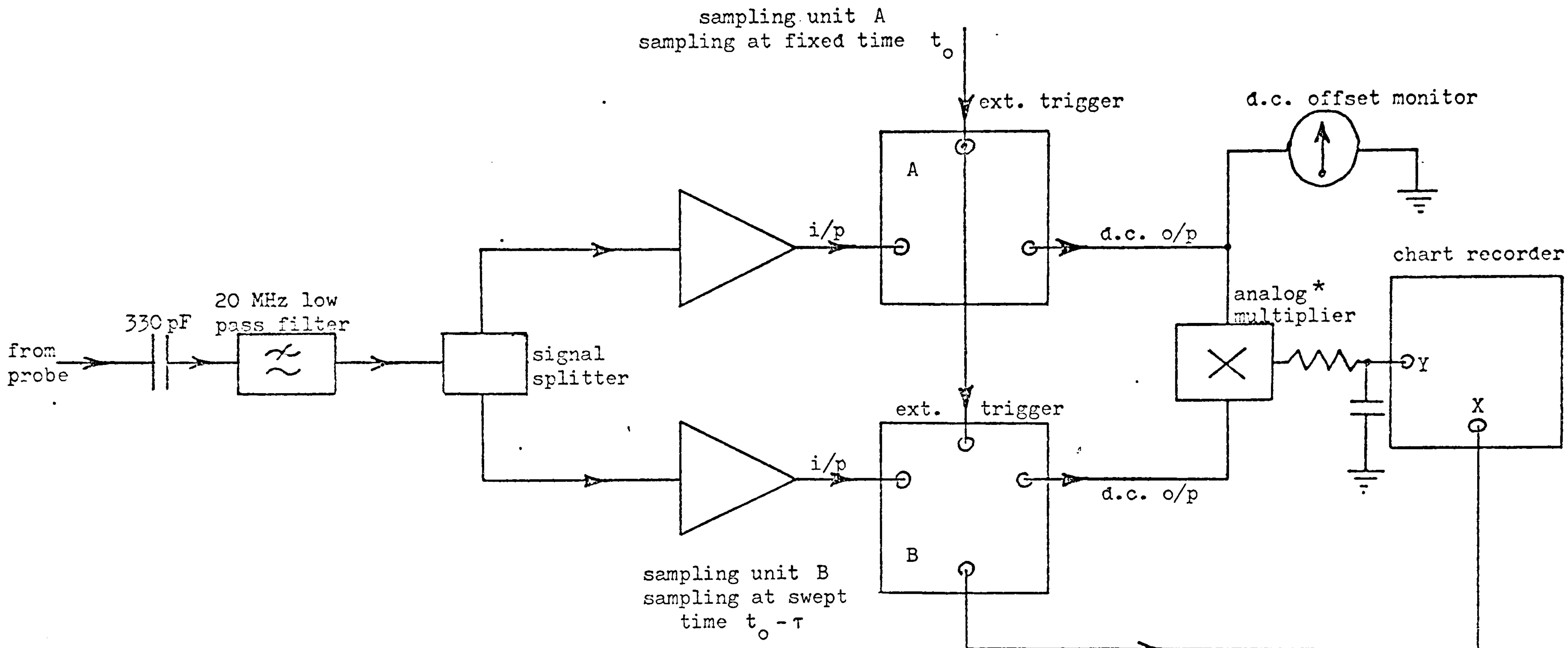

*RCA type CA 3091D

Fig.5.6
Circuit for the measurement of $A(t_o, \tau)$

is the instantaneous voltage sampled during each pulse. These two outputs are electronically multiplied by a four-quadrant analogue multiplier and then integrated over a time of about 1 sec. In this way we can measure $A(t_0, \tau)$ from an average over an ensemble of about 50,000 pulses in 100 sec. In order to ensure that $A(t_0, \tau)$ relates to the random part of $S(t_0)$ it is necessary to adjust the d.c. offset of the fixed-time sampling unit so that the average output is zero, i.e. from channel A, the d.c. output for each sample

$$= S(t_0) - S_0(t_0) = \tilde{S}(t_0)$$

where the d.c. offset has been adjusted to $S_0(t_0)$. From channel B, the d.c. output for each sample

$$= S_0(t_0-\tau) + \tilde{S}(t_0-\tau) \ .$$

Thus the time-averaged output from the multiplier

$$= \langle \tilde{S}(t_0) [S_0(t_0-\tau) + \tilde{S}(t_0-\tau)] \rangle$$

$$= \langle \tilde{S}(t_0) \, . \, \tilde{S}(t_0-\tau) \rangle \ .$$

A typical result is shown in Fig.5.7 along with the corresponding conditional probability plots; (i.e. the probability of $\tilde{S}(t_0)$ and $\tilde{S}(t_0-\tau)$ taking values in the range $[y, y+dy]$ and $[x, x+dx]$ respectively, is proportional to the density of spots). These are obtained by applying one sampling unit output to the horizontal deflection plates of a sampling oscilloscope and the other to the vertical deflection plates, so that each spot represents one pulse and its coordinates are $\tilde{S}(t_0)$ and $\tilde{S}(t_0-\tau)$ for that particular pulse. Such photographs enable us to determine qualitatively at a glance how well two instantaneous voltages are correlated over many current pulses.

Using this technique, $A(t_0, \tau)$ was measured over a wide range of densities and currents for $0.5 \leq t_0 \leq 2.0$ µs. There was little or no variation in the shape of $A(t_0, \tau)$ from that shown in Fig.5.7. This, in

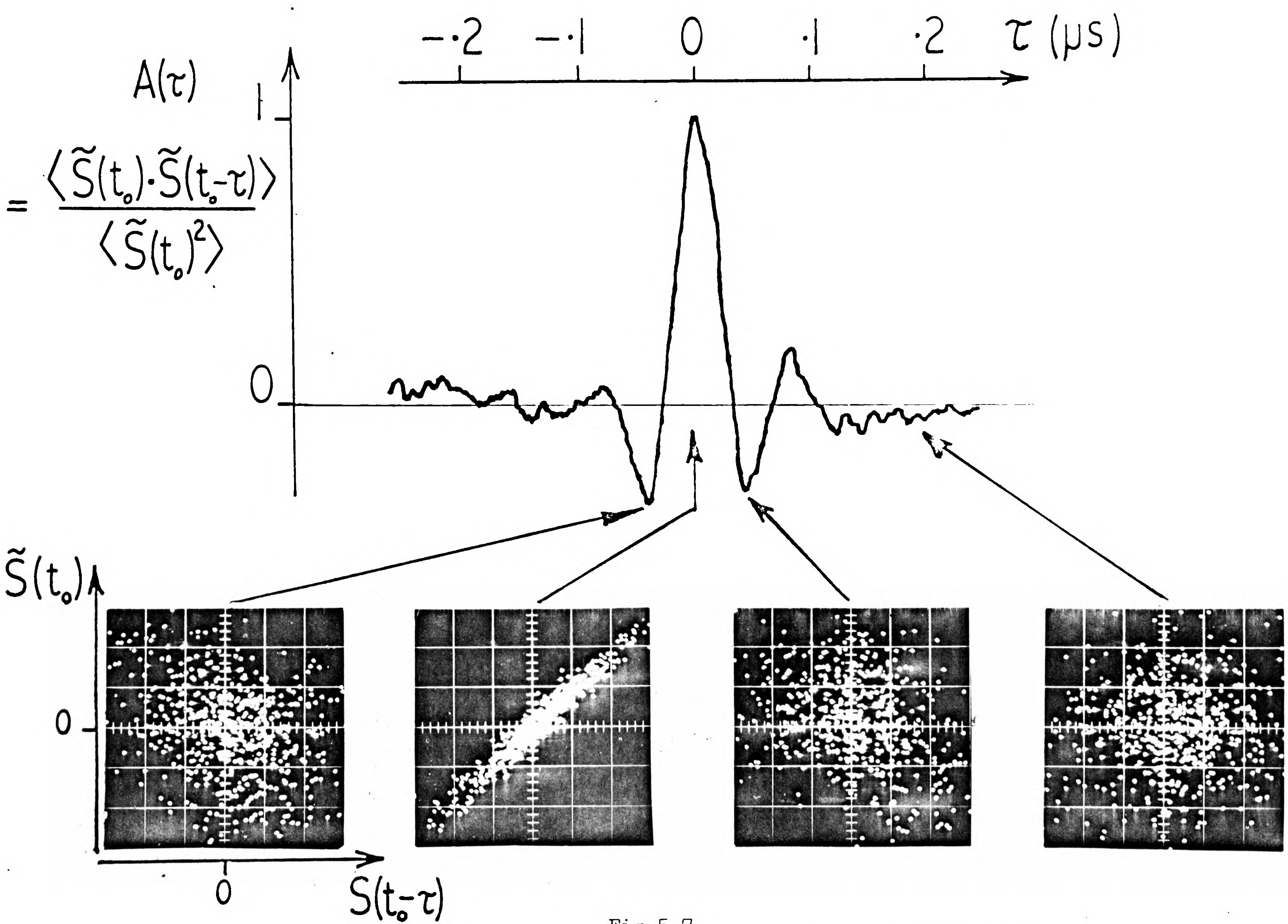

Fig.5.7
A typical ensemble average of the instantaneous auto-correlation
(t_o = 1.4 μs , n = 4 x 10^9 , v_d = 10^8 cm s^{-1})

conjunction with a few single pulse photographs, implied that no prominent coherent oscillations could be detected in the low frequency fluctuations. The form of $A(t_o, \tau)$ seems to be determined mainly by the frequency response of the filter; (e.g. white noise transmitted by an ideal low pass filter cutting off at a frequency $= \omega_o/2\pi$ would produce $A(\tau) \propto \frac{\sin \omega_o \tau}{\omega_o \tau}$). Altering the filter or removing it altogether produced results consistent with this conclusion.

$C(t_o, \underline{\xi})$ was measured in a similar manner by sampling the signals from two probes at time t_o, with two sampling units and slowly separating the probes. Fig.5.8 shows the conditional probability plot of $C(t_o)$ for $|\underline{\xi}| = 0.5$ mm, the closest possible separation.

Generally $C(t_o, \underline{\xi})$ is very close to zero. Moreover, there is no perceivable variation of $C(t_o, \underline{\xi})$ with $\underline{\xi}$ for $|\underline{\xi}| > 0.5$ mm. This result was found over a wide range of densities and currents.

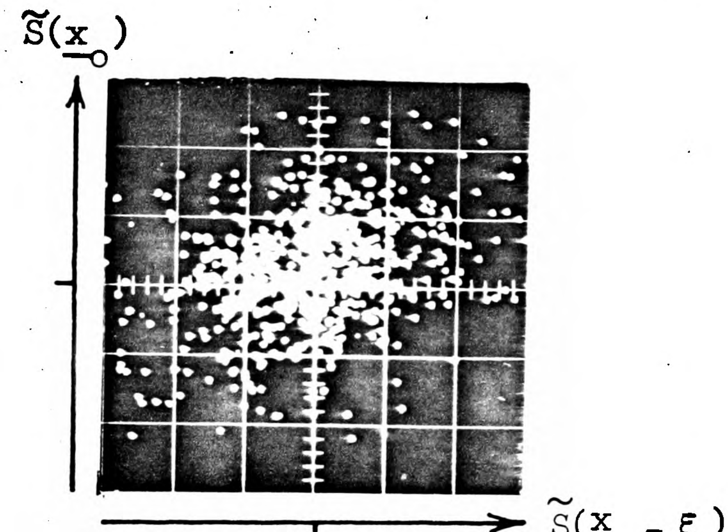

Fig.5.8
A typical conditional probability plot of $C(t_o, \xi)$
($\underline{\xi}$ (z-direction) $\simeq 0.5$ mm, $t_o = 1\,\mu$s)

In conclusion it would appear that for $t_o > 0.5\ \mu$s the low frequency fluctuations are incoherent and not spatially correlated for $|\underline{\xi}| > 0.5$ mm. It was not possible to measure $A(\tau)$ and $C(\underline{\xi})$ during the early stages because the detected signals were dominated by the reproducible ringing signal discussed in Chapter III, (see Fig.3.12).

5.5 THE HIGH FREQUENCY FLUCTUATIONS, > 50 MHz

High frequency fluctuations will not involve the ion dynamics and so cannot cause the electrons to lose momentum to the ions, although they might redistribute momentum within the electron distribution function itself.

For these frequencies it is possible to gate the detected signal with a 'window' 0.2 μs wide and apply this signal to an electronic spectrum analyser. The gating is achieved by using a balanced mixer as a switch which is operated by the second pulse generator, as shown in Fig.5.9, (cf. the trigger arrangement in Fig.4.3(b)).

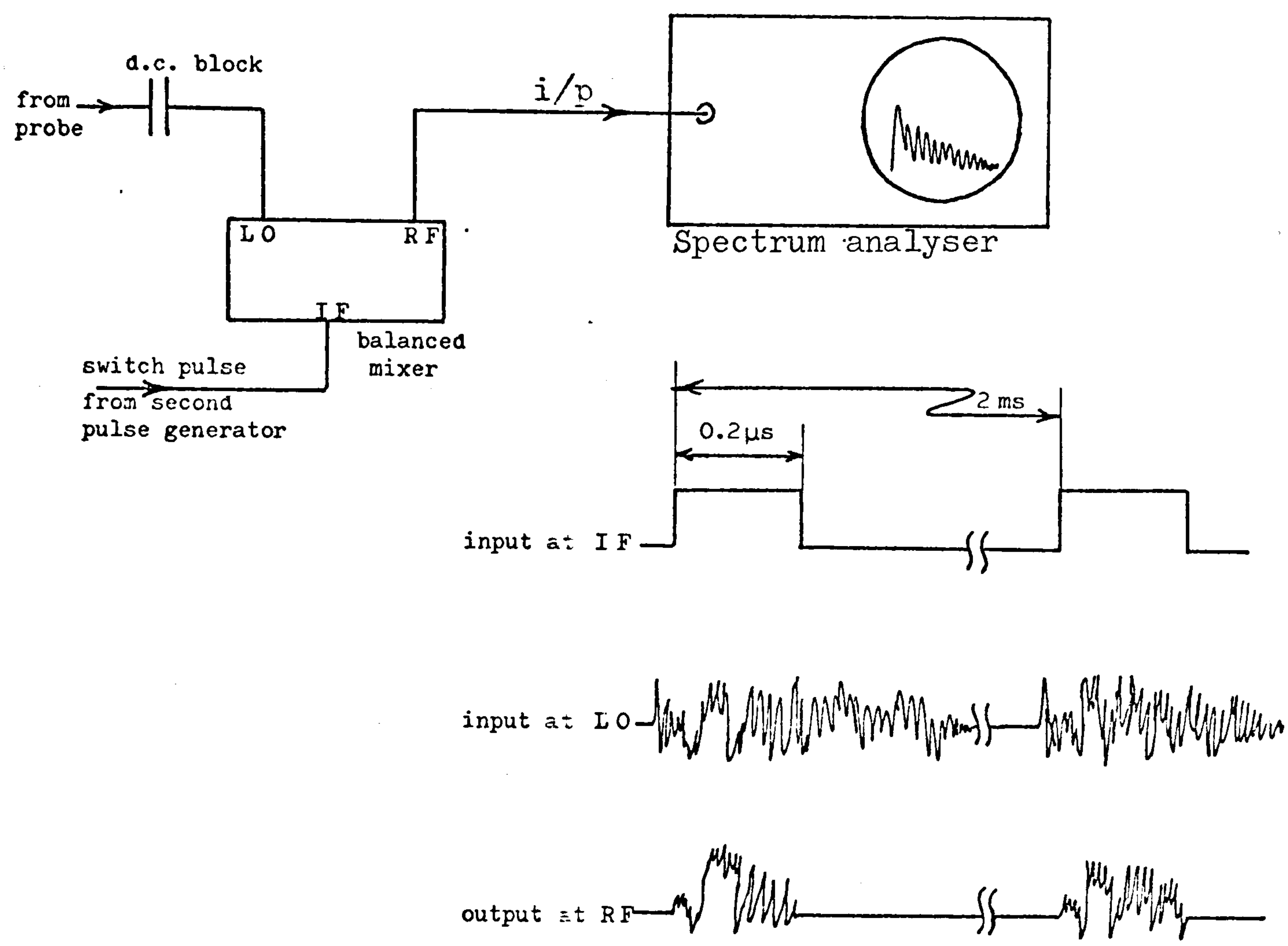

Fig.5.9
Circuit for high frequency spectrum analysis

The spectrum analyser records the frequency spectrum of the r.f. output from the mixer, thus the gate width and repetition rate are folded into the result. Provided the local oscillator of the spectrum analyser is swept sufficiently slowly and the video filter has been removed, a gate width of 0.2 μs and a repetition rate of 500 Hz has a negligible effect when sweeping from 50 to 1000 MHz, (see Appendix A.5 for a discussion of the details). By varying the delay of the switch pulse it is possible to achieve a coarse time resolution for the frequency spectrum. Fig.5.10 shows a typical result.

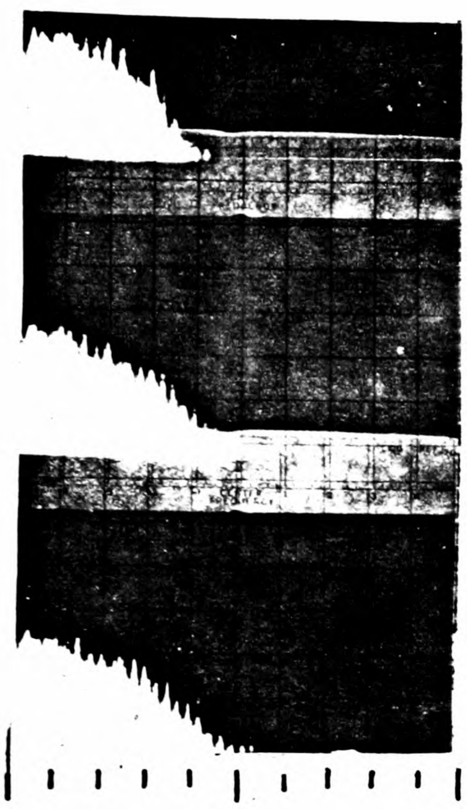

Fig.5.10
A typical example of the ensemble average high frequency spectrum, $f(\omega)$, as detected by a gated spectrum analyser; $\omega_{pe}/2\pi$ = 500 MHz, V_0 = 100 V, vertical scale is a logarithmic power scale: 10 dB div^{-1} (max. amplitude ~ -50 dBm into 50 Ω)

As pointed out in section 5.2 we cannot deduce the true frequency spectrum of the oscillations because we do not know the probe frequency response. However two observations can be made; firstly the ensemble average of the fluctuation spectrum is wideband with frequencies $\omega \leq \omega_{pe}$, and secondly there are peaks in the spectrum at intervals of about 20 MHz.

It was possible to measure $C(t_0, \underline{\xi})$ (where $\underline{\xi}$ is in the axial z-direction), for these peak frequencies by filtering them through narrow band filters and then correlating the signals from two probes by the technique described above. (The effect of the filters was carefully checked to ensure that the results were not spurious.) Fig.5.11 shows a typical result for a few of the peaks. The wavelengths of these waves are consistent with the dispersion of externally excited plasma waves measured in Chapter IV, and appear to be resonances due to reflections at the column end plates.

5.6 CONCLUSION

Because of the difficulties discussed in the first two sections, the measurements of the potential fluctuations reported in this chapter are not very precise. As a summary we list the conclusions that can be drawn from these results in contrast with the measurements that have not been made.

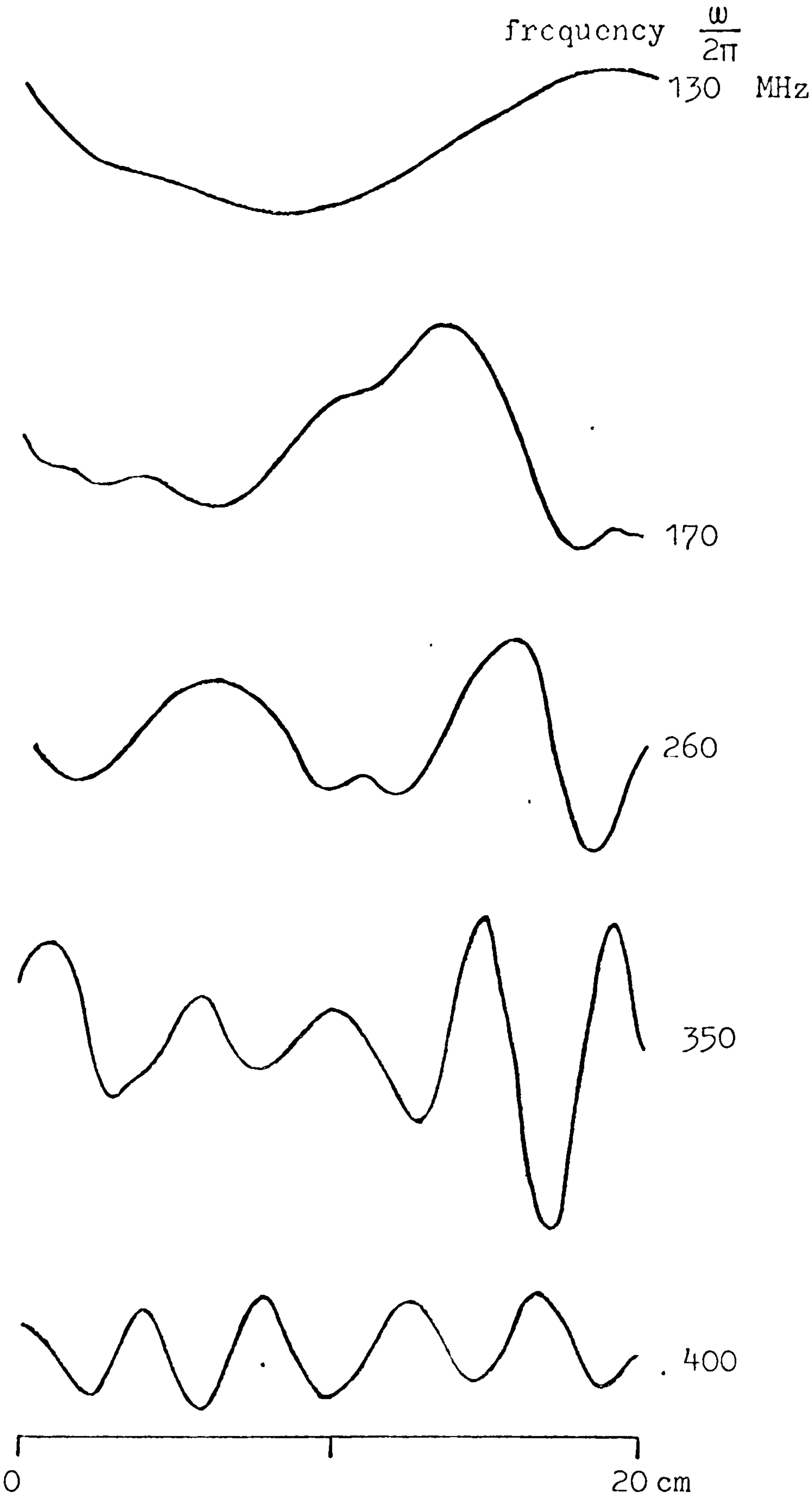

Fig.5.11

A typical example of interferometer traces (i.e. $C(t_o,z)\Big|_{\omega}^{\omega+\Delta\omega}$) for the electron plasma waves which exist in the turbulent plasma at frequencies corresponding to the peaks observed in $f(\omega)$ (see Fig.5.10); $t_o \approx 1\ \mu s$

(a) Enhanced potential fluctuations arise when the plasma is resistive and increase in magnitude with increasing current (see Fig.5.2). However the frequencies, growth rates and wavelengths of the unstable oscillations have not been measured in the early stages, so the initial instability has not been positively identified as the electron-ion two-stream instability.

(b) Although an ω or $\underline{k}$ power spectrum for the fluctuations has not been definitely measured, it seems that the high frequency fluctuations consist of a broad band of long wavelength coherent electron plasma waves with a well-defined dispersion relation, whereas the low frequency fluctuations are incoherent oscillations, uncorrelated over scalelengths ≥ 0.5 mm.

(c) Although the absolute amplitudes of the potential fluctuations are not known, there are two pieces of circumstantial evidence both of which suggest amplitudes $\sim$ tens of volts. Firstly, estimates of the plasma-probe coupling from the simple model in Fig.5.4 suggest an attenuation of ~ 40 dB at 10 MHz. For signals $\tilde{\sim}$ 100 mV (see Fig.5.2) this implies fluctuation amplitudes ~ 10 V. Secondly, the amplitude of the ringing signal should be related to the potential applied to the end plate, (see Chapter III). This suggests an attenuation of ~ 45 dB at 20 MHz (see Fig.3.12).

CHAPTER VI

CONCLUSION

In this chapter there is a brief review of other work reported in the literature relevant to this experiment. This is followed by a summary of the aims and achievements of the present work, from which future possible topics for research are discussed.

6.1 TURBULENT HEATING EXPERIMENTS

As pointed out in Chapter I, the primary purpose of many turbulent heating experiments has been to investigate the application of turbulent heating to controlled thermonuclear fusion devices, in contrast to this work which is intended to be an investigation into the physics of strong electrostatic plasma turbulence. Consequently a direct comparison of the results of this work with many of those obtained from turbulent heating experiments is not always possible. In particular, most turbulent heating experiments are conducted at higher plasma densities, ($10^{11} - 10^{14}$ cm^{-3}), and generally have confinement times long enough to allow processes with very long time scales, (i.e. very many ion plasma periods), to become important: there is considerable interest in the long timescale ion heating by the turbulent fluctuations. Many turbulent heating experiments have operated under conditions where the plasma cannot be unstable to the electron-ion two-stream instability, but is unstable to the ion acoustic instability, i.e. $c_s \ll v_d < v_e$ (see Chapter II). In the present experiment $T_i \simeq T_e$ before the heating pulse is applied, so that the ion acoustic instability cannot occur in the early stages. During the later stages, although we may have $T_e \gg T_i$, the duration of the experiment ($\sim 2\,\mu s$) is too short to observe the results of the slower growing ion acoustic instability (see Fig.2.4), assuming that it can occur in an already strongly turbulent plasma. We mention here results from three pulsed experiments which are particularly relevant to this work.

Firstly, at Jutphaas in Holland an anomalous conductivity which, in the early stages, is consistent with the scaling (1.12) found by Hamberger and Friedman (op. cit.), has been observed in a turbulently heated mirror machine experiment. Unfortunately precise measurements of σ and a detailed interpretation of the results are complicated by an increase in plasma volume due to ionization in the early stages of the heating pulse, (see De KLUIVER et al. (1971) and SCHRIJVER et al. (1974)). Secondly, at Cornell in the USA similar observations have been made by ROBERTSON et al. (1973) who also observed a critical current for the onset of anomalous conductivity, (but no scaling of this with density). Again no precise measurements of σ during the early stages of the heating pulse were possible.

Finally there is the work by Hamberger et al. in a toroidal turbulent heating experiment at Culham Laboratory, which partly stimulated the work reported here. In addition to the conductivity scaling found at high fields ($E_o > E_c$), which has been used for comparison in Chapters III and IV, there are data on the potential fluctuations detected in the plasma by a balanced, electrostatic, double probe. The frequency spectra of these fluctuations during a single heating pulse have been computed from oscilloscope photographs by HAMBERGER and JANCARIK (1972). Under conditions where the electron-ion two-stream instability was expected to occur, peaks were observed at frequencies around $\frac{1}{2}\omega^*$, (see equation (2.3)); similar observations have been reported by Schrijver et al. (op. cit.). This result is to be compared with the rather broad-band of low frequency oscillations reported in Chapter V.

The electron thermal energy in the toroidal experiment was deduced indirectly both from the electrical dissipation (assuming energy is conserved), and from the X-ray emission spectra from a solid carbon target immersed in the plasma. The implication of these results was that v_e

rapidly exceeded v_d as shown in Fig.6.1,(from HAMBERGER et al. (1975)). This behaviour is in agreement with that deduced from the dispersion of electron plasma waves in this experiment, as reported in Chapter IV (cf. Figs.4.9 and 4.11).

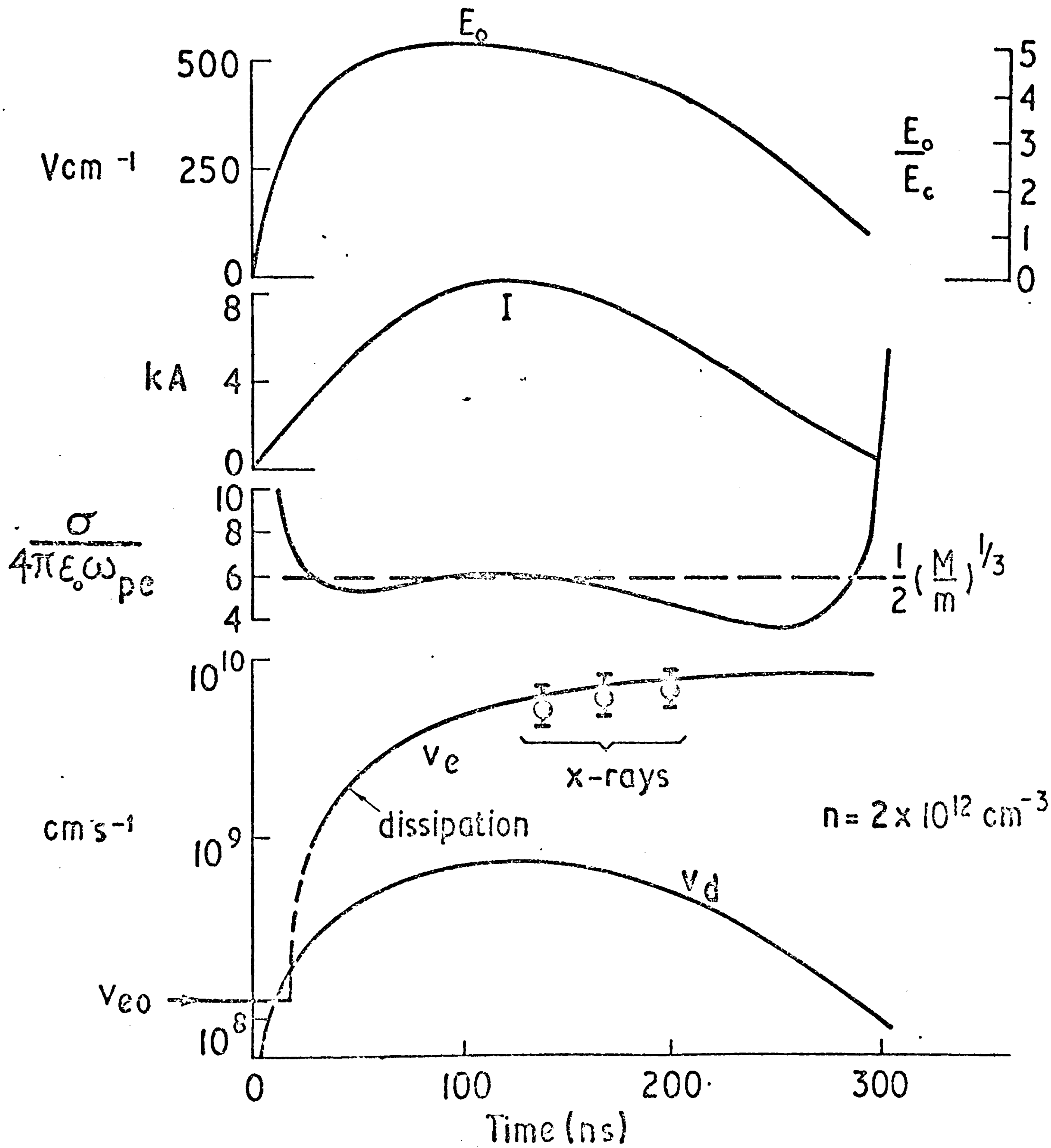

Fig.6.1

The behaviour of the electrical parameters, E_o, I and σ, and the deduced behaviour of v_d and v_e in the toroidal experiment, TWIST, (after Hamberger et al. 1975)

6.2 COMPUTER SIMULATIONS

One type of 'experiment' whose results can be directly compared with this work, is the computer simulation. In computer simulations of the two-stream instability, the individual trajectories of a large number of particles ($10^4 - 10^5$) are determined in phase space for short time-steps, by solving numerically for the self-consistent fields after each step, and using this solution to determine the trajectories during the next time-step. It is possible to follow the evolution of the plasma for many plasma periods, although computer resources usually restrict the simulation to 1-D or 2-D plasmas and purely electrostatic, self-consistent fields.

Various simulations of the current-driven two-stream instability have been reported in the literature, (BORIS et al. (1970); MORSE and NIELSON (1971); BISKAMP and CHODURA (1971); NISHIHARA and HASEGAWA (1972); WESSON et al. (1973), and HAMBERGER et al. (1975)). These have been carried out under various conditions, (e.g. constant driving field or constant current, different ion masses and different T_e/T_i ratios), but we only consider results from those with a constant driving field and $T_e = T_i$ at $t = 0$. (Unlike the turbulent heating experiments, in the present experiment the inductance of the external circuit is very small compared to the effective inductance due to the electron inertia, so that the plasma current is not determined by the external circuit.)

Figure 6.2 shows a typical example of the results obtained from a 1-D hydrogen plasma simulation by Morse and Nielsen (op. cit.) for a constant driving field, $E_o/E_c \simeq 1$. As can be seen in Fig.6.2(a), v_d does not become constant, but increases on average at about half the free acceleration rate, while v_e increases at about the same rate so that $v_d \leqslant v_e$. This result is consistent with an attractive physical picture. Initially the electrons freely accelerate until the plasma is unstable ($v_d > 1.3\ v_{eo}$).

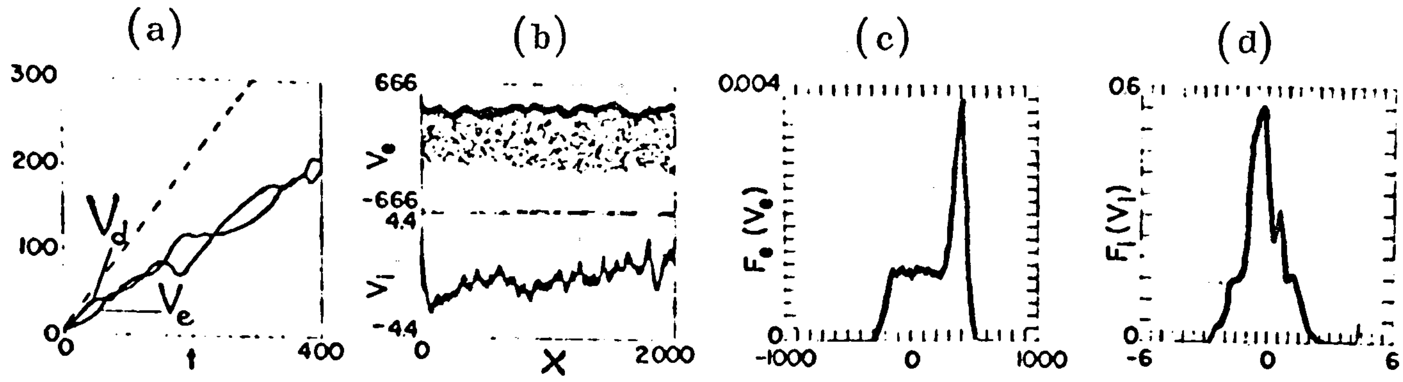

Fig.6.2

Results obtained from a 1-D computer simulation of a hydrogen plasma subject to a constant field $E_0 = 1.1\ E_c$, where $T_e = T_i$ at $t = 0$ (Morse and Nielson, 1971)

(a) Evolution of v_d and v_e, (the dotted line corresponds to free-electron acceleration)

(b) Phase-space (x,v), plots of the electron and ion distribution functions at $t = 400$

(c) Corresponding space-averaged $F_e(v)$

(d) Corresponding space-averaged $F_i(v)$

(Velocity scales: units of $\frac{1}{2\pi}\sqrt{\frac{KT_{i,e}}{m_{i,e}}}$; time-scale: units of $\frac{2\pi}{\omega_{pe}}$ length scale: units of λ_D)

During the nonlinear development of the instability, the electrons are 'heated' at the expense of losing some forward momentum, until $v_e > v_d$. The plasma now becomes stable, the fluctuations decrease rapidly allowing v_d to increase again until the plasma is unstable, so that the process can repeat itself, ad infinitum.

In general, 1-D and 2-D simulations with a constant driving field do not exhibit constant conductivity but predict a form of electron runaway combined with dissipation. The conductivity of the plasma increases linearly with time, so that the plasma presents an inductive load to the external driving field.

The deformation of $F_e(v)$ observed in the computer simulations (see Fig.6.2(c)), i.e. the scattering of the electrons in velocity space towards the ion drift, is qualitatively similar to the behaviour of $F_e(v)$ deduced from the dispersion of electron plasma waves in this experiment, (see Figs. 4.9 and 4.10). However the behaviour of v_d, v_e and ν_{eff} in the simulations is in sharp contrast with the results found in this work and that of Hamberger et al: following the initial transient, for which a heuristic explanation was given in Chapter IV, the results presented in Chapters III and IV indicate that v_d is axially uniform and remains steady, while v_e rapidly increases to values greater than v_d and the conductivity remains essentially constant. This contradiction is an unresolved mystery in this work since the experimental conditions in the Q-machine experiment, (strong uniform magnetic field, predominantly electrostatic fluctuations, etc.), would seem to be very close to the idealised plasma of the computer simulations when compared to the experimental conditions in many turbulent heating experiments.

It would seem that the computer simulations do not provide an adequate description of the physics in the experimental plasma. In particular, they may suffer from two limitations:

(a) The size of the physical space used in the calculations may be too small to include a sufficiently wide range of wavelengths for the collective modes. E.g. in the work by Morse and Nielsen (op. cit.), they consider a 1-D plasma which is initially 2000 Debye lengths in extent. Although this is treated as part of an infinite plasma by applying periodic boundary conditions, such a simulation cannot include modes with $k\lambda_D \leqslant 0.003$. In the course of the simulation as v_e increases, this extent reduces to effectively $\sim 60\ \lambda_D$ in 400 plasma periods, (see Fig.6.2), so by then modes with $k\lambda_D \leqslant 0.1$ cannot be included.

(b) The electrostatic nature of the simulations cannot include electromagnetic phenomena. It has been suggested that the resistivity in toroidal experiments might be explained by the electron current breaking up into filaments, (see HAMBERGER and SHARP (1973)). However, the scale-length perpendicular to the magnetic field for this electromagnetic process is $\sim c/\omega_{pe}$, which, in the present experiment, is an order of magnitude greater than the column radius.

6.3 THEORETICAL APPROACHES

At present, attempts to describe theoretically the nonlinear development of the electron-ion two-stream instability are very limited because of the difficulties outlined in Chapter I. We mention here three approaches in the literature specifically directed towards this instability.

As mentioned in Chapter II, electron trapping is a possible nonlinear saturation mechanism; indeed there is evidence of this happening in the early stages of some 1-D computer simulations. (As pointed out in Chapter II, because $\omega_{pi} \gg \omega_{ci}$ in this experiment, the unstable waves propagate over a wide range of angles to B_z. Particle trapping requires a well-defined monochromatic wave, so the experimental conditions may militate against this process.)

DRUMMOND et al. (1971) have attempted to describe the final state of the instability in terms of a large amplitude wave which traps nearly all of the electrons. By making assumptions about the different timescales of the wave and particle dynamics, they can use the BGK theory of large amplitude waves (BERNSTEIN, GREENE and KRUSKAL (1957) to calculate the particle distribution functions. They then compute the thermodynamic and stability properties of such a state. The results indicate that the level of collective fluctuations remains high ($\Gamma_1 \sim 1$) and the electrons are continually heated as long as the driving field is applied. The behaviour of the current depends on the distribution of untrapped electrons, which the theory cannot describe, (presumably this is determined in the early stages of the instability).

These general conclusions are consistent with the experimental observations but unfortunately the predictions of this 'big wave theory', (or 'big hand-waving theory' as it is known in some circles), are insufficiently precise to be checked.

SIZONENKO and STEPANOV (1971) adopt a different approach. As pointed out in Chapter II, when the electrons are undergoing steady acceleration, the characteristic growth rate of the two-stream instability is $\sim \omega_{pi}$ rather than $0.7\ \omega^*$ (q.v. (2.3)). They estimate the effects of the nonlinear particle dynamics at this lower growth rate, and claim that for $\omega_{ce} \gg \omega_{pe}$, the nonlinear components of electron and ion motions <u>parallel</u> to $\underline{B}$ cannot limit v_d. They require the nonlinear terms in the electron motion <u>perpendicular</u> to $\underline{B}$ to limit v_d. A consequence of this is that ν_{eff} depends on $\underline{B}$, viz:

$$\nu_{eff} \sim \omega_{pi} \left(\frac{\omega_{pe}}{\omega_{ce}}\right)^2 \qquad \text{for} \quad \omega_{pe} \ll \omega_{ce}$$

and

$$\nu_{eff} \sim \omega_{pi} \qquad \text{for} \quad \omega_{pe} \gtrsim \omega_{ce} .$$

This scaling contradicts the experimental observation that ν_{eff} is independent of B_z for $\omega_{ce} \gg \omega_{pe}$.

Finally there is the application of quasilinear theory to the problem by HAMASAKI et al. (1971). This work was stimulated by the results from the computer simulations and predicts a plasma behaviour in good agreement with them. Quasilinear theory is the lowest order stage in weak turbulence theory. Briefly, it determines the temporal evolution in velocity-space of the space-averaged particle distribution functions due to the broad spectrum of weak electrostatic fluctuations. HAMASAKI et al. state that,

> " Since the particle phase space in the simulation experiments acquires considerable spatial structure, it is indeed instructive that quasilinear theory which is inherently a space-averaged description, produces such good agreement."

Unfortunately since neither the theory or the computer simulations correspond to physical reality, the agreement is rather academic.

6.4 SUMMARY OF RESULTS AND OUTSTANDING PROBLEMS

The principal aims of this work can be summarized as :

(a) To demonstrate the existence, threshold and nature of current-driven electrostatic turbulence in a collisionless plasma with well-defined initial conditions.

(b) To measure the fluctuation spectrum of the instability in the nonlinear phase in order to explore its development, correlation properties and dispersion.

(c) To examine the time development of the electron distribution function which results from interaction with the collective electrostatic fields excited by the instability.

(d) To compare the electrical behaviour of the plasma with scaling laws obtained from other experiments.

At least some of these objectives have been met. For (a) the same well-defined threshold was observed for the onset of both anomalous conductivity and noise fluctuations. This threshold is in excellent agreement with the predictions of linear theory for the two-stream instability. On the other hand, it has proved much more difficult to make substantial progress for (b): while the observed spectral width and amplitude were of the right order to explain the measured particle scattering, it has not so far proved possible to measure correlation times and lengths; this is clearly a topic for further work.

As regards (c), the new technique developed for this problem (i.e. the time-resolved measurement of the dispersion of electron plasma waves), has proved to be a powerful means of measuring the most important moments of $F_e(v_{\parallel}, t)$ in an unambiguous way. Thus some of the doubts regarding the reliability of more conventional measurements in large turbulent heating experiments have diminished.

For (d): once the overall circuit behaviour, including the initial transients and the build-up of current, were understood, electrical measurements of plasma conductivity during the turbulent phase became possible. The values of average electrical conductivity found in this way agreed well with the electron scattering rate deduced from the dispersion of electron plasma waves, and were consistent with the results from other work when an appropriate ion mass and density scaling was used.

At present there is no understanding of the discrepancy between the overall behaviour predicted by computer simulation and physical experiment. In particular, the maintenance of strong turbulence after the clear violation of the <u>linear</u> instability criterion, ($v_d > 1.3\ v_e$), requires explanation.

Apart from the obvious continuation of work on the fluctuation spectrum itself, there are a number of other points which arise from this work:

(a) What, if any, are the changes in particle energies transverse to the magnetic field? This might be explored using a diamagnetic loop to measure $\Delta v_\perp^2$.

(b) What effect does the turbulence have on the ions? In many turbulent heating experiments significant ion heating occurred in the later stages.

(c) What is the explanation for the slow density decay, (Fig. 4.11)? Does it result from turbulent diffusion across the magnetic field, an expansion of the column (due to perpendicular pressure), or merely a change in the equilibrium properties of the Q-machine?

(d) Since relatively long wavelength electron plasma waves can clearly propagate through the turbulent plasma, what happens, (i) when their wavelengths become of the same order as those of the fluctuating fields; (ii) when their amplitudes are so large that they would, in quiescent plasma, be subject to nonlinear processes such as three-wave decay, (see e.g. FRANKLIN et al. (1975)).

APPENDIX A.1

DISPERSION RELATION FOR THE ELECTRON-ION TWO-STREAM INSTABILITY FOR A COLD 1-D PLASMA

Equation (2.2) can be derived from a self-consistent solution of the linearised particle continuity and momentum equations in conjunction with Poisson's equation, viz:

$$\left.\begin{aligned} &\frac{\partial n_{e,i}}{\partial t} + \frac{\partial}{\partial x}(n_{e,i}\cdot v_{e,i}) = 0 \\ (m_i \equiv M) \qquad &\frac{\partial v_{e,i}}{\partial t} + v_{e,i}\frac{\partial}{\partial x} v_{e,i} = \pm\frac{e}{m_{e,i}}\frac{\partial\varphi}{\partial x} \\ \text{and} \qquad &\frac{\partial^2\varphi}{\partial x^2} = -\frac{e}{\varepsilon_o}(n_i - n_e) \end{aligned}\right\} \qquad \ldots \text{(A1.1)}$$

We look for solutions of the form,

$$\left.\begin{aligned} n_{i,e} &= n_o + \tilde{n}_{i,e}\, e^{i(kx-\omega t)} \\ v_i &= \tilde{v}_i\, e^{i(kx-\omega t)} \\ v_e &= v_d + \tilde{v}_e\, e^{i(kx-\omega t)} \\ \varphi &= \tilde{\varphi}\, e^{i(kx-\omega t)} \end{aligned}\right\} \qquad \ldots \text{(A1.2)}$$

After substitution of (A1.2) into (A1.1) we can linearise the equations if we assume

$$\left.\begin{aligned} &\tilde{n}_{e,i} \ll n_o \\ &\tilde{v}_{e,i} \ll \omega/k \quad \text{and} \quad \tilde{v}_e \ll v_d \\ &e\tilde{\varphi} \ll M\left(\frac{\omega}{k}\right)^2 \quad \text{and} \quad e\tilde{\varphi} \ll m\left(\frac{\omega}{k} - v_d\right)^2 \end{aligned}\right\} \qquad \ldots \text{(A1.3)}$$

This will lead to equation (2.2), viz:

$$\frac{\omega_{pe}^2}{(\omega - kv_d)^2} + \frac{\omega_{pi}^2}{\omega^2} = 1 \qquad (2.2) .$$

For real-k , there are complex conjugate solutions $\omega = \omega_r \pm i\gamma$, if , (see e.g. MIKHAILOVSKII (1974) p.15),

$$k < \frac{\omega_{pe}}{v_d}\left[1 + \left(\frac{m}{M}\right)^{\frac{1}{3}}\right]^{\frac{3}{2}} \simeq \frac{\omega_{pe}}{v_d}$$

for which
$$|\omega| < \omega_{pe}\left(\frac{m}{M}\right)^{\frac{1}{3}}\left[1 + \left(\frac{m}{M}\right)^{\frac{1}{3}}\right]^{\frac{1}{2}} \simeq \omega_{pe}\left(\frac{m}{M}\right)^{\frac{1}{3}} .$$

Manipulating equation (2.2) leads to :

$$\omega - kv_d = \pm\, \omega_{pe}\left[1 - \frac{\omega_{pi}^2}{\omega^2}\right]^{-\frac{1}{2}}$$

If we assume that $\omega^2 \gg \omega_{pi}^2$, so that :

$$\omega - kv_d \simeq \pm\, \omega_{pe}\left[1 + \frac{\omega_{pi}^2}{2\omega^2}\right] \qquad \text{... (A1.4)}$$

then we can estimate complex solutions of ω (BUNEMAN (1958)).

In particular, if $k = \pm\, \omega_{pe}/v_d$

$$\omega^3 = -\frac{\omega_{pe}\,\omega_{pi}^2}{2}$$

i.e. three solutions:

$$\left.\begin{aligned} \omega &\equiv \omega_r = \frac{\omega^*}{2^{\frac{1}{3}}} \\ \omega &\equiv \omega_r \pm i\gamma = \frac{\omega^*}{2^{4/3}}\left[1 \pm i\sqrt{3}\right] \end{aligned}\right\} \qquad \text{... (A1.5)}$$

where
$$\omega^* = \left(\frac{m}{M}\right)^{\frac{1}{3}} \omega_{pe} .$$

Clearly the approximation for equation (A1.4) holds, if

$$\left(\frac{\omega_{pe}\,\omega_{pi}^2}{2}\right)^{\frac{2}{3}} \gg \omega_{pi}^2$$

i.e.
$$\frac{1}{2^{\frac{2}{3}}}\left(\frac{M}{m}\right)^{\frac{1}{3}} \gg 1 \quad . \qquad \text{... (A1.6)}$$

On the other hand if $k \ll \pm\, \omega_{pe}/v_d$ then, (MIKHAILOVSKII (op.cit.) p.13)

$$\omega \equiv \pm\, i\gamma = \pm\left(\frac{m}{M}\right)^{\frac{1}{2}} kv_d . \qquad \text{... (A1.7)}$$

These solutions of ω apply to the ion inertial frame; in the electron inertial frame γ is unchanged but ω_r is Doppler-shifted by kv_d.

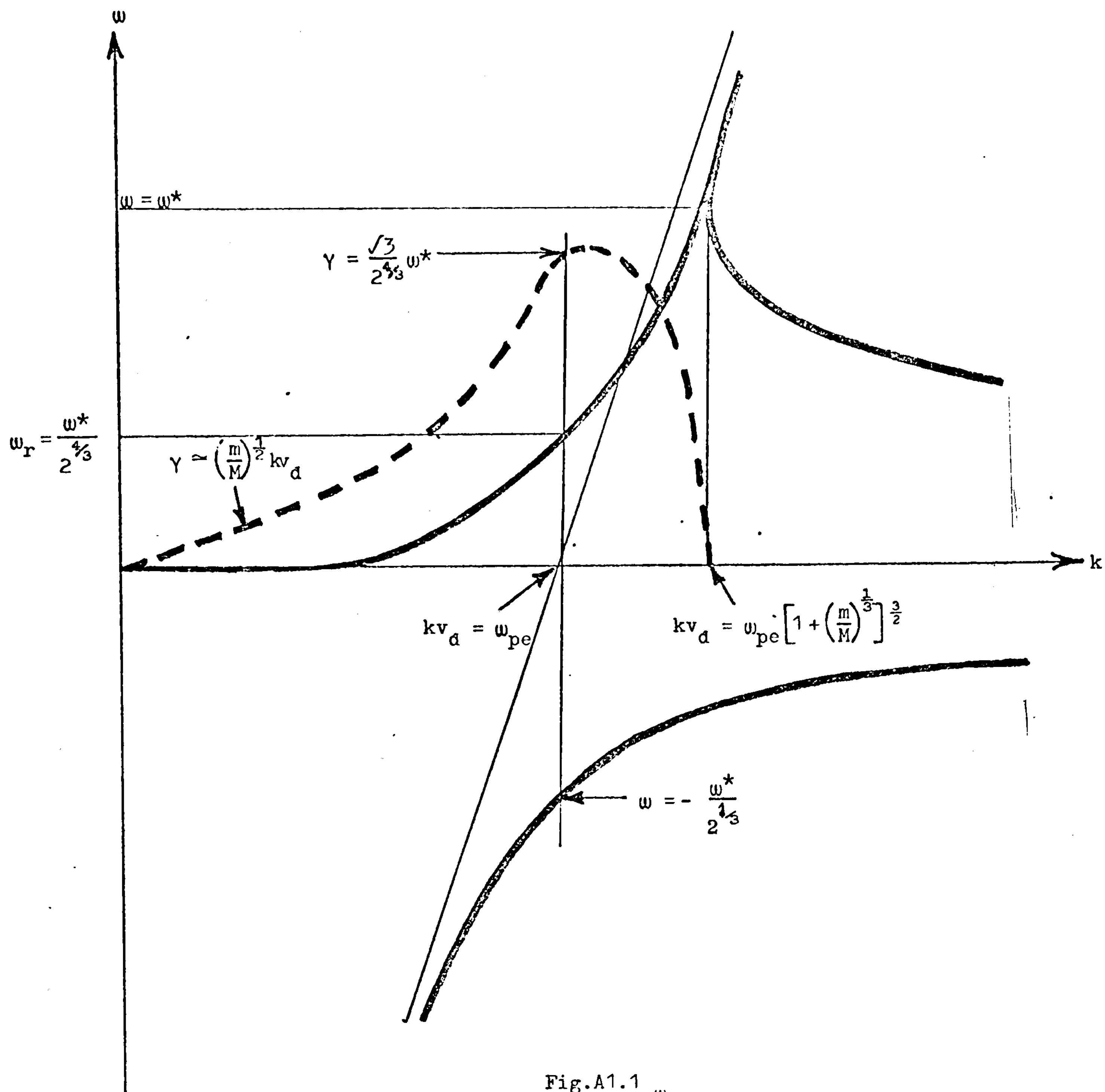

Fig.A1.1

Solutions of (2.2) for $k \leqslant \frac{\omega_{pe}}{v_d}$ and $\omega \ll \omega_{pe}$

In section 2.5.1 we require an estimate of

$$\int_0^t \gamma(t')\,dt'$$

where $t' = mv_d/eE_o$; thus

$$\gamma(kv_d) \equiv \gamma\left(\frac{keE_o t'}{m}\right) .$$

Using the approximations shown above; in the range

$$0 \leqslant t \leqslant \frac{m\,\omega_{pe}}{e\,E_o\,k} \quad , \quad \int_0^t \gamma(t')\,dt' \simeq 0.5\ \omega_{pi}\,t .$$

In the range,

$$\frac{m\,\omega_{pe}}{e\,E_o\,k}\left[1 - \left(\frac{m}{M}\right)^{\frac{1}{3}}\right]^{\frac{3}{2}} \leqslant t \leqslant \frac{m\,\omega_{pe}}{e\,E_o\,k}\left[1 + \left(\frac{m}{M}\right)^{\frac{1}{3}}\right]^{\frac{3}{2}}$$

$$\int_{t}^{t+\Delta t} \gamma \, dt' \simeq 1.4 \left(\frac{m}{M}\right)^{1/6} \omega_{pi} t$$

$$\simeq 0.2 \, \omega_{pi} t \quad \text{for potassium ions.}$$

Thus maximum amplification $\approx \exp\left(0.7 \, \omega_{pi} t\right)$, in a time

$$t \simeq \frac{m \, \omega_{pe}}{e E_o k} .$$

Finally, the restriction on the amplitude $\tilde{\varphi}$, for the results of linear theory to hold. From condition (A1.3)

$$e\tilde{\varphi} \ll m \left[\frac{\omega}{k} - v_d\right]^2 \quad \text{and} \quad e\tilde{\varphi} \ll M \left(\frac{\omega}{k}\right)^2 .$$

Thus if $|\omega| \sim \omega^*$, i.e. around maximum growth rate,

$$e\tilde{\varphi} \ll m v_d^2 \quad \text{and} \quad e\tilde{\varphi} \ll \left(\frac{M}{m}\right)^{\frac{1}{3}} m v_d^2 .$$

Thus the linear growth rates $(\gamma \sim \gamma_{max})$ apply for

$$e\tilde{\varphi} \ll m v_d^2 .$$

APPENDIX A.2

DISPERSION RELATION FOR A COLD PLASMA COMPLETELY FILLING A CYLINDRICAL WAVEGUIDE WITH AN AXIAL MAGNETIC FIELD SUCH THAT $\omega_{ce}^2 \gg \omega_{pe}^2 \gg \omega_{pi}^2 \gg \omega_{ci}^2$

The complete dispersion relation is equation (2.8), i.e.

$$D(\omega,k) = 0 = 1 + \frac{1}{1+K^2}\left\{\frac{\omega_{pe}^2}{\omega_{ce}^2 - (\omega - k_z v_d)^2} + \frac{\omega_{pi}^2}{\omega_{ci}^2 - \omega^2}\right\} - \frac{K^2}{1+K^2}\left\{\frac{\omega_{pe}^2}{(\omega - k_z v_d)^2} + \frac{\omega_{pi}^2}{\omega^2}\right\}$$

where
$$K = \frac{k_z a}{p_{\mu\nu}} \qquad \ldots (2.8).$$

Each term in this equation represents a plasma resonance. If the condition $\omega_{ce}^2 \gg \omega_{pe}^2 \gg \omega_{pi}^2 \gg \omega_{ci}^2$, holds then to a first approximation we can consider each resonance separately. E.g. if $v_d = 0$, equation (2.8) has three resonances, (see Mikhaelovskii (op.cit.) pp.142–145), viz. for $\omega \sim \omega_{ce}$

$$D(\omega,k) \simeq 1 + \frac{1}{1+K^2}\,\frac{\omega_{pe}^2}{\omega_{ce}^2 - \omega^2}$$

then

$$\omega^2 \simeq \omega_{ce}^2 + \frac{\omega_{pe}^2}{1+K^2} \qquad \ldots (A2.1)$$

i.e. <u>electrostatic electron cyclotron oscillations</u>. Similarly for

$$\omega_{pe} \geqslant \omega \geqslant \omega_{pi}$$

$$\omega^2 \simeq \frac{\omega_{pe}^2\left(K^2 + \frac{m}{M}\right)}{K^2 + 1} \qquad \ldots (A2.2)$$

i.e. <u>electrostatic plasma oscillations</u>. Also for $\omega \leqslant \omega_{ci}$

$$\omega^2 \simeq \frac{\omega_{ci}^2}{1 + \frac{1}{K^2}\frac{m}{M}} \qquad \ldots (A2.3)$$

i.e. <u>electrostatic ion cyclotron oscillations</u>.

When the electrons drift with velocity v_d, it is possible for the electron resonant frequencies, when Doppler-shifted by kv_d into the ion inertial frame, to coincide with the ion resonant frequencies. The dispersion relation is shown schematically in Fig.A2.1.

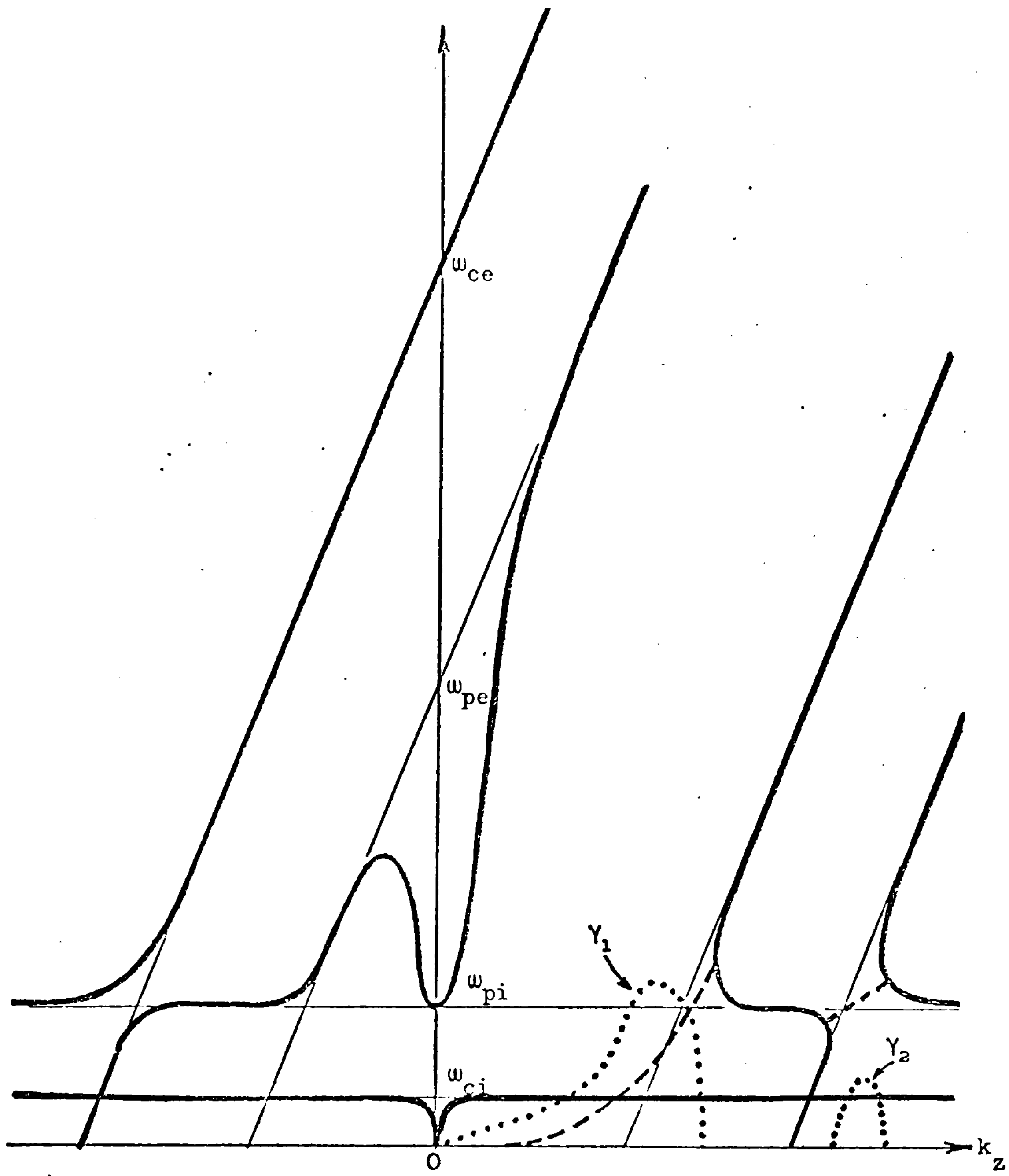

Fig.A2.1

Schematic representation of the dispersion relation (2.8)

——— purely real solutions

- - - - - - real part } complex conjugate

.... positive imaginary part } solutions of ω

To estimate the maximum growth rates of the two instabilities, γ_1 and γ_2, as before, we consider each interaction separately.

γ_1, Interaction between Doppler-shifted electron plasma oscillations and ion plasma oscillations in the ion inertial frame, i.e. the electron-ion two-stream instability:

For $|\omega_{ce} - k_z v_d| \gg |\omega| \gg \omega_{ci}$, equation (2.8) becomes:

$$D(\omega,k) = 0 \simeq 1 - \frac{K^2\omega_{pe}^2}{1+K^2}\,\frac{1}{(\omega - KV)^2} - \frac{\omega_{pi}^2}{\omega^2} \qquad \ldots \text{(A2.4)}$$

where $V = \dfrac{v_d p_{\mu\nu}}{a}$.

If we now consider V as the variable rather than K, (A2.4) is mathematically identical to the 1-D dispersion relation (2.2), provided the substitution

$$\frac{K^2\omega_{pe}^2}{1+K^2} \rightarrow \omega_{pe}^2$$

is made. Thus the solutions follow from Appendix A.1, viz :

$$\gamma_{1\,max} \simeq \frac{\sqrt{3}}{2^{4/3}}\,\omega^* \left(\frac{K^2}{1+K^2}\right)^{1/6} \qquad \ldots \text{(A2.5)}$$

for

$$\omega_r = \frac{\gamma_{1\,max}}{\sqrt{3}}$$

and

$$KV = \frac{K\omega_{pe}}{(1+K^2)^{\frac{1}{2}}} \,.$$

Substituting for K in equation (A2.5) leads to

$$\left.\begin{aligned} \gamma_{1\,max} &\simeq \frac{\sqrt{3}}{2^{4/3}}\,\omega^* \left(1 - \frac{p_{\mu\nu}^2\, v_d^2}{\omega_{pe}^2\, a^2}\right)^{1/6} \\ \text{for} \quad k_z &\simeq \frac{\omega_{pe}}{v_d}\left(1 - \frac{p_{\mu\nu}^2\, v_d^2}{\omega_{pe}^2\, a^2}\right)^{\frac{1}{2}} \end{aligned}\right\} \qquad \ldots \text{(A2.6)}$$

The approximation condition (A2.4) means that

$$|\gamma_{1\,max}| \gg \omega_{pi} \,,$$

thus we require,

$$\frac{p_{\mu\nu}^2\, v_d^2}{\omega_{pe}^2\, a^2} \ll 1 \,. \qquad \ldots \text{(A2.7)}$$

Notice that if both electrons and ions are magnetised, i.e. $\omega_{ci} \gg \omega_{pi}$, then the result is somewhat different

$$\gamma_{1\,max} \simeq 0.7\,\omega^* \left(1 - \frac{p_{\mu\nu}^2\, v_d^2}{\omega_{pe}^2\, a^2}\right)^{\frac{1}{2}}$$

and the two-stream instability is stabilised if

$$\left.\begin{aligned} v_d &\geq \frac{\omega_{pe}\, a}{p_{oo}}\left[1 + \left(\frac{m}{M}\right)^{\frac{1}{3}}\right]^{\frac{3}{2}} \\ \text{where} \quad p_{oo} &\simeq 2.4 \end{aligned}\right\} \qquad \ldots \text{(A2.8)}$$

γ_2, Interaction between Doppler-shifted electron cyclotron oscillations and ion plasma oscillations

For $|\omega_{pe} - k_z v_d| \gg |\omega| \gg \omega_{pi}$, equation (2.8) becomes :

$$D(\omega,k) = 0 \simeq 1 + \frac{1}{(1+K^2)} \frac{\omega_{pe}^2}{\omega_{ce}^2 - (\omega - KV)^2} - \frac{\omega_{pi}^2}{\omega^2} \qquad \text{... (A2.9)}$$

Thus,
$$\omega_{ce}^2 - (\omega - KV)^2 \simeq - \frac{\omega_{pe}^2}{1+K^2}\left(1 + \frac{\omega_{pi}^2}{\omega^2}\right)$$

$$\omega - KV \simeq - \omega_{ce}\left[1 + \frac{1}{\omega^2}\left(\frac{\omega_{pe}}{\omega_{ce}}\right)^2 \frac{\omega_{pi}^2}{2(1+K^2)}\right] \qquad \text{... (A2.10)}$$

This equation (A2.10), is mathematically analogous to (A1.4). Thus at $KV = \omega_{ce}$

$$\omega^3 = -\left(\frac{\omega_{pe}}{\omega_{ce}}\right) \frac{1}{1+K^2} \frac{\omega_{pe}\,\omega_{pi}^2}{2}.$$

Following the same procedure as in appendix A.1,

$$\left.\begin{aligned} \gamma_{2\,max} &\simeq \frac{\sqrt{3}}{2^{4/3}}\,\omega^* \left(\frac{\omega_{pe}}{\omega_{ce}}\right)^{\frac{1}{3}} \left(\frac{v_d\, p_{\mu\nu}}{a\,\omega_{ce}}\right)^{\frac{2}{3}} \\ \text{for} \quad k_z &\simeq \frac{\omega_{ce}}{v_d} \end{aligned}\right\} \qquad \text{... (A2.11)}$$

where the condition for the approximation is (A2.7).

Intersection between the dispersion curves for Doppler-shifted electron cyclotron oscillations and ion cyclotron oscillations

These two oscillations do not interact and there is no instability. This can be proved as follows.

In the intersection region, $|\omega - k_z v_d| \gg \omega_{pe}$, so that (2.8) becomes

$$D(\omega,k) = 0 \simeq 1 + \frac{1}{1+K^2} \frac{\omega_{pe}^2}{\omega_{ce}^2 - (\omega - KV)^2} + \frac{1}{1+K^2} \frac{\omega_{pi}^2}{\omega_{ci}^2 - \omega^2} - \frac{K^2}{1+K^2} \frac{\omega_{pi}^2}{\omega^2} \qquad \text{... (A2.12)}$$

Again we can fix K and consider ω and V as the two variables. Transforming these to the new variables α and β where,

$$\left.\begin{aligned} \alpha &= \omega \\ \beta &= \omega - KV \end{aligned}\right\} \qquad \text{... A2.13)}$$

and multiplying (A2.12) through by $\alpha^2(\omega_{ce}^2 - \beta^2)(\omega_{ci}^2 - \alpha^2)$ gives :

$$\alpha^4\left[\frac{\omega_{pe}^2}{1+K^2} + \omega_{ce}^2 - \beta^2\right] - \alpha^2\left[(\omega_{ce}^2 - \beta^2)(\omega_{pi}^2 + \omega_{ci}^2) + \frac{\omega_{pe}^2}{1+K^2}\,\omega_{ci}^2\right]$$

$$+ \frac{K^2\omega_{pi}^2}{1+K^2}\cdot\omega_{ci}^2(\omega_{ce}^2 - \beta^2) = 0 \qquad \ldots \text{(A2.14)}$$

Now consider the solution for α where

$$\beta^2 = \omega_{ce}^2$$

i.e.
$$\alpha^4\frac{\omega_{pe}^2}{1+K^2} - \alpha^2\frac{\omega_{pe}^2\omega_{ci}^2}{1+K^2} = 0 \;.$$

Thus
$$\alpha^2 = 0$$
and
$$\alpha^2 = \omega_{ci}^2 \qquad \ldots \text{(A2.15)}$$

i.e. at the intersection of the dispersion curves

$$\omega = k_z v_d \pm \omega_{ce} \qquad \text{and} \qquad \omega = \pm\,\omega_{ci}$$

there are real solutions for ω and k_z; the curves pass through each other (see Fig.A2.1).

APPENDIX A.3

DISPERSION RELATION FOR ELECTRON PLASMA WAVES

The following is an outline of the linear theory for the dispersion of electron plasma waves in a warm, magnetised plasma column partly filling a cylindrical waveguide. For a more detailed account see FRANKLIN et al. (1974).

Following the discussion in section 2.3 we solve

$$\underline{\nabla} \cdot (\underline{\underline{\epsilon}}\, \underline{\nabla} \varphi) = 0 \qquad (2.1)$$

where, in the frequency regime,

$$\omega_{ce}^2 \gg \omega_{pe}^2 \geqslant \omega^2 \gg \omega_{pi}^2 \qquad \ldots \text{(A3.1)}$$

the plasma dielectric tensor is well approximated by

$$\underline{\underline{\epsilon}} = \begin{pmatrix} 1 & 0 & 0 \\ 0 & 1 & 0 \\ 0 & 0 & \epsilon_3 \end{pmatrix} \qquad \ldots \text{(A3.2)}$$

where

$$\epsilon_3(\omega, k_z, r) = 1 - \frac{\omega_{pe}^2}{k_z^2} f(r) \int_{-\infty}^{+\infty} \frac{\frac{\partial F_e}{\partial v_z}\, dv_z}{(v_z - \omega/k_z)} \qquad \ldots \text{(A3.3)}$$

and the radial density profile is given by

$$n(r) = n_o\, f(r) \qquad \ldots \text{(A3.4)}$$

such that n_o is the density at $r = 0$, (see Fig.2.5).

Substitution of equations (A3.3) and (A3.4) into (2.1) yields a solution of the form

$$\varphi(r, \theta, z, t) = R_\mu(r)\, e^{i\mu\theta}\, e^{i(k_z z - \omega t)} \qquad \ldots \text{(A3.5)}$$

where $R_\mu(r)$ is a solution to

$$r^2 \frac{d^2R}{dr^2} + r \frac{dR}{dr} - \left\{ \left[1 + f(r)\, h(\omega, k_z) \right] k_z^2 r^2 + \mu^2 \right\} R = 0 \qquad \ldots \text{(A3.6)}$$

and

$$h(\omega,k_z) = -\frac{\omega_{pe}^2}{k_z^2}\int_{-\infty}^{+\infty}\frac{\frac{\partial F_e}{\partial v_z}.\,dv_z}{(v_e - \omega/k_z)} \quad . \quad . \qquad \ldots (A3.7)$$

The boundary condition

$$\varphi(r=b) = 0 \qquad \ldots (A3.8)$$

determines the dispersion relation for a prescribed $f(r)$. In principle it is possible to integrate equation (A3.6) from $r=0$ to $r=b$ with prescribed values of k_z and μ to determine the numerical values of h which make R vanish at $r=b$; i.e. for the prescribed variable k_z, the boundary condition (A3.8) determines an eigenvalue equation

$$h = g_{\mu\nu}(k_z) \qquad \ldots (A3.9)$$

for a prescribed $f(r)$ such that equation (A3.7) can be solved for ω.

i.e. $$g_{\mu\nu}(k_z) = -\frac{\omega_{pe}^2}{k_z^2}\int_{-\infty}^{+\infty}\frac{\frac{\partial F_e}{\partial v_z}\,dv_z}{(v_z - \omega/k_z)} \qquad \ldots (A3.10)$$

Integrating by parts and manipulating (A3.10) we obtain the form for the lowest order (0,0) mode used in section 4.5, viz

$$\frac{\omega^2}{\omega_{pe}^2} = G(k_z)\int_{-\infty}^{+\infty}\frac{F_e(v_z)\,dv_z}{\left(1 - \frac{k_z v_z}{\omega}\right)^2} \qquad \ldots (4.9)$$

where $$G(k_z) = \frac{1}{g_{oo}(k_z)} .$$

If the density is radially uniform such that

$$\begin{aligned} f(r) &= 1 \qquad \text{for} \quad 0 \le r \le a \\ &= 0 \qquad \text{for} \quad a < r \le b \end{aligned} \qquad \ldots (A3.11)$$

then the general solution to equation (A3.6) will be

$$R = A I_\mu\left(\sqrt{\epsilon_3}\,k_z r\right) + B K_\mu\left(\sqrt{\epsilon_3}\,k_z r\right) \qquad \ldots (A3.12)$$

where I_μ and K_μ are modified Bessel functions of the first and second kinds respectively. For a finite value of R at $r=0$, we require $B=0$ so that inside the plasma column $(r \le a)$,

$$\varphi = A\, I_\mu\left(\sqrt{\epsilon_3}\, k_z r\right)\, e^{i\mu\theta}\, e^{i(k_z z - \omega t)}$$

$$= \tilde{\varphi}\, J_\mu\left(p_{\mu\nu}\frac{r}{c}\right)\, e^{i\mu\theta}\, e^{i(k_z z - \omega t)} \qquad \ldots \text{(A3.13)}$$

where $c \equiv c(\omega, k_z)$.

Outside the column $(a < r \leq b)$,

$$\varphi = \left[A' I_\mu(k_z r) + B' K_\mu(k_z r)\right] e^{i\mu\theta}\, e^{i(k_z z - \omega t)} \qquad \ldots \text{(A3.14)}$$

The solution for the (0,0) mode is shown in Fig.A3.1.

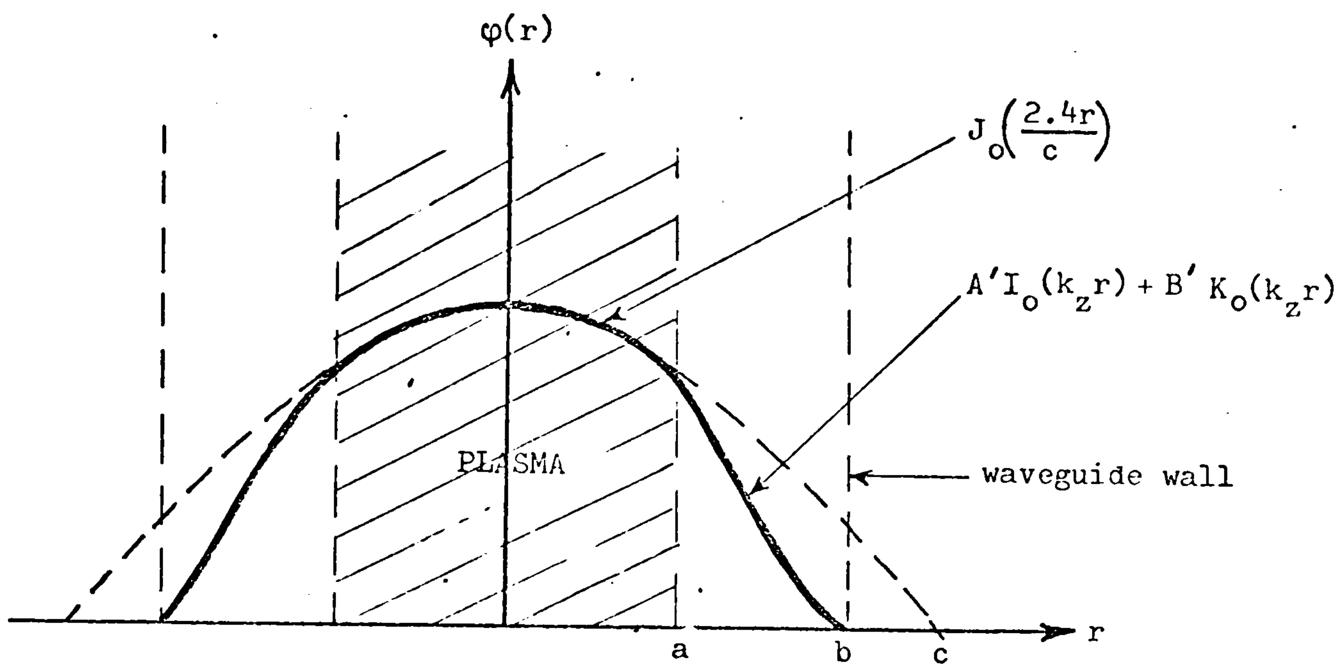

Fig.A3.1
The radial potential profile of the lowest order (0,0) mode in a uniform plasma column, $\omega < \omega_{pe}$; $c \to a$ as $\omega \to \omega_{pe}$

The eigenvalue equation (A3.9), is obtained by matching solutions (A3.13) and (A3.14) at $r = a$, combined with equation (A3.8); this leads to the well documented but rather cumbersome form :

$$\frac{J_\mu(i\sqrt{\epsilon_3}\, k_z a)}{i\sqrt{\epsilon_3}\, J'_\mu(i\sqrt{\epsilon_3}\, k_z a)} = \frac{I_\mu(k_z a)\, K_\mu(k_z b) - I_\mu(k_z b)\, K_\mu(k_z a)}{I'_\mu(k_z a)\, K_\mu(k_z b) - I_\mu(k_z b)\, K'_\mu(k_z a)} \qquad \ldots \text{(A3.15)}$$

(see e.g. BECK (1958), p.168).

A particularly simple form of $G(k_z)$ occurs in the completely-filled waveguide model used in Chapter III; i.e. if $a = b$ then

$$G(k_z) = \frac{k_z^2 a^2}{k_z^2 a^2 + (2.4)^2}$$

(*cf.* equation (3.8)).

BARRETT et al. (1968) have computed the dispersion relation for parabolic $f(r)$ with $\frac{b}{a} \to \infty$. When compared with the results for a uniform $f(r)$, (equation (A3.11)), the modification to the dispersion curve is greatest at long wavelengths, (see Fig.4.1(a)).

APPENDIX A.4

VARIATIONS OF THE TECHNIQUE FOR TIME-RESOLVED MEASUREMENTS OF THE DISPERSION OF ELECTRON PLASMA WAVES

In order to obtain the data shown in Figs.4.9 and 4.11, ~ 500 wavelength measurements are required for each set of conditions. With the standard technique outlined in section 4.3 this procedure would take ~ 8 hours ! In this appendix we describe two variants of the basic technique which permit faster data acquisition.

In general the phase-difference between the transmitted and received signals depends on three variables: frequency $\omega/2\pi$, separation z, and time-delay t, of the sampling gate. In the standard technique ω and t are kept constant whilst z is varied; however it is possible to keep z constant whilst sweeping one of the other two variables.

(a) Swept-Delay, Constant Separation and Frequency

In this variant the interferometer trace is a record of the variation with t of the transmitter-receiver phase difference for fixed ω_0 and z_0 due to the temporal variation of the wavelength $2\pi/k_z(t)$.

If the wavelength is measured at times t_1 and t_2 using the basic technique, then it is possible to interpolate accurately for wavelengths in the interval $t_1 < t < t_2$, from the swept-delay interferometer trace. The circuit is shown in Fig.A4.1; (although unnecessary in this circuit, it was found that the signal-to-noise ratio for the interferometer trace is improved if the trigger for the sampling unit is synchronised to ω_0 using the method depicted in Fig.4.3(b)). Thus the received signal is:

$$R_1(t) = A\cos\left(k_z(t)z_0 - \omega_0 t\right) \qquad \ldots \text{(A4.1)}$$

where

$$\left|\frac{1}{k_z}\frac{dk_z}{dt}\right| \ll \omega_0 .$$

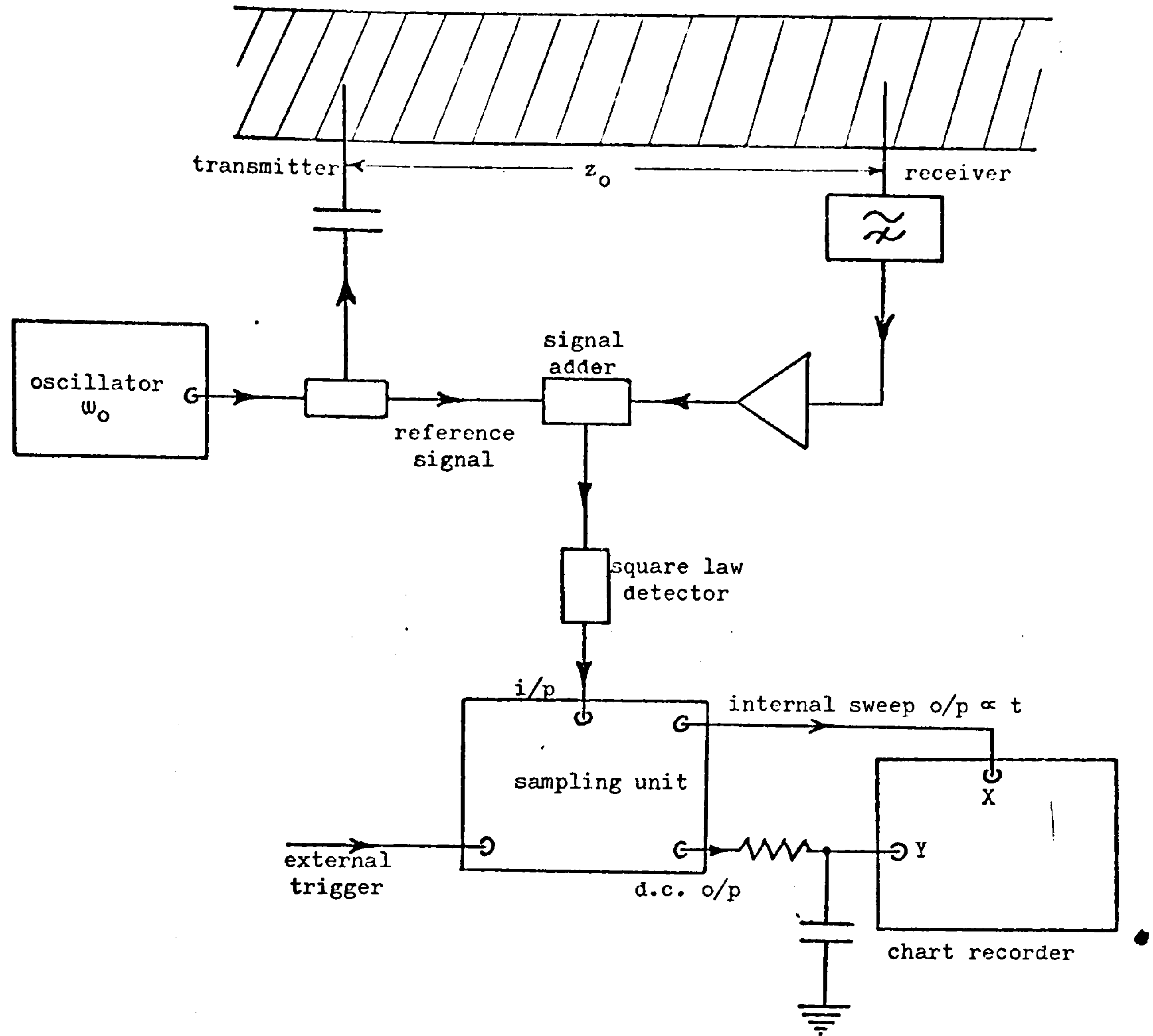

Fig.A4.1
Circuit for swept-delay interferometer

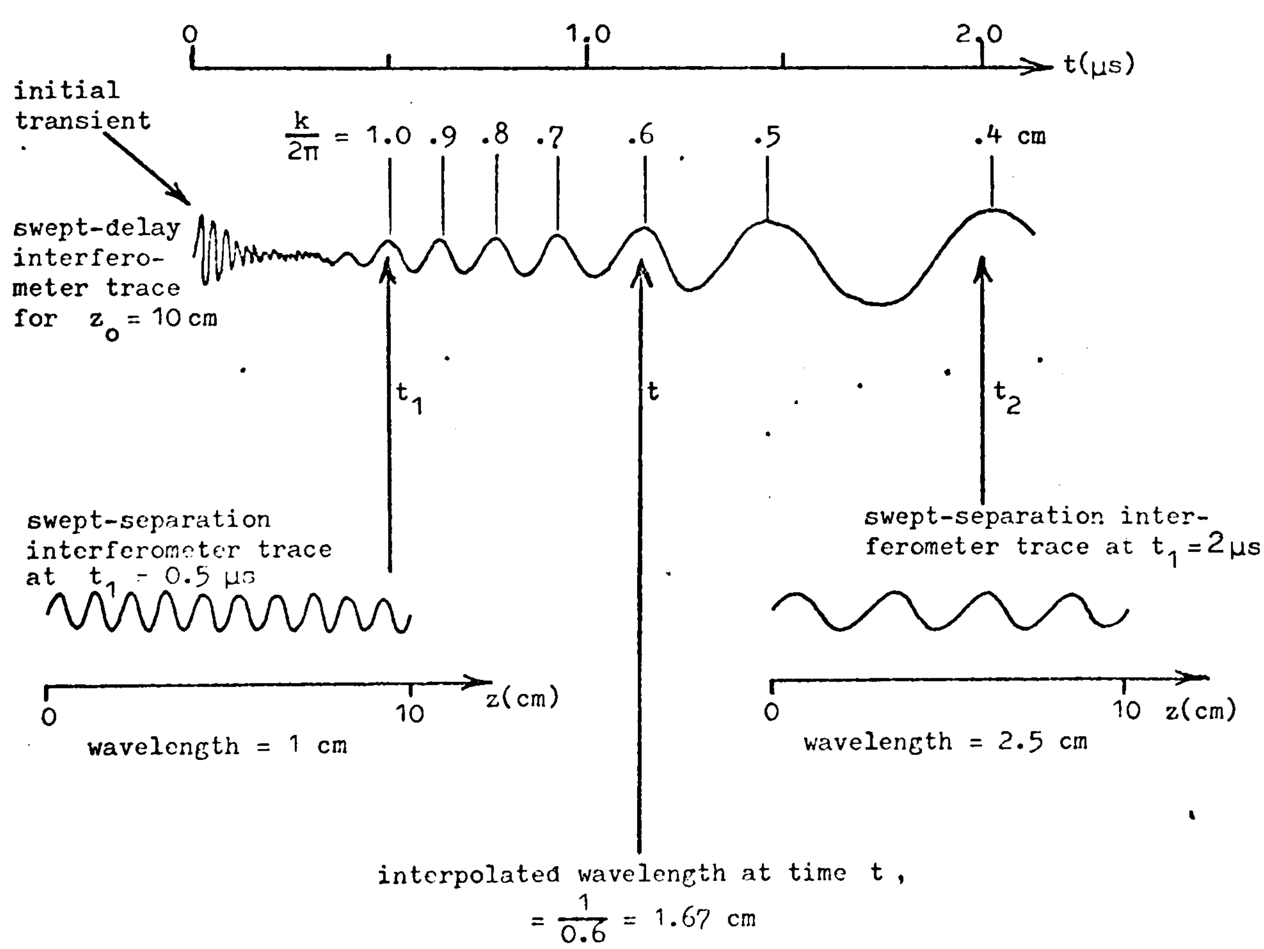

Fig.A4.2
Schematic illustration of wavelength interpolation for a swept-delay interferometer trace at fixed frequency ω_o

The reference signal is

$$R_2(t) = B\cos\omega_o t \qquad \text{... (A4.2)}$$

so that the output from the signal adder will be

$$R_3(t) = A\cos\left(k_z(t)\,z_o - \omega_o t\right) + B\cos\omega_o t \qquad \text{... (A4.3)}$$

The detector squares $R_3(t)$ and averages over one cycle $^{2\pi}/\omega_o$. This signal is applied to the sampling unit whose delay is being swept slowly ($\sim 1\,\mu s\,min^{-1}$) between t_1 and t_2 so that the d.c. output will be

$$Y(t) = \tfrac{1}{2}\,(A^2 + B^2) + AB\cos\left(k_z(t)\,z_o\right) \qquad \text{... (A4.4)}$$

Figure A4.2 shows schematically how the value of k_z can be interpolated between t_1 and t_2. Care must be taken to ensure that the measurements are self-consistent. The interpolation will be incorrect if $\frac{dk_z}{dt}$ should change sign between t_1 and t_2 or if k_z is not spatially uniform, as is the case during the initial transient.

(b) Swept-Frequency, Constant Delay and Separation

The principle of this variant is analogous to (a) with the roles of ω and t interchanged. The swept-frequency interferometer trace is a record of the variation with ω of the transmitter-receiver phase difference for fixed t_o and z_o due to the dispersion of wavelengths $^{2\pi}/k_z(\omega)$.

The trace is calibrated in an analogous manner by measuring the wavelength at two frequencies ω_1 and ω_2 so that it is possible to interpolate for wavelengths in the interval, $\omega_1 < \omega < \omega_2$. The circuit is shown in Fig.A4.3.

The phase-delay of the coaxial cables in the external circuit varies as the frequ ncy is swept. Thus the delay line in the external trigger must be trimmed such that the time-delay of the sampling gate with respect to the second pulse generator is equal to the time-delay of the amplifier, filter and cables connected to the transmitter and receiver probes. Then

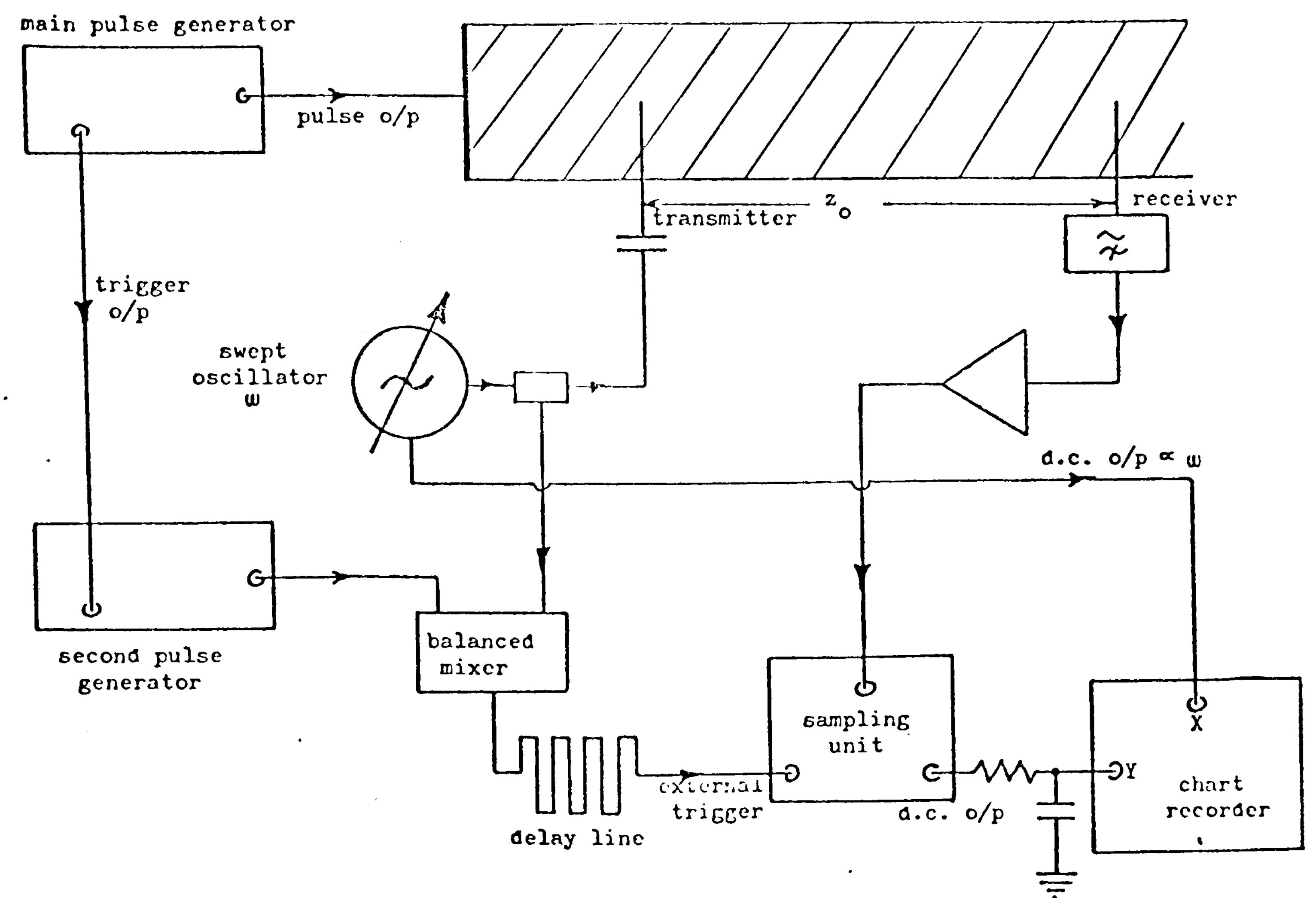

Fig.A4.3
Circuit for swept-frequency interferometer

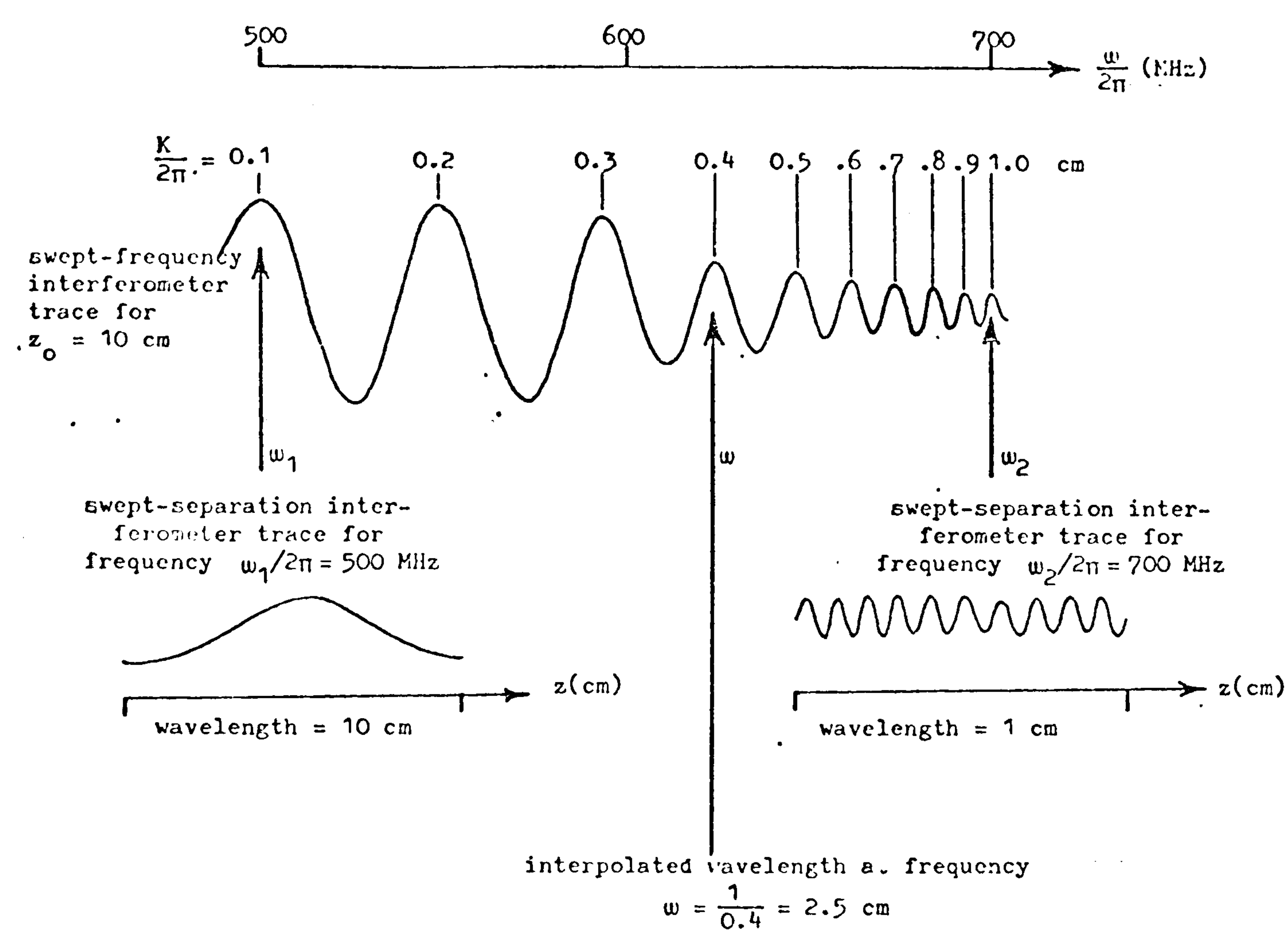

Fig.A4.4
Schematic illustration of wavelength interpolation for a swept-frequency interferometer trace at a fixed time-delay, t_o

the phase change observed as ω is swept consists only of the phase change between the transmitter and receiver probes due to the propagation of electron plasma waves in the column.

In practice the probes are set close together so that the coupling of the signal is dominated by the waveguide cut-off mode whose phase change will not vary with ω for fixed t_o. The delay is trimmed by adjusting the manual delay control on the sampling unit until the swept-frequency interferometer trace shows zero phase change over the swept frequency range. If the probes are now separated such that the electromagnetic coupling is negligible, traces similar to the one in Fig.A4.4 are observed. The time-delay of the sampling gate with respect to the current pulse can be varied by varying the time-delay of the second pulse generator.

APPENDIX A.5

THE ENSEMBLE AVERAGE POWER SPECTRUM OF THE HIGH-FREQUENCY FLUCTUATIONS MEASURED WITH AN ELECTRONIC SPECTRUM ANALYSER

If a signal $f(t)$, is gated with a series of window pulses of width τ_g, and repetition time τ_r, in the manner depicted in Fig.5.9, then the Fourier transform of the product will be a convolution integral, viz: the gated signal $S(t)$ is given by

$$\left.\begin{aligned} S(t) &= \sum_{n=-\infty}^{+\infty} f(t) \,.\, w(t-n\tau_r) \\ \text{where} \quad w(t) &= H(t+\tfrac{1}{2}\tau_g) - H(t-\tfrac{1}{2}\tau_g) \end{aligned}\right\} \quad \ldots \text{(A5.1)}$$

Thus the Fourier transform $\bar{S}(\omega)$ is given by

$$\left.\begin{aligned} \bar{S}(\omega) &= \int_{-\infty}^{+\infty} \bar{f}(\omega-\omega')\, \bar{w}(\omega')\, d\omega' \\ \text{where} \quad \bar{w}(\omega') &= \int_{-\infty}^{+\infty} \tau_g \, \frac{\sin\left[\left(\frac{\omega'-\omega''}{2}\right)\tau_g\right]}{\left(\frac{\omega'-\omega''}{2}\right)\tau_g} \sum_{n=-\infty}^{+\infty} \delta\left(\omega'' - \frac{2\pi n}{\tau_r}\right) d\omega'' \end{aligned}\right\} \quad . \text{(A5.2)}$$

Figure A5.1 shows a sketch of $\bar{w}(\omega')$ which determines the maximum resolution of $\bar{f}(\omega)$.

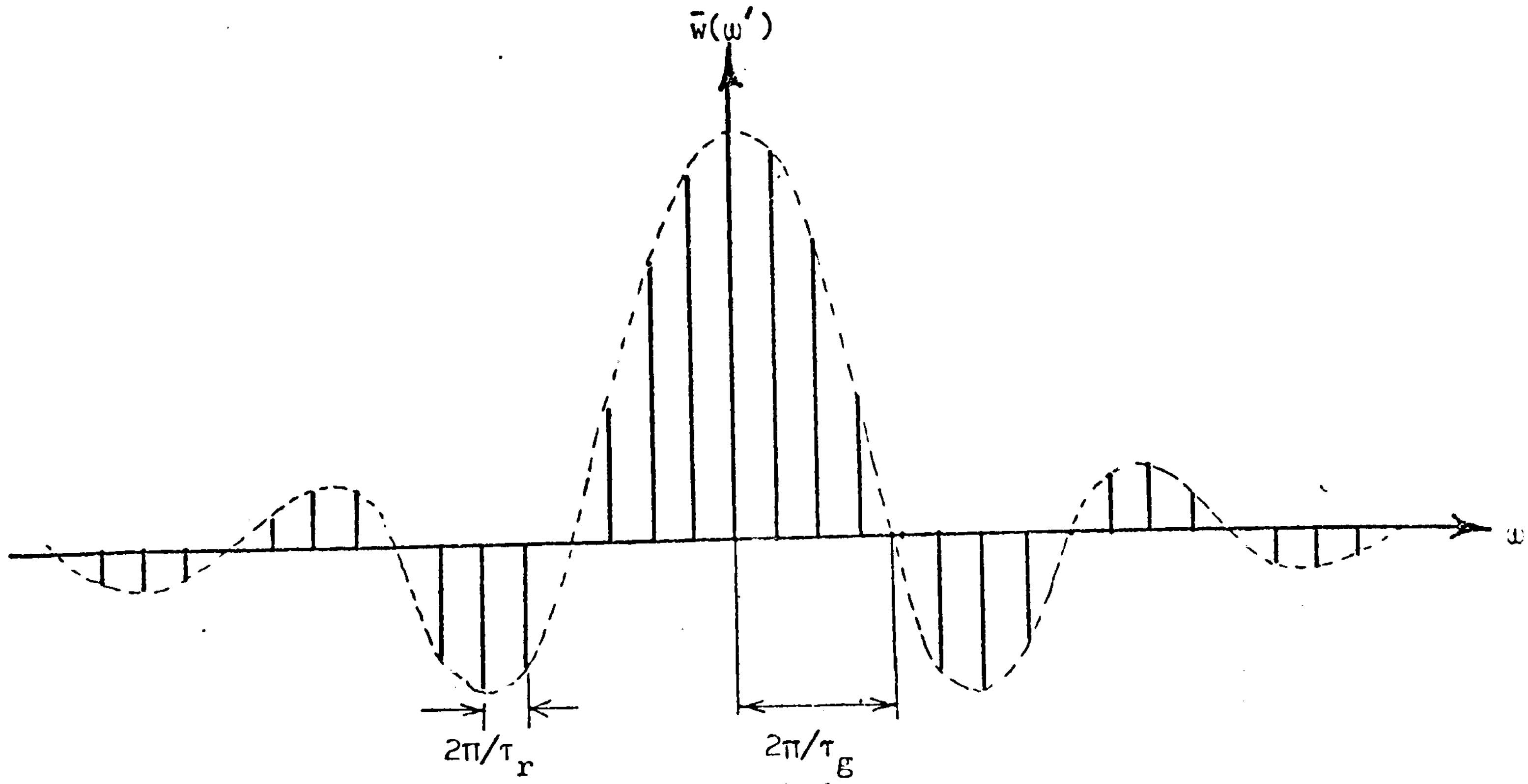

Fig.A5.1
The function $\bar{w}(\omega')$

In the experiment the situation is more complicated. The input to the spectrum analyser is a series of short duration (0.2 μs) pulses whose frequency spectra may vary from pulse to pulse. The spectrum analyser can only make measurements on signals whose frequency spectra are stationary during the period of measurement, (which can be varied from 0.01 to 100 s). In order to understand how the instrument can measure ensemble average power spectra for pulses 0.2 μs in duration, consider an idealised model for an electronic spectrum analyser shown in Fig.A5.2(a). In Fig.A5.2(b) we show how a Fourier component of the signal at frequency ω, passes through the system when the local oscillator frequency ω_0, is close to ω. Thus the input signal $S(t)$, can be considered as

$$S(t) = \int_{-\infty}^{+\infty} \left[\sum_n A_n(\omega) \cos \delta_n \cos \omega t \,.\, w(t - n\tau_r) \right] \frac{d\omega}{2\pi} \qquad \ldots \text{(A5.3)}$$

where $A_n(\omega)$ is the amplitude and δ_n the phase of a component with frequency ω during the n^{th} pulse: thus the ensemble average power spectrum is a measure of $\langle |A_n(\omega)|^2 \rangle$.

The mixer multiplies $S(t)$ with the local oscillator signal, so that the i.f. output

$$= \int_{-\infty}^{+\infty} \left[\sum_n \tfrac{1}{2} A_n(\omega) \cos \delta_n (\cos(\omega - \omega_0)t + \cos(\omega + \omega_0)t) \,.\, w(t - n\tau_r) \right] \frac{d\omega}{2\pi} \,.$$

The passage of this signal through the i.f. filter will depend in detail on the transfer function for the filter. For example, if we consider a simple low-pass R C filter, then only those components with $|\omega - \omega_0| \leqslant \frac{2\pi}{\tau_g}$ will pass through relatively unattenuated and for those components where $|\omega - \omega_0| \ll \frac{2\pi}{\tau_g}$ the amplitude of the output pulses will be

$$\propto \sum_n A_n \cos \delta_n \left(1 - e^{-\tau_g/RC}\right) .$$

In general the instrument can only detect signals if:

$$\tau_g \geqslant \frac{1}{\text{i.f. bandwidth}} \qquad \ldots \text{(A5.4)}$$

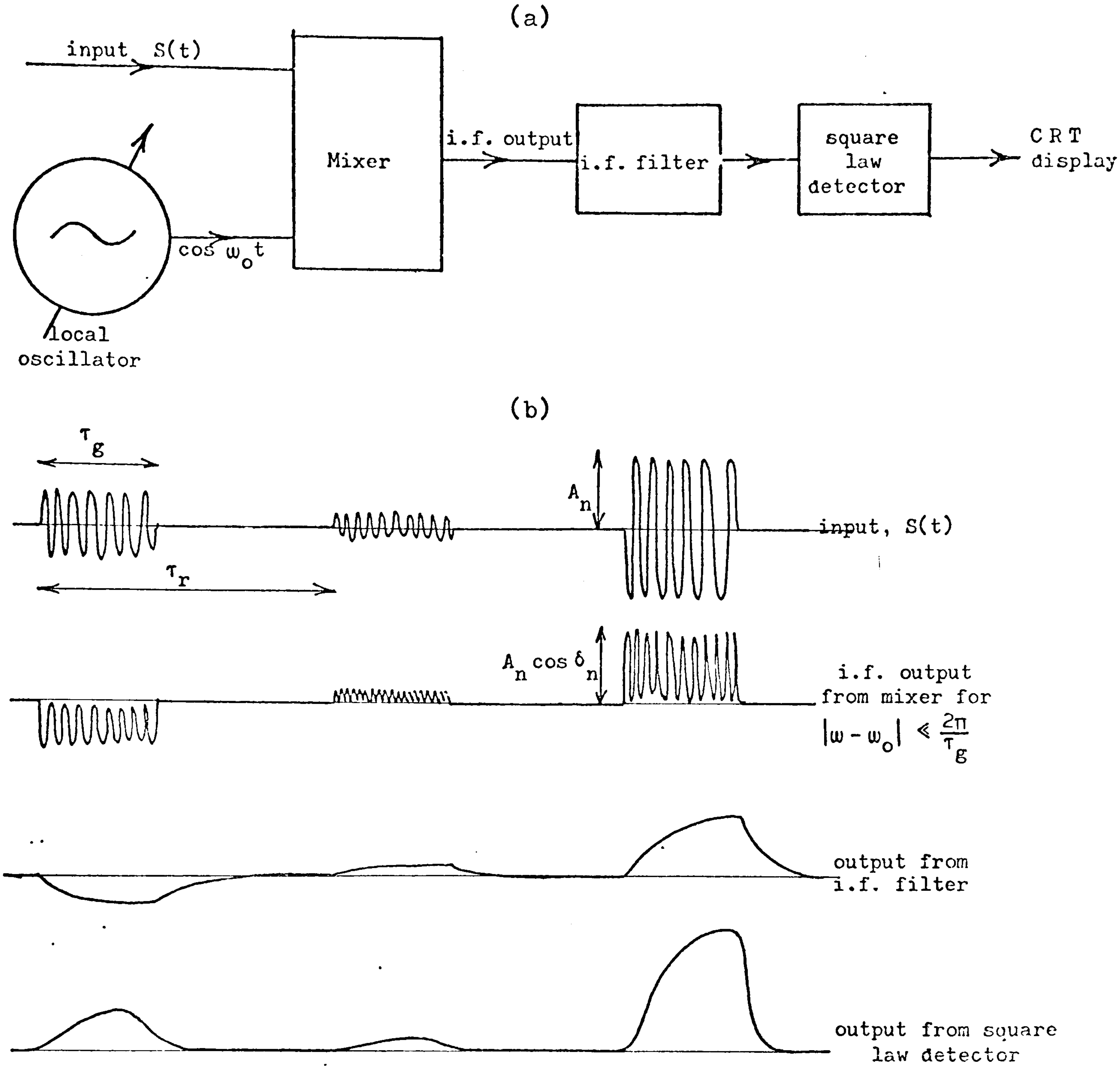

Fig.A5.2

(a) Schematic circuit for an idealised spectrum analyser

(b) Passage through the circuit of a Fourier component with frequency ω close to ω_o

The square law detector rectifies and squares the pulse output from the i.f. filter and the final output is written on to a cathode ray tube storage screen as the local oscillator is slowly swept, producing a display $\propto \langle |A_n(\omega)|^2 \rangle$, (the integration is carried out on the screen itself because the intensity of the display $\propto$ writing density). For the data shown in Fig.5.10, the logarithmic display facility was used. Most commercial instruments have a video filter between the detector and the display. This must be switched off for this type of measurement otherwise the pulse output from the detector will be filtered out. The criteria which determine the instrument parameters are listed below.

(a) i.f. bandwidth: the maximum i.f. bandwidth of the instrument determines the minimum gate width (A5.4). This was 300 KHz on the instrument used; (Hewlett Packard HP 8554L spectrum analyser).

(b) Gate width: determines the frequency resolution (A5.2).

(c) Video filter: this must be switched off.

(d) Local oscillator sweep rate: this determines the number of samples per frequency interval, e.g. with a sweep rate of 10 MHz s^{-1} and a pulse repetition rate of 500 s^{-1}. Number of samples per MHz = 50 .

REFERENCES

ANDERSEN, S.A., JENSEN, V.O., MICHELSEN, P. and NIELSEN, P., Phys. Fluids, 14, 728 (1971).

BARRETT, P.J., JONES, H.G. and FRANKLIN, R.N., Plasma Physics, 10, 911 (1968).

BECK, A.H.W., 'Space Charge Waves', Pergamon Press, (1958).

BERNSTEIN, I.B., GREENE, J.M. and KRUSKAL, M.D., Phys. Review, 108, 546 (1957).

BISKAMP, D. and CHODURA, R., Phys. Rev. Letts., 27, 1553 (1971).

BLEANEY, B.I. and BLEANEY, B., 'Electricity and Magnetism', Clarendon Press, Oxford University, (1965).

BORIS, J.P., DAWSON, J.M., ORENS, J.H. and ROBERTS, K.V., Phys. Rev. Letts. 25, 706 (1970).

BUNEMAN, O., Phys. Rev. Letts., 1, 8 (1958).

BUNEMAN, O., Phys. Review, 115, 503 (1959).

CLARK, W.H.M., M.Sc. Dissertation, Oxford University, (1972).

CLEMMOW, P.C. and DOUGHERTY, J.P., 'Electrodynamics of Particles and Plasmas', Addison-Wesley, (1969).

DREICER, H., Phys. Rev., 115, 238 (1956).

DRUMMOND, W.E., MALMBERG, J.H., O'NEIL, T.M. and THOMPSON, J.R., Phys. of Fluids, 13, 2422 (1970).

DRUMMOND, W.E., THOMPSON, J.R., SLOAN, M.L., and WONG, H.V., Plasma Physics and Controlled Nuclear Fusion Research, Procs., vol.2, p.167, 1971, IAEA Vienna.

DRUMMOND, W.E. and ROSS, D.W., Proc. of Culham-SRC Symposium on Turbulence and Nonlinear Effects in Plasmas, p.1, (1973), HMSO.

Von ENGEL, A.H., 'Ionized Gases', Clarendon Press, Oxford University, (1955).

FRANKLIN, R.N., HAMBERGER, S.M., LAMPIS, G. and SMITH, G.J., UKAEA Culham Laboratory Report, CLM-R131, HMSO, (1974).

FRANKLIN, R.N., HAMBERGER, S.M., LAMPIS, G. and SMITH, G.J., Proc. Roy. Soc., A 347, 25 (1975).

FRIED, B.D. and CONTE, S.D., 'The Plasma Dispersion Function', Academic Press, (1961).

GENTLE, K.W. and LOHR, J., Phys. Rev. Letts., 30, 75 (1973).

GRADSHTEYN, I.S. and RYZHIK, I.M., 'Tables of Integrals, Series and Products', Academic Press, (1965).

HAMASAKI, S., DAVIDSON, R.C. and KRALL, N.A., Phys. Rev. Letts., 14, 2385 (1971).

HAMBERGER, S.M. and FRIEDMAN, M., Phys. Rev. Letts., 21, 674 (1968).

HAMBERGER, S.M. and JANCARIK, J., Phys. Fluids, 15, 825 (1972).

HAMBERGER, S.M. and SHARP, L.E., Bull. Amer. Phys. Soc., 18, 1312 (1973).

HAMBERGER, S.M., SHARP, L.E., WOODWARD, M. and CLARK, W.H.M., Proc. of 7th European Conference on Controlled Fusion and Plasma Physics Research, vol.1, p.164, Lausanne, 1974.

HENDEL, H. and YAMADA, M., Phys. Rev. Letts., 33, 1076 (1974).

JACKSON, J.D., Plasma Physics (J. Nucl. Energy, Pt.C), 1, 171 (1960).

De KLUIVER, H., PIEKAAR, H.W., RUTGERS, W.R., SCHRIJVER, H. and De GROOT, B., Plasma Physics and Controlled Nuclear Fusion Research, Procs., vol.2, p.67, 1971, IAEA Vienna.

KRALL, N.A. and TRIVELPIECE, A.W., 'Principles of Plasma Physics', McGraw-Hill, (1973).

MIKHAILOVSKII, A.B., 'Theory of Plasma Instabilities', vol.1, Consultants Bureau (Plenum), (1974).

MORSE, R.L. and NIELSON, C.W., Phys. Rev. Letts., 26, 3 (1971).

MOTLEY, R.W., 'Q-Machines', Academic Press, (1975).

O'NEIL, T.M., WINFREY, J.H. and MALMBERG, J.H., Phys. Fluids, 14, 1204 (1971).

NISHIHARA, K. and HASEGAWA, A., Phys. Rev. Letts., 28, 424 (1972).

ROBERTSON, S., KORN, P. and WHARTON, C.B., IEEE Trans. on Plasma Science, 2, 17 (1973).

SCHRIJVER, H., RUTGERS, W.R., van ELST, J.A., POST, H.A., KALFSBEEK, H.W., PIEKAAR, H.W. and De KLUIVER, H., Plasma Physics and Controlled Nuclear Fusion Research, Procs. vol.3, 271, 1974, IAEA Vienna.

SISONENKO, V.L. and STEPANOV, K.N., Plasma Physics, 13, 1033 (1971).

SMITH, G.J., D.Phil. Thesis, Oxford University, (1971).

STIX, T.H., 'The Theory of Plasma Waves', McGraw-Hill, (1962).

STRINGER, T.E., Plasma Physics (J. Nucl. Energy Pt.C), 6, 267 (1964).

TSYTOVICH, V.N., 'An Introduction to the Theory of Plasma Turbulence' Pergamon Press, (1972).

WESSON, J.A., SYKES, A. and LEWIS, H.R., Plasma Physics, 15, 49 (1973).